UNIVERSIDAD NACIONAL AUTÓNOMA DE MÉXICO
PROGRAMA DE POSGRADO EN ASTROFÍSICA

INSTITUTO DE RADIOASTRONOMÍA Y ASTROFÍSICA
(IRYA)

PRUEBAS Y CARACTERIZACIÓN DEL COLAPSO GRAVITACIONAL JERÁRQUICO EN NUBES MOLECULARES.

TESIS
QUE PARA OPTAR POR EL GRADO DE
DOCTOR EN CIENCIAS
(ASTROFÍSICA)

PRESENTA
RAÚL NARANJO ROMERO

TUTOR
DR. ENRIQUE VÁZQUEZ SEMADENI, IRYA

MIEMBROS DEL COMITE TUTOR
DR. JAVIER BALLESTEROS PAREDES, IRYA
DR. LUIS ALBERTO ZAPATA GONZÁLEZ, IRYA
DR. LAURENT RAYMOND LOINARD, IRYA

MORELIA, MICHOACÁN, ENERO 2018

Contents

List of Figures

List of Tables

To my beloved sons,

Antar Nahim and Rhaúl Abrahim.

Acknowledgements

I want to thank my supervisor, Prof. Enrique Vázquez, who helped me to develop this research project. It has been an honor for me to had the opportunity to work with you. I am profoundly grateful with you for the constant encouragement and inspiration.

I also like to express my gratitude to my co-supervisors Prof. Javier Ballesteros, Prof. Luis Zapata and Prof. Laurent Loinard whose thoughtful advise often used to help me on the good direction during my PhD.

To my dear friends Manuel Zamora, Jorge Tarango, Gisela Ortíz, Victor Ramírez, Robert Loughnane for your patience, motivation, enthusiasm, and for the sleepless nights we were working together for the last years.

Thanks to Prof. Gilberto Gómez, Prof. Aina Palau, Prof. Adriana Gazol, Prof. Bernardo Cervantes, Prof. Jacopo Fritz and many other great astronomers and human beings at the Instituto de Radiastronomía y Astrofísica, for promoting science and helping me to reach this life goal with your knowledge and kind support.

I would like to show a sincere gratitude to Karin Hollemberg. You have been a wonderful person and I am thankful for all your support with the academic issues.

I am also deeply grateful with my parents María Eugenia and Raúl, for your patience, understanding, trust and for always been there for me in one or other way.

Finally, thanks to the Consejo Nacional de Ciencia y Tecnología (CONACYT, doctoral fellowship CVU 318178), for the financial support on my PhD. To PAPIIT project IA103517 from DGAPA-UNAM, for the financial support.

Chapter 1

Introduction.

Molecular clouds (MC) have been considered generally to be dense virialized structures in the interstellar medium (ISM), supported by magnetic fields or turbulence, with relatively long free-fall times and collapsing only locally at the scale of the dense cores within them. Moreover, in recent years, several observational (*e.g.*, Peretto et al., 2013; Polychroni et al., 2013) and numerical works (*e.g.*, Vázquez-Semadeni et al., 2007; Heitsch and Hartmann, 2008; Heitsch et al., 2008; Vázquez-Semadeni et al., 2009, 2010, 2011; Ibáñez-Mejía et al., 2016) have suggested that instead MCs may be in a state of global hierarchical gravitational collapse (GHC), characterized by small structures collapsing on timescales shorter than those of the larger-scale collapsing structures in which they are hierarchically immersed.

Star formation occurs in the densest parts of MCs (the "dense cores"). The standard view of MC cores is that they start their lives as low-mass hydrostatic structures (supported either by thermal pressure, turbulent pressure or magnetic fields) which eventually become gravitationally unstable, either by mass accretion onto the hydrostatic cores (see *e.g.*, the review of André et al., 2014) or by dissipation of the internal supporting turbulence (*e.g.*, Bergin and Tafalla, 2007)[1]. The notion of hydrostatic cores within turbulent clouds, however, has been criticized by a number of authors (*e.g.*, Whitworth et al., 1996; Vázquez-Semadeni et al., 2005).

Moreover, recent observations have shown the ubiquity of filaments in MCs (see André et al., 2014, and references there in), which in addition appear to be funneling gas to dense cores (hubs) located at sites where various filaments converge (*e.g.*, Galván-Madrid et al., 2010; Schneider et al., 2010; Kirk et al., 2013; Peretto et al., 2013). Recent numerical simulations of cloud formation by colliding flows naturally reproduce this behavior (*e.g.*, Gómez and Vázquez-Semadeni, 2014) and suggest that the filaments constitute part of the collapse process. Nevertheless, existing models of filamentary structures[2] assume either radially hydrostatic structure (*e.g.*, Ostriker, 1964; Fischera and Martin, 2012) or radial accretion (*e.g.*, Heitsch, 2013a,b; Hennebelle and André,

[1] See also Sec. 4.2.1 for the case of magnetic support.

[2] In general, filaments' radial density (or column density) profile allows to determine their mass per unit length, which in turn is used as a gravitational instability criterion to study the observed evolutionary stage of the filaments.

2013), but have not considered the longitudinal flow along the filament so far.

In this work we present idealized numerical simulations of gravitationally collapsing cores and filaments embedded in globally unstable backgrounds, fully forgoing any assumption of a hydrostatic state, with the aim of extracting the essential flow features that develop in this scenario of global, hierarchical collapse.

In Chap. 2, we describe the theoretical foundations required for the numerical and theoretical study of these collapsing structures, followed by a description of the observational perspectives of star formation in molecular clouds, filaments and dense cores, in Chap. 3. In Chap. 4, we describe the current state of several star formation scenarios, including the main support mechanisms against gravitational collapse. We next present the numerical work of the early stages in the evolution of prestellar cores in Chap 5, and of filaments in Chap 6. Finally, some conclusions on the implications of the GHC scenario are presented in Chap. 7.

Chapter 2

Physical foundations

In this chapter we describe the theoretical frame necessary to describe the work in the present thesis. In particular, the numerical simulations presented here represent the gravitational collapse of a gas structure, which is described by means of the equations of gas dynamics in the presence of gravity. We elaborate these equations in this chapter together with other important equations such as the virial theorem and the Lane-Emden equation. We later elaborate some of the basic configurations of spherical density structures commonly used to describe the process of the collapse of molecular clouds, and hence the origins of protostars in those clouds. Finally, a general review is given on the classical theory of cloud collapse.

2.1 Fluid dynamics

2.1.1 The hydrodynamic approximation of fluids

We can study the ISM, treating it as a continuous medium using the fluid dynamics approximation, by considering a volume element in the fluid with typical length-scale, timescale and velocity much smaller than their macroscopic values[1], on which the fluid properties vary. This region must satisfy the following criteria: *i*) its size is much smaller than a length scale for the change of any physically relevant quantity q,

$$l_{\rm region} \ll \mathcal{L} \sim q/ \mid \boldsymbol{\nabla} q \mid, \tag{2.1}$$

where the scale length is the scale over which q varies by an order of unity; *ii*) It is large enough to contain a sufficiently large number of particles to avoid fluctuations due to their finite number (namely the discreteness noise),

$$n l^3_{\rm region} \gg 1, \tag{2.2}$$

[1]Where the fluid characteristic length-scale $\mathcal{L}$, and timescale $\mathcal{T}$, are related by a characteristic velocity $\mathcal{U} \sim \mathcal{L}/\mathcal{T}$.

where n is the number density per unit volume. These conditions apply for any system described as a fluid. Moreover, for a *collisional* fluid[1], *iii*) the fluid element is large enough that the constituent particles have a mean free path, λ_{mfp}, that satisfies:

$$l_{region} \gg \lambda_{\text{mfp}}. \tag{2.3}$$

Note that if the particles in the fluid interact with each other (which does not necessarily imply that they collide physically) and the aforementioned conditions are satisfied, then it is possible to define a volume element (or fluid parcel) ΔV in space that contains a sufficiently large number of particles so that local spatial and velocity averages can be computed. Therefore, the fluid (or bulk) velocity and the mass density of a given volume element can be defined as:

$$\boldsymbol{u} \equiv \lim_{\Delta V \longrightarrow 0} \frac{1}{N\Delta V} \sum_{i=1}^{N} \boldsymbol{v}_i \equiv \langle \boldsymbol{v} \rangle_{\Delta V},$$

$$\rho \equiv \lim_{\Delta V \longrightarrow 0} \frac{1}{\Delta V} \sum_{i=1}^{N} m_i,$$

where N is the number of particles within the volume element, and $\boldsymbol{v_i}$ and m_i are the i-th particle total velocity and mass.

This makes possible to define the mean kinetic energy (internal energy) within the volume of the fluid element. For instance, for a fluid with a single type of particles, the resulting kinetic energy distribution equals the velocity distribution in the fluid. This internal energy therefore determines the fluid temperature.

2.1.2 Description of fluid flows

There are two approaches to formulating the equations that describe the fluids:

In the *Eulerian* description of a fluid, given a small volume at a fixed spatial position, the fluid flows through the volume with physical variables specified as functions of time and the (fixed) position of the volume, *e.g.*, $q = q(\mathbf{r}, t)$. The change of any measurable quantity q as a function of time is the time derivative, $\partial q/\partial t$, evaluated at the fixed position.

In the *Lagrangian* description, one chooses a particular fluid element (labeled $\mathbf{a}$) and examines the change in any quantity (*e.g.*, $q(\mathbf{a}, t)$) within the flow as time goes on. Thus, the reference system is *comoving* with the fluid. Therefore, the Lagrangian time derivative, Dq/Dt[2], has a term due to the rate of change at a fixed location (*i.e.*, the Eulerian time derivative), and an additional term due to the fact that the fluid element has moved to a new location (with a velocity $\mathbf{u}$) where the variable has a different value.

$$\frac{Dq}{Dt} = \frac{\partial q}{\partial t} + \mathbf{u} \cdot \boldsymbol{\nabla} q, \tag{2.4}$$

where the last term is called the *convective derivative*.

[1] That in which the characteristic timescale is much longer than the frequency of the collisions in the fluid.

[2] The notation D/Dt is referred to as the "total" time derivative.

2.1.3 The formulation of the fluid equations

As mentioned before, we can consider the ISM as a magnetized, compressible fluid[1] , subject to a gravitational field. Thus, its behavior is governed by the hydrodynamic equations. These equations are based on Newtonian dynamics, and express the conservations of mass, momentum and energy, and are also known as the Euler equations when viscous effects are neglected. In addition, it is necessary to consider the magnetic flux conservation equation. We thus have:

$$\frac{\partial \rho}{\partial t} + \boldsymbol{u} \cdot \boldsymbol{\nabla} \rho = -\rho \boldsymbol{\nabla} \cdot \boldsymbol{u}, \textit{ mass conservation or continuity equation} \tag{2.5}$$

$$\frac{\partial \boldsymbol{u}}{\partial t} + \boldsymbol{u} \cdot \boldsymbol{\nabla} \boldsymbol{u} = -\frac{\boldsymbol{\nabla} P}{\rho} - \boldsymbol{\nabla} \Phi + \frac{1}{4\pi\rho} (\boldsymbol{\nabla} \times \boldsymbol{B}) \times \boldsymbol{B}, \textit{ momentum conservation} \tag{2.6}$$

$$\frac{\partial e}{\partial t} + \boldsymbol{u} \cdot \boldsymbol{\nabla} e = -(\gamma - 1) e \boldsymbol{\nabla} \cdot \boldsymbol{u} + \Gamma - n\Lambda, \textit{ internal energy conservation} \tag{2.7}$$

$$\frac{\partial \boldsymbol{B}}{\partial t} = \boldsymbol{\nabla} \times (\boldsymbol{u} \times \boldsymbol{B}), \textit{ magnetic flux conservation}, \tag{2.8}$$

where $\boldsymbol{u}$ is the gas velocity, ρ is the mass density, e is the internal energy per unit mass, $\boldsymbol{B}$ is the magnetic field[2] and P is the thermal pressure, which we assume is given by the ideal equation of state:

$$P = n k_B T, \tag{2.9}$$

where k_B is the Boltzmann constant, $n = \rho/(\mu m_H)$ is the number density of particles, μ is the mean weight per particle of gas, γ is the ratio between the specific heats at constant pressure and at constant volume for the fluid, m_H is the mass of the hydrogen atom, and Φ is the gravitational potential that satisfies *Poisson's equation*:

$$\nabla^2 \Phi = 4\pi G \rho. \tag{2.10}$$

The equation relating the internal energy and the temperature is:

$$e = C_V T \tag{2.11}$$

where C_V is the specific heat at constant volume. Finally, in eq. (2.7), Λ is the cooling function and Γ is the heating function. Both Γ and $n\Lambda$ have units of specific power (energy per unit time per unit mass).

Note that in these equations we are ignoring the efects of viscosity, electric resistivity, thermal conductivity and relativistic movements. Additionally we assume that the fluid is newtonian (*i.e.*, is isotropic and that any deformation is proportional to the velocity gradient), having zero net charge and the electric fields at macroscopic scale dissipate in times shorter than the systems characteristic timescale.

[1] For which a relative volume change is expected as a response to a pressure change, $\beta = -(1/V)(\partial V/\partial p)$, where β is the compressibility of the fluid. For instance, for an isothermal compressible flow, $\beta = 1/p = 1/\rho c_s^2$.

[2] Which must satisfy $\boldsymbol{\nabla} \cdot \boldsymbol{B} = 0$ in order to avoid magnetic monopoles.

Moreover, these equations can also be derived from a microscopic approach, treating the fluid as a ensemble of particles that interact via collisions (*i.e.*, that can be described by a distribution function in the phase space), by calculating the zeroth, first and second moment equations of the Boltzmann equation. For a collisional fluid, these equations are called the Navier-Stokes equations, while for a collisionless fluid these are called the Jeans equations. If the viscosity and conductivity of the fluid are ignored, the Navier-Stokes equations reduce to the Euler equations.

The left-hand sides (LHS) of the first three equations represent the *total* rate of change of the respective gas property of a fluid element, due to both changes at its current position and change due to the motion of the fluid element with velocity $\boldsymbol{u}$ to a new position (the second term is usually denoted as *advective* term). The right-hand sides (RHS) of the equations represent *source* and *sink* terms, and are responsible for changes in the gas properties. Specifically:

- In the mass conservation equation, the source term is due to a converging velocity field at the position of the fluid element, resulting in a density increase (or *vice versa*).
- In the momentum conservation equation, the fluid tends to move in the direction toward low pressure regions and toward regions where the gravitational potential is more negative. In this equation, the last term is the Lorentz force exerted by the magnetic field.
- In the energy conservation equation, the first term in the RHS is the adiabatic work PdV acting over the fluid parcel, for which $e = \frac{1}{\gamma-1}\frac{P}{\rho}$, and the sum of the second and third terms is the *net cooling* that results from cooling and heating processes.

2.2 Thermodynamics

The various components of the ISM are at very different ranges of temperature and density, although roughly at the same pressure[1], except at bubbles and molecular clouds (Myers, 1978). Thus, it is important to study those components from a thermodynamics point of view. For this reason we now will focus on the energy equation (2.7).

2.2.1 Heating and cooling

The heating and cooling functions (Γ and Λ, respectively) entering eq. (2.7) represent a variety of processes that act at the atomic and molecular level (Wolfire et al., 1995; Koyama and Inutsuka, 2002; Glover and Clark, 2014; Klessen and Glover, 2016). The

[1] With a variation of 5 orders of magnitude in temperature, and 3 orders of magnitude in density (Ferrière, 2001; Klessen and Glover, 2016), while one order of magnitude in pressure (*e.g.*, Audit and Hennebelle, 2005).

net rate of change of the gas temperature strongly depends on its temperature, density and metallicity. The *net cooling* of the gas is defined as:

$$\mathscr{L} \equiv n\Lambda - \Gamma \tag{2.12}$$

The molecules that make up the molecular component of the ISM are formed through very complex sequence of chemical reactions. Since Hydrogen is abundant in the universe, H_2 is the most abundant molecule and is thought to be formed by recombination on the surface of grains of interstellar dust (Hollenbach and Salpeter, 1971). The next molecule in abundance is CO, identified in an ultraviolet stellar spectrum (Smith and Stecher, 1971). Despite being formed continuously, the unique regions where these molecules can avoid dissociation by radiation are the interiors of dense clouds and the deeper interiors of diffuse clouds. The observed temperatures of these regions are explained as the result of the thermal balance between the heating by cosmic rays (and at the edges of the clouds, collisions with photoelectrons from dust grains and with radioactively excited) and cooling by molecular emission lines (mainly of CO) whose rate increases rapidly with the temperature (de Jong et al., 1980; Goldsmith, 1987; Hollenbach and Tielens, 1999). Collisions with dust grains also enter the thermal balance depending on the dust temperature with respect to that of the gas (Burke and Hollenbach, 1983). For instance, Koyama and Inutsuka (2002) have computed the analytical fitting of the heating and cooling functions for the atomic and molecular gas, including collisions with dust grains. More recently, Glover and Clark (2012) have identified three main regimes with different heating and cooling dominant processes in molecular clouds (see their Fig. 8): i) at low densities ($n < 1000\,\mathrm{cm}^{-3}$), C^+ is the dominant coolant, while the main heating process is photoelectric emission from dust. ii) for densities in the range $1000\,\mathrm{cm}^{-3} \leqslant n \leqslant 10^5\,\mathrm{cm}^{-3}$, C^+ quickly gives way to CO as the dominant coolant, reflecting the fact that the gas becomes CO dominated around $n = 1000\,\mathrm{cm}^{-3}$, while photoelectric heating quickly becomes irrelevant as dissipation in shocks becomes the main source of heat. iii) At $n > 10^5\,\mathrm{cm}^{-3}$, dust takes over from CO as the most important coolant, and PdV heating becomes almost as important as shock heating.

2.2.2 Cooling time

Since MCs emit radiation and thus cool, it is useful to calculate the cooling time. This time essentially depends on the internal energy of the gas, e, and the rate at which the gas emits energy due to its net cooling. Thus, we can define the cooling time as:

$$\tau_{\mathrm{cool}} \approx \frac{e}{|n\Lambda - \Gamma|}. \tag{2.13}$$

Frequently, if the gas is optically thin, the heating and cooling functions have characteristic times much shorter than the dynamic crossing time of the fluid. In this case, the heating and cooling functions balance mutually ($n\Lambda = \Gamma$), thus giving a relation between the density and the temperature. This relation allows us to eliminate the temperature dependence from the equation of state, resulting in a *barotropic* relation where pressure depends only on density. Because the temperature regime of the MCs

is approximately isothermal, in the rest of this work we will refer to the special case of an isothermal gas in which $P = c_s^2 \rho$, where $c_s = \sqrt{k_B T/\mu m_H}$ is the sound speed.

2.3 The virial theorem

The scalar virial theorem (VT) is obtained from the dot product of the momentum equation (2.6) with the position vector $\mathbf{x}$, and integrating of the product over some volume V (see Vazquez-Semadeni, 1997). Traditionally, the volume V is taken in a Lagrangian frame of reference. The VT states that:

$$\frac{1}{2}\frac{d^2 I}{dt^2} = 2K + \left(2U - \oint_S P\mathbf{x}\cdot d\mathbf{S}\right) + \left(\mathfrak{M} + \oint_S \mathbf{x}\cdot\mathbf{T}\cdot d\mathbf{s}\right) + W, \tag{2.14}$$

where, d/dt is the total or Lagrangian derivative operator (see eq. [2.4]), I is the moment of inertia, S is the surface enclosing the volume. W, K, U, and $\mathfrak{M}$ are respectively the gravitational, kinetic, internal, and magnetic energies contained within the volume. $\mathbf{T}$ is the Maxwell's magnetic stress tensor $\mathbf{T} \equiv T_{ij} \equiv B_i B_j/4\pi - |\mathbf{B}|^2\delta_{ij}/8\pi$, such that the Lorentz force term satisfies $(\boldsymbol{\nabla}\times\mathbf{B})\times\mathbf{B}/4\pi = \boldsymbol{\nabla}\cdot\mathbf{T}_{ij}$.

In particular, the virial equilibrium condition, $d^2I/dt^2 = 0$, establishes a balance among all the energies in a system.

2.4 Stability analyses of density configurations

2.4.1 Pressure confinement

Let us consider a fluid with $\mathbf{u} = \mathbf{B} = 0$, neglecting self-gravity, and considering the virial equilibrium condition. The VT reduces to $2U = \oint_S P\mathbf{x}\cdot d\mathbf{S}$. Therefore, there is a balance between the internal and external pressures in the fluid's surface. Thus, the fluid is considered as pressure confined.

2.4.2 Hydrostatic equilibrium

One of the most basic equilibrium configurations for a fluid is *hydrostatic equilibrium*. In particular, if $\mathbf{u} = \mathbf{B} = 0$ everywhere, and $\partial/\partial t = 0$, the continuity equation is trivially satisfied. The momentum equation, in which the only non-zero terms are now gravity and pressure, which themselves must be mutually balanced, becomes

$$\frac{1}{\rho}\boldsymbol{\nabla}P = \mathbf{g} = -\boldsymbol{\nabla}\Phi. \tag{2.15}$$

Note that similarly, from the VT, considering the virial equilibrium condition, one can obtain $W = -2U$. In addition, for barotropic cases where $P = P(\rho)$, we can use Poisson's equation to solve for the density distribution corresponding to hydrostatic equilibrium, and therefore provide solutions for the pressure and gravitational potential everywhere, fully describing the fluid.

2.4.3 Pressureless collapse

The simplest case of gravitational collapse is that of a spherical cloud in which the internal pressure is negligible, and thus the gas will move towards the center of the cloud in a regime near to free-fall (see Lin et al., 1965). Let us assume a cloud of with initial radius r_0. The equation of motion of a shell of material is:

$$\frac{d^2r}{dt^2} = -G\frac{M(r)}{r^2}, \tag{2.16}$$

where the RHS is the local gravitational acceleration of the shell, and $M(r)$ is the mass interior to a radius r. By integrating this equation over time, we obtain the infall velocity of the shell after been contracted to a radius r[1]:

$$\frac{dr}{dt} = -\left[2GM(r)\left(\frac{1}{r} - \frac{1}{r_0}\right)\right]^{1/2}. \tag{2.17}$$

Note that since we are interested only in the surface that encloses $M(r)$, we have assumed that the mass interior to r remains constant during the collapse. Integrating this equation, we get an expression for the position of the shell as a function of time:

$$r(M,t) = r_0(M)\ cos^2\theta, \tag{2.18}$$

where

$$\theta + \frac{1}{2}\ sin2\theta = \left(\frac{8\pi}{3}G\rho_0\right)^{1/2} t, \tag{2.19}$$

and ρ_0 is the mean density of the sphere of radius r_0. From here, the *free-fall time* can be considered as the total time from the beginning of the contraction and until the formation of the singularity (*i.e.*, where the radius srinks to zero), and thus:

$$t_{ff} = \left(\frac{3\pi}{32G\rho_0}\right)^{1/2}. \tag{2.20}$$

It is noteworthy that the free-fall time is independent of the initial cloud radius. Therefore, if the initial sphere have uniform density, every shell of the cloud will span the same collapsing time and the density will increase at the same rate everywhere. This behavior is known as the *homologous collapse*. On the contrary, if the cloud were centrally condensed at the beginning, then the free-fall time of the material close to the center will be shorter than the free-fall time for the material at larger radii. Thus, the central density will increase at a rate faster than for other cloud regions. In this case, the collapse is referred as an *inside-out collapse*. We will discuss it later in Chaps. 5 & 6.

[1] See *e.g.*, Ostlie and Carroll (2006) for the details on the development.

2.4.4 The Jeans gravitational instability

Now, let us consider a fluid at rest, with uniform density and pressure, filling all space. By considering a perturbation of the fluid variables

$$\rho = \rho_0 + \rho', \tag{2.21}$$
$$P = P_0 + P', \tag{2.22}$$
$$\Phi = \Phi_0 + \Phi', \tag{2.23}$$
$$\boldsymbol{u} = \boldsymbol{u'}, \tag{2.24}$$

in the equations of mass and momentum conservation (2.5, 2.6) and Poisson's equation (2.10), under the equilibrium condition $u_0 = 0$, we obtain the set of equations:

$$\frac{\partial \rho'}{\partial t} + \rho_0 \boldsymbol{\nabla} \cdot \mathbf{u} = 0 \tag{2.25}$$
$$\frac{\partial \mathbf{u}}{\partial t} = -\frac{1}{\rho_0} \nabla P' - \nabla \Phi' \tag{2.26}$$
$$\nabla^2 \Phi' = 4\pi G \rho'. \tag{2.27}$$

If the perturbations are adiabatic, the density and pressure perturbations are related by:

$$P' = c_\mathrm{s}^2 \rho'. \tag{2.28}$$

We now expand all fluid variables as a superposition of traveling waves, so that all quantities have the form $\exp(-i\mathbf{k} \cdot \mathbf{r} + i\omega t)$, where $\mathbf{k}$ is the wave vector, $\mathbf{r}$ is the position vector, ω is the frequency, and t is the time. Therefore, using the expression for the perturbed pressure, P', in the set of equations, we obtain:

$$i\omega \mathbf{u} = -i\mathbf{k} c_\mathrm{s}^2 \frac{\rho'}{\rho_0} - i\mathbf{k}\Phi' \tag{2.29}$$
$$i\omega \frac{\rho'}{\rho_0} + i\mathbf{k} \cdot \mathbf{u} = 0 \tag{2.30}$$
$$-k^2 \Phi' = 4\pi G \rho', \tag{2.31}$$

where $k \equiv |\mathbf{k}|$ is the wave number. Combining these equations, we obtain the dispersion relation:

$$\omega^2 = k^2 c_\mathrm{s}^2 - 4\pi G \rho_0. \tag{2.32}$$

Note that in the absence of gravity (*i.e.*, $G = 0$) we recover acoustic waves propagating at the sound speed. Moreover, the presence of gravity modifies the waves by a frequency $\omega_G = (4\pi G \rho_0)^{1/2}$, with characteristic timescale $\tau_G = 2\pi/\omega_G = (\pi/G\rho_0)^{1/2}$. If the gravity term becomes large enough (which occurs at sufficiently large wavelengths), then $\omega^2 < 0$, and gravitational instability sets in (since at this point the fluctuations cease to be traveling waves, and instead, their amplitude begins to grow exponentially

in time). The critical wavelength at which this occurs is set by the condition $\omega^2 = 0$. Thus remembering that the wave length, $\lambda = 2\pi/k$, we obtain the *Jeans length* as:

$$\lambda_{\rm J} = \sqrt{\frac{\pi c_{\rm s}^2}{G\rho_0}}. \tag{2.33}$$

We can also define the critical *Jeans mass* as the mass contained in a sphere of radius equal to $\lambda_{\rm J}/2$:

$$M_{\rm J} = \frac{4}{3}\pi\rho_0 \left(\frac{\lambda_{\rm J}}{2}\right)^3 \tag{2.34}$$

Now let us consider a fluid element of size $\sim \lambda$. Gravity acts on it, trying to make it collapse on a timescale τ_G. Meanwhile, the pressure gradient provides support against gravity, but adjacent fluid elements are also in communication with each other through pressure. Since this communication occurs at the sound speed, (*i.e.*, at a timescale $\tau_{\rm s} = \lambda/c_{\rm s} = \tau_G$[1] when $\lambda = \lambda_{\rm J}$), for fluid elements larger than the Jeans length (or equivalently for fluid elements of mass larger than the Jeans mass), it cannot occur quickly enough to prevent a gravitational collapse.

2.4.4.1 The Jeans swindle

It is noteworthy that, in the previous treatment, the initial unperturbed state is inconsistent. That is, given that the density is uniform and that it is filling all space, it cannot satisfy the unperturbed Poisson's equation together with the condition $\nabla\Phi = 0$. This inconsistency is known as the "Jeans-swindle". The solution of this conundrum requires the consideration that the background is not static, but rather expanding or contracting, as was done by Einstein in the formulation of the General Theory of Relativity.

2.4.5 Hoyle fragmentation

If we now consider an isothermal cloud in gravitational collapse, its density will increase while the cloud is contracting and therefore the Jeans mass (eq. [2.34]) will be reduced, producing unstable sub-volumes that will condense and collapse on their own. This so-called *Hoyle fragmentation* (Hoyle, 1953) can continue until the gas opacity is so high that radiation cannot escape from inside. Therefore, changing the effective equation of state of the gas, and consequently stopping subsequent contraction and fragmentation. The gravitational energy loss rate in the cloud is given by:

$$\dot{E}_{\rm grav} \sim \frac{\left(GM^2/R\right)}{\tau_{\rm cool}}, \tag{2.35}$$

[1] This can be easily understood if we think about $\tau_{\rm s}$ as the sound crossing time, and τ_G as the free-fall time.

and considering that during collapse, the energy release process has an efficiency η, we can express the radiated luminosity as:

$$L_{\rm rad} = (4\pi R^2)(\eta \sigma_{\rm B} T^4), \tag{2.36}$$

where $\sigma_{\rm B}$ is the Stefan-Boltzmann constant. If the cloud is optically thick, the emitted energy is absorbed somewhere in the cloud and then re-emitted in other regions. In this case, the fragment will radiate as a black body ($\eta = 1$, $L = L_{\rm rad}$):

$$L = 4\pi \sigma_{\rm B} R^2 T^4. \tag{2.37}$$

Then, by equating (2.35) and (2.37) we obtain a lower limit for the fragment mass as:

$$M_{\rm frag} \geq \pi^2 \left(\frac{32}{9}\right)^{1/4} \left(\frac{k}{\mu}\right)^{9/4} \frac{T^{1/4}}{G^{3/2}\sigma_{\rm B}^{1/2}} \simeq 0.01\ T_1^{1/4}\ {\rm M}_\odot, \tag{2.38}$$

where $T_1 = T/10{\rm K}$. This over-simplified fragmentation process of course does not include influences by rotation, turbulence and magnetic fields.

2.4.6 Magnetic field. Support and mass-to-flux relation

Now we will consider another support mechanism against the gravity of a parcel of gas, this time provided by the magnetic field, using a treatment based on the energy balance.

Let us consider a sphere with uniform magnetic field $\boldsymbol{B}$ inside and a vanishing field outside, and $\mathbf{u} = P = 0$. The magnetic energy stored within the volume V (*e.g.*, Shu, 1992), is:

$$\mathcal{M} = \frac{B^2}{8\pi} V = \frac{B^2 R^3}{6}, \tag{2.39}$$

and the magnetic flux passing on a cylindrical cross section of area A and radius R is:

$$\phi = BA = \pi B R^2. \tag{2.40}$$

In absence of any diffusion or dissipation processes, the magnetic flux is conserved (in agreement with the *flux freezing* condition, eq. [2.8]), and thus $\mathcal{M} = \phi^2/(6\pi R)$. The gravitational energy of the sphere is $W = -3GM^2/5R$. Therefore, the ratio of the gravitational to magnetic energy is:

$$\frac{|W|}{\mathcal{M}} = \frac{18\pi^2 G}{5} \left(\frac{M}{\phi}\right)^2, \tag{2.41}$$

where the term between the parenthesis is named the mass-to-flux ratio. The collapse condition $|W| > \mathcal{M}$, implies that:

$$\frac{M}{\phi} > \left(\frac{M}{\phi}\right)_{crit,sph} \equiv \sqrt{\frac{5}{18\pi^2 G}}, \tag{2.42}$$

where the numerical value depends on the geometry. Nakano and Nakamura (1978), made the calculation for a cylindrical geometry, obtaining:

$$\left(\frac{M}{\phi}\right)_{crit,cyl} \equiv \sqrt{\frac{1}{4\pi^2 G}}. \tag{2.43}$$

Thus, clouds can be classified as:

- $\frac{M}{\phi} < \left(\frac{M}{\phi}\right)_{crit}$ magnetically subcritical,
- $\frac{M}{\phi} > \left(\frac{M}{\phi}\right)_{crit}$ magnetically supercritical.

A magnetically subcritical cloud can be supported by the magnetic field against its own gravity, while a magnetically supercritical cloud cannot. It is noteworthy that the magnetic surface term (which can explicitly appear in a more detailed version of energy conservation equation, 2.7) includes the effects of both the external magnetic pressure and the magnetic tension along the magnetic field lines, and thus, is not exclusively confining. Moreover, if the magnetic field is uniform, the corresponding volume and surface contributions of the magnetic field in the VT cancel one each other, indicating balance between the internal and external stresses.

2.4.7 The Lane-Emden equation

Let us consider the density structure of a spherical cloud in hydrostatic equilibrium for which:

$$-\frac{1}{\rho}\boldsymbol{\nabla} P - \boldsymbol{\nabla}\Phi = 0. \tag{2.44}$$

This condition, together with the equation of state (eq. [2.9]), implies that $\ln\rho + \Phi/c_{\rm s}^2$ is a spatial constant. Thus, assuming spherical symmetry, we can write:

$$\rho\left(r\right) = \rho_c \exp\left(-\Phi/c_{\rm s}^2\right), \tag{2.45}$$

where ρ_c is the central density and $\Phi = 0$ at the cloud's center. Therefore, by considering spherical symmetry, Poisson's equation becomes:

$$\frac{1}{r^2}\frac{d}{dr}\left(r^2\frac{d\Phi}{dr}\right) = 4\pi G\rho_c\left(\frac{-\Phi}{c_{\rm s}^2}\right). \tag{2.46}$$

It is useful to write this equation in dimensionless form by defining $\Psi \equiv \Phi/c_{\rm s}^2$, and a non-dimensional length:

$$\xi \equiv \left(\frac{4\pi G\rho_c}{c_{\rm s}^2}\right)^{1/2} r. \tag{2.47}$$

Thus, eq. (2.46) becomes the *isothermal Lane-Emden equation*:

$$\frac{1}{\xi^2}\frac{d}{d\xi}\left(\xi^2\frac{d\Psi}{d\xi}\right) = \exp\left(-\Psi\right). \tag{2.48}$$

This particular form is a special case of the generic Lane-Emden equation that governs the structure of spherical *polytropes* (for which $P \propto \rho^{1+1/n}$) in the limit $n \to \infty$. Its first boundary condition is $\Psi(0) = 0$, while the second condition can be derived from the Poisson's equation by noting that the force produced by the gravitational potential of the mass interior to a radius r, is $-GM(r)/r^2$, and that close to the center this mass approaches to $(4\pi/3)\,\rho_c r^3$. It follows that the force, and consequently $d\Psi/d\xi$, must vanish as ξ goes to zero.

The Lane-Emden equation admits *regular* solutions (*i.e.*, with finite values of the variables at the origin) and *singular* solutions (for which some of the variables can have singularities at the origin). This equation is solved numerically starting from the center and integrating outwards.

2.4.8 The Singular Isothermal Sphere

Considering the ratio ρ/ρ_c which is given by $\exp(-\Psi)$ (see eq. [2.45]), we note that the density, and consequently the pressure, drop monotonically at every radius away from the center. This behavior is characteristic of all hydrostatic configurations, necessary to produce a pressure gradient capable of overcoming the inward pull of gravity. The singular solution of the Lane-Emden equation proposed by Shu (1977) is characterized by the fact that at large distances ($\xi \gg 1$), the ratio ρ/ρ_c asymptotically approaches to $2/\xi^2$, and thus the asymptotic solution is given by:

$$\rho(r) = \frac{c_s^2}{2\pi G r^2}, \tag{2.49}$$

$$\frac{d\Phi}{dr} = \frac{2c_s^2}{r}, \tag{2.50}$$

and is known as the *Singular Isothermal Sphere* (SIS).

Note that the SIS has no outer radius, *i.e.*, it occupies all space, and therefore its total mass is infinite as $M(r)$ grows linearly with r. Moreover, even though the corresponding potential, $\Phi = \ln(\xi^2/2)$, does not satisfy the boundary conditions at $\xi = 0$, the SIS is frequently used to estimate the cloud properties. Thus, its use has been criticized because of the improbability that this particular configuration is produced (*e.g.*, Whitworth and Summers, 1985).

Taking in account that clouds are not infinite, the pressure does not really fall to zero at their boundary, but to some value P_0 and a corresponding density ρ_0 at the "edge" r_0, and non-dimensional radius ξ_0. Thus the ratio ρ_c/ρ_0 indeed parametrizes models of isothermal spheres with mass:

$$M = 4\pi \int_0^{r_0} \rho r^2 dr \tag{2.51}$$

and a non-dimensional mass:

$$m = \left(4\pi \frac{\rho_c}{\rho_0}\right)^{-1/2} \left(\xi^2 \frac{d\Psi}{d\xi}\right)_{\xi_0}. \tag{2.52}$$

This function has an oscillatory behavior. We can know the value of ξ_0 for each ρ_c/ρ_0, and therefore the last factor of the RHS of eq. (2.52) can be determined from $\Psi(\xi)$. First, when $\rho_c/\rho_0 = 1$, $\xi_0 = 0$, and thus $m = 0$. Then, with increasing density contrast, m rises to a maximum value $m_1 = 1.18$ at $\rho_c/\rho_0 = 14.1$. The mass then drops to a minimum value of $m_2 = 0.695$, and so on, eventually approaching an oscillatory fashion in which the asymptotic limit, $m_\infty = (2/\pi)^{1/2} = 0.798$, corresponds to the non-dimensional mass of the singular isothermal sphere, (see Fig. 9.2 of Stahler and Palla, 2005).

2.4.9 Bonnor-Ebert spheres

The family of regular solutions of the Lane-Emden equation are known as the Bonnor-Ebert spheres (BE, Ebert, 1955; Bonnor, 1956)[1]. It is noteworthy than only a limited number of the models given by this equation and parametrized by the ratio ρ_c/ρ_0 are gravitationally stable.

For instance, let us consider a cloud of low density contrast $\rho_c/\rho_0 = \exp(-\Psi) \approx 1 - \xi_0^2/6$ [2]. Given the density distribution, the effective density, ρ_{eff}, can be approximated by P_0/c_s^2. Thus, considering that $M = 4\pi r^3 \rho_{eff}$, we obtain the cloud's radius:

$$r_0^3 \approx \frac{3Mc_s^2}{4\pi P_0}. \tag{2.53}$$

Therefore, any rise of the internal pressure will act to expand the configuration of the initial structure, thus providing stability to the cloud. For low density clouds, the fact that in this equation the gravitational constant does not appear is usually interpreted as the clouds being not self-gravitating, *i.e.*, they are confined by external pressure.

On the contrary, for self-gravitating configurations (*i.e.*, high density contrast clouds), it would be more difficult for the central regions to expand after an increase in the external pressure. In particular, gravitationally unstable configurations are characterized by ratios $\rho_c/\rho_0 > 14.1$ or equivalently $M > M_{BE}$, where the critical value, known as the *Bonnor-Ebert mass* is given by:

$$M_{BE} = \frac{m_1 c_s^4}{P_0^{1/2} G^{3/2}}. \tag{2.54}$$

It is noteworthy that in order to be truncated, BE-spheres need to be immersed in a warmer and rarefied medium, so that its weight over the sphere is negligible. Due to its higher temperature, however, can be at the same pressure than that on the surface of the sphere, and thus, be the pressure confining it. This particular configuration can be achieved for instance, through a transition from the cold to the warm phase of the ISM, at the sphere's boundary. Nevertheless, there is no observational evidence that the dense cores of MCs, which are the main candidates to be BE-spheres (*e.g.*, Lada et al., 2007), are surrounded by warm gas. See also Fig. 2.1 for various solutions of the Lane-Emden equation.

[1] See Sipilä et al. (2015) for the non-magnetic case and Nejad-Asghar (2016) for the magnetic case of non-isothermal BEs.

[2] For which a Taylor series expansion of $\Psi(\xi) = \xi^2/6 + \mathcal{O}(\xi^4)$ has been considered.

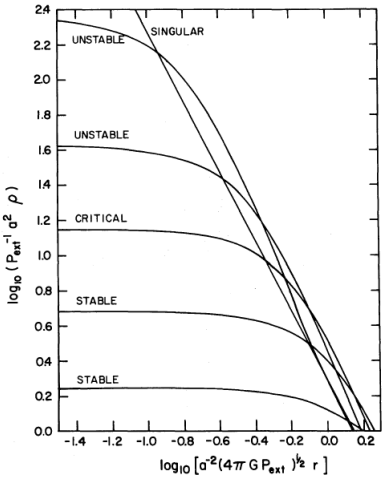

Figure 2.1 Solutions of the Lane-Emden equation, showing two stable, two unstable and the marginally stable ("critical") configurations, together with the SIS. From Shu (1977).

Moreover, any increase of the external pressure on isothermal spheres would create internal oscillations around the equilibrium configuration. Let us consider a perturbation in such configurations, mathematically described by *e.g.*, $\rho(r,t) = \rho_{eq}(r) + \delta\rho(r)\exp(i\omega t)$. For any equilibrium cloud model characterized by the criterion $\omega^2 > 0$, the density and all other physical quantities undergo oscillations of fixed amplitude. On the contrary, for $\omega^2 < 0$ the perturbation can grow exponentially rendering it to be unstable. In the interstellar environment in which molecular clouds are embedded it is inevitable that a perturbation occurs. Thus, if the configuration is unstable, it will necessarily be pushed away from equilibrium by the environmental perturbations.

2.4.10 Rescaling and self-similarity of flows

We have seen that generally, astrophysical fluids can be described via the principles of conservation of mass, momentum, and energy in the presence of self-gravity in the form of equations with boundary conditions. These equations can be expressed in such a way that their LHS are formed by the total rate of change of some property q of the fluid element (due to both the change of this property at its actual position or due to the movement of the fluid element with a velocity u to a new position where it has a different value), and the RHS expresses the source terms causing these space-temporal changes (*i.e.*, as the rate of change of q). An interesting aspect of this formulation is that these rates of change correspond to different physical processes acting on the fluid, and the corresponding characteristic time given by the ratio of the physical property to its rate of change. Thus, in general, the behavior of the fluid will depend on the ratios of the characteristic times for different involved physical processes. Therefore, the different time ratios can be considered as dimensionless parameters that ultimately

determine the evolution of the fluid.

Another interesting aspect is that the fluid equations can be *rescalable*, in the sense that they can describe two flows of different physical scale but with the same dimensionless parameters. Thus, the flow's behavior must be identical, if all the system variables has been rescaled in an adequate way. Moreover, a flow could be similar to itself at a different time and space location. In this case, the fluid dynamics equations must have invariant solutions as long as we introduce some *similarity variables* that satisfy the invariance conditions, *i.e.*, nondimensional variables constructed as a combination of the original spatial and temporal variables together with any relevant physical parameters of the problem, that continue to satisfy the equations when written in terms of the new variables. It is noteworthy that in general the flow self-similarity is only asymptotically fulfilled when the initial and boundary conditions are compatible with it. Thus, the self-similarity would be only achieved far enough from the boundaries and far enough from initial conditions both in position and time.

2.4.10.1 Similarity analysis

Let us now consider the gravitational collapse of an arbitrarily extended spherical isothermal cloud following the treatment of Shu (1977). Considering the cloud as composed of spherical shells, from the mass and momentum conservation equations, we obtain:

$$\frac{\partial M}{\partial t} + u\frac{\partial M}{\partial r} = 0, \tag{2.55}$$

$$\frac{\partial u}{\partial t} + u\frac{\partial u}{\partial r} = -\frac{c_s^2}{\rho}\frac{\partial \rho}{\partial r} - \frac{GM}{r^2}, \tag{2.56}$$

where M is the mass inside a shell of radius r, for which:

$$\frac{\partial M}{\partial r} = 4\pi r^2 \rho, \tag{2.57}$$

from continuity equation.

As we can see in equations (2.55)-(2.56), the only relevant physical parameters of the problem are the sound-speed and the gravitational constant. Thus, we must use it to obtain the equations in dimensionless form. This can be done by writing all physical variables A (*i.e.*, ρ, M, and u) as the product of a dimensional unit A_0 that depends on time, and a dependent dimensionless similarity variable a that depends on position and time:

$$A(r,t) \equiv A_0(t)\ a(x(r,t)), \tag{2.58}$$

where the independent dimensionless similarity variable can be defined as:

$$x \equiv \frac{r}{c_s t}. \tag{2.59}$$

Note that with this assumption, the flow at a given time resembles its own configuration at a different time, but at a different position (*i.e.*, this describe the *self-similarity* of the possible solutions of the problem).

The units for A_0 can be set by considering the dimensional analysis of the physical variables involved. For instance, $[G] = L^3 M^{-1} T^{-2} = [\rho]^{-1}[t]^{-2}$, suggesting the choice of the dimensionless variables:

$$\rho(r,t) = \frac{\bar{\rho}(x)}{4\pi G t^2}, \tag{2.60}$$

$$M(r,t) = \frac{c_s^3 t}{G} m(x), \tag{2.61}$$

$$u(r,t) = c_s v(x), \tag{2.62}$$

where $\bar{\rho}$, m, and v are the dimensionless density, mass and velocity, respectively. Therefore, taking in account the chain rule for derivatives, both in position and time, in equations (2.55) and (2.57), we obtain:

$$\frac{dm}{dx} = x^2 \bar{\rho}, \tag{2.63}$$

$$m + (v - x)\frac{dm}{dx} = 0. \tag{2.64}$$

Combining these equations, we obtain:

$$m = x^2 \ \bar{\rho} \ (x - v). \tag{2.65}$$

Thus, by substitution in our initial mass and momentum conservation equations we get a nonlinear set of ordinary differential equations:

$$\left[(x-v)^2 - 1\right] \frac{dv}{dx} = \left[(x-v)\bar{\rho} - \frac{2}{x}\right](x - v), \tag{2.66}$$

$$\left[(x-v)^2 - 1\right] \frac{1}{\bar{\rho}} \frac{d\bar{\rho}}{dx} = \left[\bar{\rho} - \frac{2}{x}(x-v)\right](x - v). \tag{2.67}$$

This set of equations has two types of solutions: the first is a static unstable solution corresponding to the SIS:

$$v = 0, \quad \bar{\rho} = \frac{2}{x^2}, \quad m = 2x. \tag{2.68}$$

Historically, this has been considered as the "natural" initial condition for subsequent gravitational collapse (Shu, 1977). This choice, however, is unfortunate, since it ignores the fact that the ISM is turbulent. For example, clumps and dense cores could have their origin in density fluctuations dynamically formed due to the turbulence, and therefore such unstable configurations will not arise naturally. This point has been noted by Whitworth et al. (1996) and Vázquez-Semadeni et al. (2005), and more recently by us as part of this thesis (see Naranjo-Romero et al., 2015, included in Chapter 5).

The second type is a dynamic solution that must be obtained numerically, which has as an initial condition a hydrostatic sphere *similar* to the SIS, except that its mass is $m = (2+\epsilon)x$, *i.e.*, slightly larger than that for a SIS. From this solution, we can note several important points:

First, we can consider the SIS-like initial condition as the moment in which a protostar (*i.e.*, the singularity) is formed at $r = 0$ with mass $M = \int_{\mathrm{V}} \rho dV = 0$ due to that $dV \to 0$ even though $\rho \to \infty$.

The solutions for $x > 0$ correspond to times $t > 0$. At these times, the solutions have the asymptotic form:

$$v \to -\left(\frac{2m_0}{x}\right)^{1/2}, \quad \bar{\rho} \to \left(\frac{m_0}{2x^3}\right)^{1/2}, \quad m \to m_0 \tag{2.69}$$

in the limit $x \to 0$, where $m_0 = 0.975$[1] is the non-dimensional mass that has been accreted to the central object of mass:

$$M(0,t) = \frac{m_0 c_{\mathrm{s}}^3}{G} t, \tag{2.70}$$

with accretion rate:

$$\dot{M} = \frac{m_0 c_{\mathrm{s}}^3}{G} \tag{2.71}$$

Note that at $x = 1$, the velocity $v = 0$, and thus, the sound wave has reached a radius $r = x c_{\mathrm{s}} t$. Beyond this radius, the system has not "noted" that its internal parts are collapsing, because this requires the sound wave at speed c_{s}, to reach to those regions, and thus, they preserve their initial conditions. The accretion process is established through a *rarefaction wave* located at $x = 1$. The material inside this radius is falling toward the central object with infall velocity, $v_{inf} = (2GM/r)^{1/2}$, and the wave front, located at a physical radius $r = c_{\mathrm{s}} t$ (for $x = 1$), propagates outwards at the sound speed.

In the internal parts, $0 < x < 1$, the flow has density and velocity profiles different from those of the SIS, and in the most internal parts, *i.e.*, for $x \to 0$, it approaches the asymptotic solution given by:

$$\mid v \mid \propto r^{-1/2}, \quad \rho \propto r^{-3/2}. \tag{2.72}$$

In the intermediate points, the material is being accelerated from zero velocity at $x = 1$ to the free-fall velocity at $x \to 0$. The collapse mode described here is called *the inside-out* collapse, and is generally considered the standard mode of collapse of dense cores in the star formation process.

Note that it is also valid to suppose an initial condition that is not an SIS, but that has similar density structure to the SIS, with non-zero infall speed. For it, the asymptotic solution in the limit $x \to \infty$ has the form:

$$v \to -\frac{\mathcal{A} - 2}{x}, \tag{2.73}$$

$$\bar{\rho} \to \frac{\mathcal{A}}{x^2}, \tag{2.74}$$

$$m \to \mathcal{A} x, \tag{2.75}$$

[1] This value can be obtained by numerically integrating the set of eqs. (2.66-2.67)

where $\mathcal{A} > 2$ in order to get a speed different from zero. This solution has no critical points. Note that the value for the mass of the central object, m_0, is related to $\mathcal{A}$ due to the fact that the limit $x \to \infty$ could be considered as an initial condition because it corresponds to $t \to 0$, and thus, the expected accretion rate could be larger that that for the hydrostatic condition corresponding to $\mathcal{A} \to 2^+$.

2.4.11 Classical solutions of collapsing self-gravitating isothermal gas spheres

Even though there have been several classic seminal works on the collapse of self-gravitating isothermal gas spheres (*e.g.*, Penston, 1969; Larson, 1969; Hunter, 1977), a compehensive description was given by Whitworth and Summers (1985). These authors discovered that each of the discrete solutions previously found can be expressed as a bounded two-parameter continuum of solutions (namely, the cloud's initial central density, z_0 and the central point mass, w_0, originated by the collapse, see Fig. 2.2). They found that z_0 characterizes the asymptotic form of the solution at early times, reflecting how intrinsically unstable against contraction the cloud interior is from the outset, while w_0 characterizes the asymptotic form of the solution at very late times, reflecting the importance of the external pressure in driving the compression. They further argue that if the cloud interior is initially close to hydrostatic equilibrium, then sound waves will propagate inwards, both providing support against the collapse and for some regions the gas will flow outwards for a time. Thus, it is only the arrival of a compression wave driven into the cloud by external pressure which converts the cloud to overall contraction. On the other hand, if the cloud's interior is far from hydrostatic equilibrium, then it will immediately start an overall contraction, and a sound wave will propagate inwards, amplifying any initial contraction, leaving a uniform velocity field behind. This will eventually form a central point mass that will subsequently grow by accretion, and then a rarefaction wave will propagate outwards through the infalling gas, leaving a free-fall velocity field in the inner parts. Fig. 2.2, shows the plane (Z,W) splitted into discrete bands where any point represent a unique complete solution[1], in the sense that they provide a continuous description of the flow for all space and all time, and are physically acceptable. They conveniently divided these complete solutions into three consecutive paths in order to gain physical insight by tracing the paths chronologically, by following the point $x_R(t) = R/c_s t$ at a fixed radius R: from $t = -\infty$ when $x_R = 0^-$; through $t = 0$ when x_R goes from $-\infty$ to $+\infty$; to $t = +\infty$ when $x_R = 0^+$. This is: i) an early interior path, representing the behavior of the interior of the cloud at early times and in which the flow is everywhere subsonic; ii) an early exterior path, representing the behavior of the outer parts of the cloud it early times, but after they have been overrun by the inward propagating compression wavefront, and in which the flow is everywhere supersonic; and iii) a late path, representing the behavior of the whole cloud at late times, as it is steadily accreted by the central point mass, and in which the flow remains everywhere supersonic. They also found semi-complete solutions that describe the flow for all space and through the late era but

[1]Note that the Larson, Penston, Hunter and Shu's solutions fall at the apices of these bands

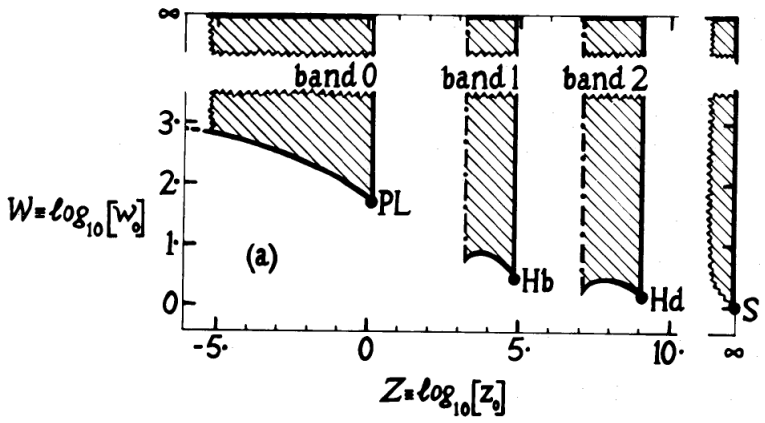

Figure 2.2 Solutions of Whitworth and Summers (1985) for the collapse of self-gravitating isothermal gas spheres fully parametrized by the initial central density (z_0) of the cloud and the central point mass originated by the collapse of the cloud (w_0), representing: intrinsically unstable (band 0), intrinsically stable (band 1) clouds, and physically unnatural solutions (Band 2 and right-hand band ∞). Jagged boundary bands extend indefinitely, except for the case of the band ∞ where the boundary is simply indeterminate.

begin in a singular manner.

It is noteworthy that the ingredient that allowed them to provide a more complete description of the collapse solutions was noting that the physically possible solutions that passed through *trans-sonic points*[1] were *nodes* (at which there are an infinity of paths that represent different combinations of two linear eigensolutions) instead of *saddles* (at which the only paths are the two linear eigensolutions). Moreover, this trans-sonic points are identified as the head of the compression wave because the density at fixed radius always increases after the pass of the wave at $t = 0$.

Band 0 solutions represent clouds whose interior is centrally rarified during early times, or clouds whose interior initially has uniform density and retains uniform density at least until overrun by the inward propagating compression wave, or clouds whose interior is initially mildly centrally peaked. On the other hand, Band 0 early interior paths, represent cloud interiors which from the outset are so far from hydrostatic equilibrium that they immediately start to contract through their entire volume, without requiring any external stimulus. Its behavior is expected to occur when a protostar forms through the break-up of a shocked gas layer, or when a previously Jeans-stable cloud is rendered Jeans-unstable by sudden cooling and/or molecular association. This is numerically reproduced by taking an equilibrium configuration and then doubling the density throughout, or by taking a density cloud with mass well in excess of the

[1] *I.e.*, where the flow goes from been supersonic to being subsonic

Jeans mass (*e.g.*, Naranjo-Romero et al., 2015).

Band 1 solutions represent clouds which are not monotonically centrally peaked (*i.e.*, can have density profiles with a local minimum). A large number of this solutions have a single sound wave propagating inwards through the cloud interior, ahead the compression wave. Band 1 early interior paths represent cloud interiors which are initially insufficiently close to hydrostatic equilibrium that overall contraction requires some external stimulus, thus this are clouds marginally Jeans unstable or previously Jeans-stable clouds that turns unstable by an increase in the external pressure.

Band 2 solutions represent clouds that are even more centrally peaked that those in Band 1, and thus Band 2 early interior paths represent cloud interiors which are initially even closer to hydrostatic equilibrium than those in Band 1. Only when the cloud interior has been overrun by the inward propagating compression wave does it convert to overall contraction; in the meantime it is traversed by a low amplitude sound waves tending to stablish hydrostatic equilibrium by redistributing the mass.

In a more general description, the behavior of the cloud exterior is given by early exterior paths describing the flow behind the inward propagating compression wavefront associated with the trans-sonic node, and that have monotonic velocity profiles with positive radial gradient, so the inward flow is always accelerated behind the compression wavefront. The compression wave creates a central point mass, leaving behind an uniform velocity field. After this (note that the subsequent behavior is described by the late paths), the central point mass grows by accretion, and a rarefaction wave propagates throughout the infalling gas adjusting the velocity to free-fall. Note that all late paths thus have monotonic velocity and velocity profiles, both with negative radial gradient. Thus, the different combination of an early interior path and a late path represent strengths of the external pressures that ultimately produce a large point mass during the late times.

Whitworth and Summers, concluded that all of Shu's solutions originated in a rather unnatural manner with density profiles infinitely centrally peaked, while Hunter's solutions whilst rather particular, are even less natural than Shu's. Hunter's solutions represent clouds whose interiors are initially close to hydrostatic equilibrium, but are overrun by an inward propagating compression wave driven by external pressure, and thus overall contraction occurs in order to form a central point mass.

2.5 Filament stability

The radial profile of the observed filaments column density is well described by a Plummer-like function (*cf.*, Whitworth and Ward-Thompson, 2001; Arzoumanian et al., 2011):

$$\rho(r) = \frac{\rho_{\rm c}}{\left[1 + (r/R_{\rm flat})^2\right]^{p/2}}, \tag{2.76}$$

where $\rho_{\rm c}$ is the central density and $R_{\rm flat}$ is the radius of its inner flat region (both parameters characterize a pure Gaussian-like inner region comprising the most central

and densest parts of the filament), and the parameter p characterize the power-law like region of the profile at large radii (*e.g.*, Rivera-Ingraham et al., 2016).

Analogous to the cloud mass in a spherical cloud, in the case of filaments, the mass per unit length (*e.g.*, Fischera and Martin, 2012) is given by:

$$\frac{M}{l}(r_{\rm cyl}) = \int_0^{r_{\rm cyl}} 2\pi r \rho(r) dr = \frac{2K}{G}\left[1 - \frac{1}{1+(r_{\rm cyl}/R_{\rm flat})^2}\right], \tag{2.77}$$

where M is the mass, and l is the length, and K is related to the gas pressure and density of the filament:

$$K = \frac{P}{\rho} = \frac{Tk_B}{\mu m_H}. \tag{2.78}$$

If the effective temperature equals the thermal or kinetic temperature, then $K = c_{\rm s}^2$. The relation between K and $R_{\rm flat}$ is:

$$R_{\rm flat} = \sqrt{2K/\pi G\rho_{\rm c}}. \tag{2.79}$$

In the limit $r_{\rm cyl} \gg R_{\rm flat}$ the mass per unit length approaches a maximum value:

$$\frac{M}{l}(r_{\rm cyl}) = \frac{2K}{G} = 16.4\left(\frac{T}{10K}\right) {\rm M_\odot pc^{-1}}. \tag{2.80}$$

Therefore, the gravitational state of the filament can be classified as:

- $\frac{M}{l} < \left(\frac{M}{l}\right)_{crit}$ subcritical,
- $\frac{M}{l} > \left(\frac{M}{l}\right)_{crit}$ supercritical.

A subcritical filament can be supported by the interior pressure against its own gravity, while a supercritical filament cannot.

Chapter 3

General observational perspectives of star formation

3.1 The Interstellar Medium

The ISM is a complex environment with three main phase components[1] regulated by several energy-injection mechanisms like supernova explosions, UV photoionizing radiation, spiral arm passage, etc., in an inhomogeneous substrate, with a wide range of properties (*e.g.*, Cox and Smith, 1974; McKee and Ostriker, 1977). In disk galaxies, the ISM is radially extended beyond the stellar disk to distances almost twice that of the stellar radius (Binney, 1998). Its different components have different scale heights (see *e.g.*, Table 1 of Boulares and Cox (1990) and also Cox (2005)) with its thickness determined by the gravitational potential of the stars and each component itself. The ISM pressure is generated by the weight of the vertical column of gas, and it diminishes with the height and thus, can be simply modeled as an stratified atmosphere (Boulares and Cox, 1990; Ferrière, 2001).

In the Milky Way (MW), approximately half the volume is filled by a hot ionized medium with $n < 0.01\,\mathrm{cm}^{-3}$ and $T_K > 10^5$K, and half is filled by some combination of warm ionized medium (WIM) and warm neutral medium (WNM) with $n \sim 0.1-1\,\mathrm{cm}^{-3}$ and kinetic temperature, T_K, of several thousand K (Cox, 2005; Kennicutt and Evans, 2012). The neutral gas is subject to a thermal instability that predicts segregation into the warm neutral and cold neutral media (CNM, Field et al., 1969), the latter with $n > 10\,\mathrm{cm}^{-3}$ and $T_\mathrm{K} < 100$ K. Observations, however, suggest that this segregation is not strict and thus, approximately 48% of the WNM may lie in the thermally unstable phase (Dickey et al., 1977; Vázquez-Semadeni et al., 2000, 2003; Gazol et al., 2001; Heiles and Troland, 2003; Kennicutt and Evans, 2012). With a mass of $10^{10}\mathrm{M}_\odot$, a 10-15% of the total mass of the Galactic disk, the ISM is an extremely dilute mixture of gas, mostly formed by atomic hydrogen (90.8% by number, 70.4% by mass), molecular or

[1] See also Table 1 of Ferrière (2001) for the descriptive physical parameters of the different components of the interstellar gas.

ionized hydrogen, helium ($\sim 9.1\%$ by number, $\sim 28.1\%$ by mass), other complex traces of heavier elements and dust, pervaded by a rather strong and irregular magnetic field and cosmic rays (Ferrière, 2001; Cox, 2005).

3.1.1 Molecular Clouds

In the Milky Way, the ISM is arranged in large-scale structures of bubble walls, clouds, sheets, and filaments of warm gas, within which close to the mid-plane there are sub-sheets and filaments of cold dense material (Cox, 2005; Kennicutt and Evans, 2012). Roughly half the interstellar mass is confined to discrete clouds occupying only ~ 2 of the interstellar volume. These interstellar clouds can be divided into (Ferrière, 2001): i) dark clouds, which are made of very cold ($T \sim 10 - 20$ K) molecular gas that block the light from background stars. ii), translucent clouds, which contain molecular and atomic gases and have intermediate visual extinctions. iii) diffuse clouds, which consist of cold ($T \sim 100$ K) atomic gas, almost transparent to the background starlight, except at some specific wavelengths.

In turn, the molecular gas is contained in discrete clouds organized hierarchically from giant complexes (namely the giant molecular clouds, GMCs, with a size L of a few tens of parsecs, a masses of $10^5{-}10^6 \mathrm{M}_\odot$, and a mean hydrogen number density $n \sim 100 - 1000\,\mathrm{cm}^{-3}$), molecular clouds ($L \sim 5 - 10\,\mathrm{pc}$, $n \sim 10^3\,\mathrm{cm}^{-3}$), clumps ($L \sim 0.5\,\mathrm{pc}$, $n \sim 10^4\,\mathrm{cm}^{-3}$) and small dense cores ($L \sim 0.1\,\mathrm{pc}$, masses of $\sim 0.3{-}10^3 \mathrm{M}_\odot$, $n \sim 10^4 - 10^6\,\mathrm{cm}^{-3}$), see *e.g.*, Larson (1981); Blitz (1993); Ferrière (2001).

Recently, *Herschel* observations (Pilbratt et al., 2010) that have mapped the sky from entire cloud complexes down to individual dense core scales (*i.e.*, from $> 10\,\mathrm{pc}$ down to $< 0.1\,\mathrm{pc}$), have revealed ubiquitous intricate networks of filamentary substructure within the MCs irrespective of their star-forming content, suggesting that the formation of filaments precedes star formation in the cold ISM, and is tied to processes acting within the clouds themselves and therefore, favoring a scenario where filaments and prestellar cores play an important role in the star formation process (*e.g.*, André et al., 2014; André, 2017). In this scenario, large-scale compressions (turbulent or not) first produce sheet-like structures which contract first along their shortest dimension to form filaments. Then, the densest filaments fragment into prestellar cores by gravitational instability above the critical mass per unit length (see also Vázquez-Semadeni et al., 2006, 2007; Gómez and Vázquez-Semadeni, 2014).

3.1.1.1 Filaments

Filamentary interstellar structure has been detected in a variety of observations since long time ago. For instance, McClure-Griffiths et al. (2006) found a network of tenuous CO filaments observed in HI self absorption, aligned with the surrounding magnetic field, with lengths of $\sim 17\,\mathrm{pc}$, widths of less than $0.1\,\mathrm{pc}$ and temperatures of $\sim 40K$. This filamentary structure has also been observed in infrared dark clouds (Busquet et al., 2013), where quiescent filaments with temperatures of $10K$ and non-thermal velocity dispersions $\sigma_{\mathrm{NT}} \sim 0.6\,\mathrm{km\,s}^{-1}$ seem to feed star forming hubs of $15K$ and $\sigma_{\mathrm{NT}} \sim 1\,\mathrm{km\,s}^{-1}$, and also with cores within the filaments separated by a length of

$\sim 0.33\,\mathrm{pc}$, consistent with fragmentation by gravitational instability of a thin gas layer threaded by magnetic fields. Moreover, the filamentary structure seem to be present in *Herschel* observations of nearby star forming molecular clouds[1], namely Orion, Taurus, Musca-Chamaeleon and Perseus, among other cold ISM individual molecular clouds, GMCs and in the Galactic plane (see André et al., 2014, and references there in). In the nearby clouds, the observed filaments are typically from $\sim 1\,\mathrm{pc}$ up to several tens of pc long, which are in general quite linear with minimal curvatures, appearing co-linear with their host MCs (André et al., 2014; André, 2017), and with a characteristic width of $\sim 0.1\,\mathrm{pc}$ (*c.f.*, Panopoulou et al., 2017). Usually, dense, self-gravitating filaments tend to be parallel to the local magnetic field, while having associated perpendicular, less dense, sub-filaments (called *striations*), through which material is funneled down to the main filament (André et al., 2014; Palmeirim et al., 2013) with typical velocities of $\sim 0.5 - 1\,\mathrm{km\,s^{-1}}$. Also, some filaments have been observed that appear to radially feed material into hubs or ridges of active clustered star formation (*e.g.*, Myers, 2009), similarly to the tenuous CO filaments mentioned before.

In order to avoid overlapped structures in the plane of the sky, the observed filaments are usually identified by analyzing the velocity channels in molecular line observations. Once a filament has been identified, its velocity centroid usually does not show much variation, and thus are considered as real velocity-coherent structures. Moreover, overlapping sub-filamentary structures ($\sim 0.5\,\mathrm{pc}$ long) with small velocity differences and linear mass densities close to the critical mass per unit length have also been identified (*e.g.*, Hacar and Tafalla, 2011; Hacar et al., 2013). These so-called *fibers* are also identified in *Herschel* data when large-scale emission is filtered out, suggesting that filaments could be bundles of smaller and more stable fibers (Hacar et al., 2013). Nevertheless not all filaments consist of multiple fiber-like structures (Cox et al., 2016). Moreover, numerical simulation of star-forming self-gravitating clouds in magnetized media suggest that these fibers could be a projection effect, and are more prone to be produced by separated density enhancements superposed along the line of sight (Zamora-Avilés et al., 2017).

In Sec. 2.5 we have seen that the radial profile of filament column density is well described by a Plummer-like function (*cf.*, Whitworth and Ward-Thompson, 2001; Arzoumanian et al., 2011). At large radii, the observed filaments usually have a fitted value of the power-law exponent $p \approx 2$, while for a theoretical isothermal gas cylinder in hydrostatic equilibrium, $p = 4$ Ostriker (1964). This difference could be due to the fact that dense filaments are not strictly isothermal, and thus, a polytropic equation of state with polytropic index $\gamma \lesssim 1$ describe it more exactly as has been suggested (*e.g.*, Palmeirim et al., 2013). We will discuss an alternative explanation to the discrepancy in the values of p, later in Chap. 6, suggesting that filaments are not hydrostatic but are collapsing structures immersed in large scale collapsing clouds in the GHC scenario. In fact, models of polytropic cylindrical filamentary clouds ongoing gravitational contraction have density profiles scaling as $r^{2/(2-\gamma)}$ (Kawachi and Hanawa, 1998; Nakamura and Umemura, 1999). In nearby clouds, the averaged diameter of the flat inner part of the radial profile of the observed filaments is roughly constant, and it has been suggested that the filament width corresponds to the sonic scale at which interstellar

[1]Here after we will use the term "filament" to refer to molecular filaments.

turbulence becomes sub-sonic in the diffuse, non-star forming molecular gas (*e.g.*, Arzoumanian et al., 2011; Federrath, 2016), while for denser filaments that are expected to radially contract with time, this width could be significantly overestimated by up to a factor of a few (Seifried et al., 2017). On the other hand, recent works have suggested that this quasi-universality is a bias due to the method and choice of parameters used in measuring the filament widths (Panopoulou et al., 2017), (see also Ntormousi et al., 2016; Seifried et al., 2017; Green et al., 2017).

3.1.1.2 Dense cores

Prestellar cores are observationally identified as not very elongated patches in submillimeter/millimeter continuum emission or optically/infrared absorption and also, can be identified in line emission of molecules that do not suffer from freeze-out[1] in the cold dense gas (*e.g.*, André et al., 2010, 2014). The density structure of dense cores is very similar to that of a self-gravitating isothermal sphere that is critically stable according to the Bonnor-Ebert (BE) criteria (Ebert, 1955; Bonnor, 1956), bounded by the external pressure of its parent cloud (*e.g.*, Alves et al., 2001; Tafalla and Hacar, 2015). Simpson et al. (2011) have proposed that cores evolve by accreting mass quasi-statically, maintaining Bonnor-Ebert equilibrium and increasing in both mass and radius. When a core crosses the limit of gravitational instability, it begins to collapse, decreasing in radius. Nevertheless, Ballesteros-Paredes et al. (2003) have shown that even dynamical structures can produce BE column density profiles, although with significant differences between apparent and actual temperatures and with central densities obtained with the BE fit that tend to be smaller than the actual central densities of the cores. They also found that different projections of the same core may give very different values of the BE fits, and thus fitting BE profiles to the observed cores is not an unambiguous test of hydrostatic equilibrium.

Moreover, *Herschel* observations have shown that $\sim 70\%$ of the bound prestellar cores and embedded protostars are located within supercritical[2] filaments with $N_{H2} \gtrsim 7 \times 10^{21}\,\mathrm{cm}^{-2}$ (*e.g.*, Polychroni et al., 2013). The rest of the prestellar core population is not associated with any filament or only associated with subcritical filaments and thus, are less massive (*e.g.*, Polychroni et al., 2013). In this picture, complex networks of long, thin filaments seem to form first within molecular clouds, and then the densest filaments fragment into a number of prestellar cores (André et al., 2010). In this case, one would expect that the cores and their associated filaments have similar kinematic properties (André et al., 2014).

It also has been suggested that prestellar cores could grow by filamentary accretion (*e.g.*, Falgarone et al., 2001; Smith et al., 2011; Cox et al., 2016; Salji et al., 2015), (see also Balsara et al., 2001). Moreover, numerical simulations have suggested that filaments represent the locus where the flow radially accreted from the cloud is redirected down to the dense cores within. In this case, the longitudinal draining of the filament's material accreted directly to its embedded cores would produce enhanced

[1] Due to the formation of ice mantles around refractory grain particles.

[2] *I.e.*, with mass per unit length $M_{\mathrm{line}} > M_{\mathrm{line,crit}}$, where the latter is the threshold value for gravitational collapse. We will return to this later in Chap. 6

star formation, in contrast to isolated prestellar cores (Gómez and Vázquez-Semadeni, 2014).

3.1.2 Scaling relations

Molecular clouds and their substructure appear to follow scaling relations first noted by Larson (1981) and later by other observational works (*e.g.*, Dame et al., 1986; Solomon et al., 1987; Falgarone et al., 1992; Caselli and Myers, 1995; Heyer and Brunt, 2004):

$$\sigma \sim L^{\beta}, \tag{3.1}$$

$$\rho \sim L^{-\alpha}, \tag{3.2}$$

where ρ is the gas density, σ is the linewidth and L the size. The most favored values for the exponents are $\alpha \approx 1$ and $\beta \approx 0.5$ (Ballesteros-Paredes et al., 2011, and references therein). These relations are valid in a range of six orders of magnitude in size, from the scale of the dense clumps up to the scale of large cloud complexes ($0.1 < L < 100\,\mathrm{pc}$). Since the ratio $2GM/\sigma^2 R$, [1] is roughly constant, they have been interpreted as virial balance between the gravitational energy and the kinetic energy (*i.e.*, $2E_k = |E_g|$) (*e.g.*, Larson, 1981; Myers and Goodman, 1988). Nevertheless, the fact that $\alpha \approx 1$ in the second relation, would imply that the column density $N = nL$ is approximately constant.

3.1.2.1 A generalization of the scaling relations in MCs

Recently, Heyer et al. (2009) re-examined the MC scaling relations by comparing the Solomon et al. (1987) data and new data from ^{13}CO (J=1–0) emission as a lower opacity tracer of molecular clouds. They found that these relations seem to be instead replaced by a single relation where:

$$\sigma_v / R^{1/2} \propto \Sigma^{1/2}, \tag{3.3}$$

where the LHS is known as the Larson ratio, $R = L/2$ is the radius, and Σ[2] is the surface density. They claim that this relation is consistent with clouds being in self-gravitational equilibrium. Nevertheless, Ballesteros-Paredes et al. (2011) pointed out that this relation is also consistent with the clouds in a state of free-fall towards their center of mass. We will discuss this later in Sec. 4.3. Moreover, Dobbs et al. (2011) argued that Heyer's results would imply that the molecular clouds are preferably gravitationally unbound. Later, Ibáñez-Mejía et al. (2016) and Camacho et al. (2016), however, have shown that the dense clumps in numerical simulations follow this generalized energy equipartition relation and they interpret this relation as a natural consequence of gravitational contraction at all scales rather than virial equilibrium. See also Fig. 3.1.

[1] where $R = L/2$ is implied by these relations

[2] Where $\Sigma = \mu m_H N$, and for the molecular gas ($\mu = 2.36$), $1\mathrm{M}_\odot\,\mathrm{pc}^{-2} = 5.30 \times 10^{19}\,\mathrm{cm}^{-2}$.

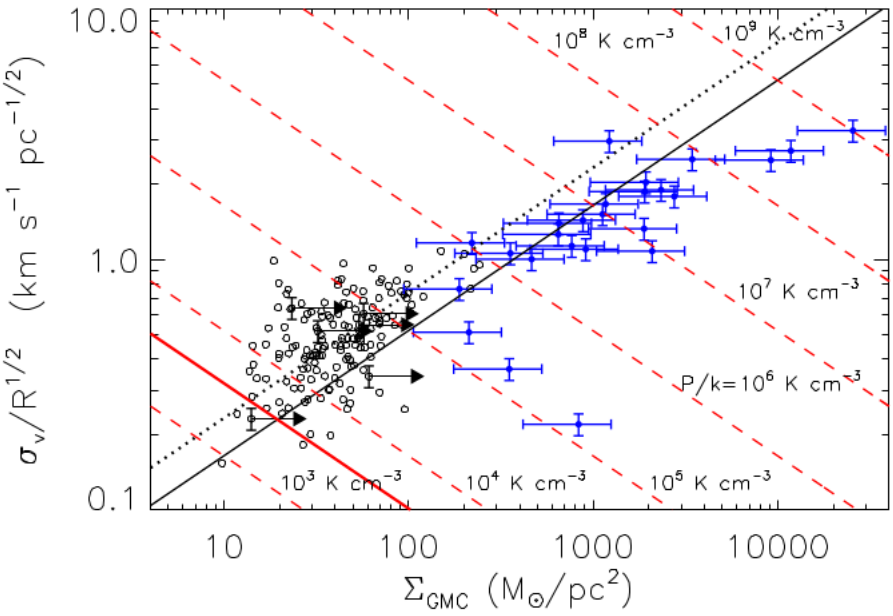

Figure 3.1 The variation of $\sigma_v/R^{1/2}$ with surface density Σ, for Milky Way GMCs from Heyer et al. (2009) (black circles) and massive cores from Gibson et al. (2009) (blue points). The solid and dotted black lines show loci corresponding to gravitationally bound and marginally bound clouds respectively. The red dashed lines represent the locus of constant turbulent pressure, while the red solid line represent the mean thermal pressure of the local ISM. From the review of Dobbs et al. (2014). See also Ballesteros-Paredes et al. (2011).

3.1.3 A "transition to coherence"

Dense cores exhibiting non-thermal velocity dispersions smaller than thermal motions have been observed for a long time (*e.g.*, Goodman et al., 1998). In particular, Myers (1983) concluded that all of the Larson relations found for supersonic regions in fact extend into the subsonic regime and that if a turbulent energy cascade is present in dense cores, then the dissipation of turbulence would be important for cloud heating and star formation. Later, Barranco and Goodman (1998), Goodman et al. (1998) and Caselli et al. (2002) found evidence of a so-called *transition to coherence*, where "coherence" means that the non-thermal, turbulent, contributions to the line width are so small that the observed velocity dispersion is nearly the sonic one and independent of scale within the core. Thus, they interpreted this behavior as a transition between the outer turbulent gas and the more quiescent gas close to the cores, taking place in regions of ~ 0.1 pc, forming primarily low-mass stars. Moreover, recent observations (Pineda et al., 2010) have apparently observed this transition from a supersonic turbulent ve-

locity dispersion down to a subsonic one (decreasing by a factor of 2, corresponding to $\sim 3\,\mathrm{km\,s^{-1}pc^{-1}}$) occurring over a physical scale of 0.06 pc, see also Fig. 3.2. Even though the typical size of the sonic region is in rough agreement with the observed width of filaments in *Herschel* data (André et al., 2014), this has been known to be the mean size of low-mass pre- and protostellar cores (*e.g.*, Jijina et al., 1999). Moreover, Palau et al. (2015), combining interferometric and single-dish data of relatively nearby massive dense cores that are actively forming stars, tested their "fragmentation level" at scale of ~ 0.1 pc and find that the best correlation between fragmentation level, velocity dispersion, and number of fragments is more consistent with pure thermal Jeans fragmentation than turbulent fragmentation (see also the review of Dobbs et al., 2014). Thus, no turbulence dissipation would be needed for the cloud to be fragmented into dense cores.

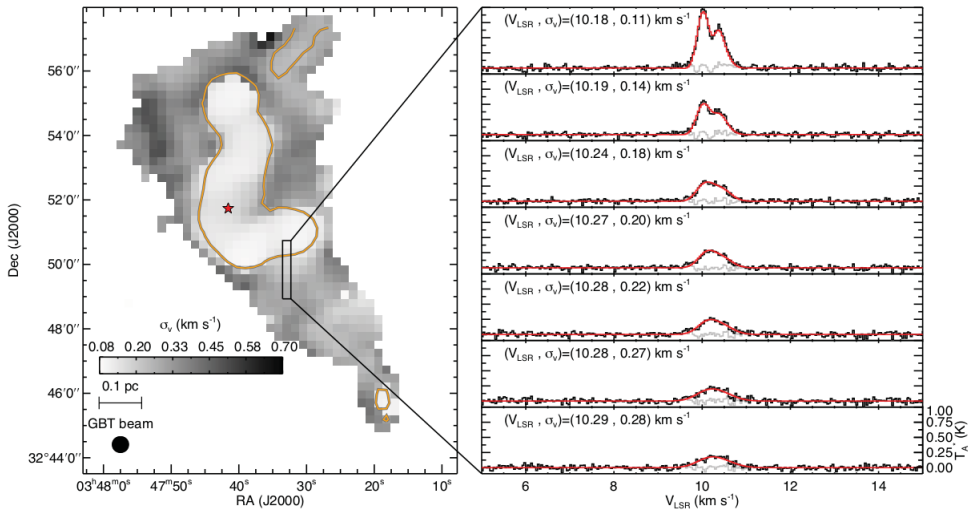

Figure 3.2 Left panel: Velocity dispersion map derived from fitting all NH_3 (1,1) hyperfine components simultaneously. Right panel: Spectra of the main components of the NH_3 line, showing the centroid velocity and velocity dispersion for each position away from the protostar. The image shows two main components (top) clearly separated due to their low velocity dispersion (the coherent core), while outwards from the core the lines get weaker and broader. From Pineda et al. (2010).

Chapter 4

Star formation

4.1 Early scenarios of star formation

Giant molecular clouds have been generally considered to be dense virialized structures in the interstellar medium (*e.g.*, Larson, 1981; Shu et al., 1987; McKee, 1989; Mouschovias, 1991), with molecular-line widths corresponding to velocities larger than their thermal speeds by about an order of magnitude (Wilson et al., 1970), and relatively long lifetimes with respect to their free-fall time (Blitz and Shu, 1980). Initially, Goldreich and Kwan (1974) found that the derived rate at which energy is radiated from the optically thick CO lines exceeds the rate at which work is done by an adiabatic compression of collapsing gas, implying the existence of an energy source which maintains the temperature of the gas against the cooling due to radiative energy losses. Thus, they suggested that MCs are in a state of gravitational collapse, and the observed large motions can be interpreted as its manifestation. Shortly thereafter, Zuckerman and Evans (1974) suggested that if molecular clouds were in a state of global contraction, they would exhibit systematic Doppler shifts (by comparison of molecular lines from the center and the periphery), which were not observed. Therefore they conclude that the observed data were dominated by local motions contained in fragments of $\sim 1000 M_\odot$. Moreover, Zuckerman and Palmer (1974) noted that if MCs were in a state of gravitational collapse, then their Star Formation Rate (SFR) should be roughly two orders of magnitude larger than the observed Galactic SFR ($\sim 2 M_\odot\,\mathrm{yr}^{-1}$; Chomiuk and Povich (2011)).

4.2 Support mechanisms against collapse

4.2.1 The magnetic support scenario

From the late 1970s to the late 1990s, the prevailing model for the state of MCs and the regulation of star formation was based on the notion of magnetic support for the clouds (*e.g.*, Shu et al., 1987; Mouschovias, 1991). See also the review of (Vazquez-Semadeni, 1997). A problem with the Larson relations was that the observed linewidths imply

highly supersonic turbulence in the form of random motions, that should produce shocks and rapidly dissipate, becoming subsonic (Mestel, 1965). At first, magnetic fields were proposed as an alternative through Alfvén waves, which does not induce shocks, and additionally that for clouds with a nearly critical max-to-flux ratio, the Alfvén velocity nearly equals the virial velocity[1] (Shu et al., 1987; Mouschovias, 1987). As noted in Sec. 2.4.6, magnetically subcritical clouds can be supported against their self-gravity by magnetic forces. This in fact would lead to no star formation at all. Since MCs are only partially ionized[2], however, a small fraction of the MCs mass is allowed to collapse by the process known as *ambipolar diffusion* (AD), which can be understood as follows.

In a partially ionized medium such as an MC, the neutral particles are only indirectly coupled to the magnetic field, through their collisions with the ions, which are the only ones that experience the Lorentz force. When such a medium is located in a gravitational potential well, the neutrals then tend to slip through the ions and sink deeper into the potential well. This causes a redistribution of the magnetic flux, which remains distributed over a large region, while the mass falls to the central most parts of the cloud (a dense core). Thus, in practice, the dense cores increase their mass-to-flux ratio, and eventually become magnetically supercritical, while their envelopes remain magnetically subcritical, and thus supported against collapse. This situation allows gravitational collapse of a small fraction of the mass of a magnetically subcritical cloud.

Following the AD model, globally magnetically subcritical clouds subject to AD correspond to low-mass star-forming regions, where the SFR and Star Formation Efficiency (SFE) are low, and no massive stars form. On the other hand, if an MC happened to be magnetically supercritical as a whole, then it would not be supported by magnetic forces, and will proceed to collapse as a whole. This case would give rise to high SFRs and SFEs, and to the formation of massive stars, thus, in the magnetic support model, magnetically supercritical clouds correspond to massive star-forming regions.

4.2.2 The turbulent support scenario

The magnetic support scenario began to be disfavored some 15 years ago because numerical simulations showed that MHD turbulence dissipates as rapidly as pure hydrodynamic turbulence (Mac Low et al., 1998; Stone et al., 1998; Padoan and Nordlund, 1999; Avila-Reese and Vázquez-Semadeni, 2001). Moreover, in the last decade Zeeman observations revealed that GMCs tend in general to be magnetically supercritical (*e.g.*, Bourke et al., 2001; Crutcher et al., 2010), and thus the magnetic field cannot provide support for most clouds. Thus, the previous magnetic interpretation of near-equipartition between the non-thermal motions and the gravitational energy in GMCs and their substructure (Larson, 1981; Heyer et al., 2009) was modified by the notion that the non-thermal motions correspond to strongly supersonic turbulence, even though it is well known that it requires continuous driving in order to be maintained (*e.g.*, Vazquez-Semadeni et al., 2000; Mac Low and Klessen, 2004; Ballesteros-Paredes

[1] A result obtained by equating magnetic and potential energies.

[2] MCs have an ionization fraction $\sim 10^{-5}$ or less.

et al., 2007; McKee and Ostriker, 2007). The main driving mechanisms invoked were feedback by supernovae and HII regions in massive star forming regions, massive-star winds, protostellar outflows, the passage of spiral density waves, together with magneto-rotational instabilities in the ISM (*e.g.*, Mac Low and Klessen, 2004). In this so-called *turbulent support* scenario, it has been proposed that the giant molecular clouds form as density fluctuations induced by larger-scale interstellar turbulence (see Ballesteros-Paredes et al., 1999) in the warm phase, via compressible motions such as those resulting from thermal instabilities or from the passage of shock fronts. On the other hand, the velocity fluctuations in molecular clouds are known to be $\sigma_v \sim 2 - 5\,\mathrm{km\,s^{-1}}$ while the sound speed is $c_\mathrm{s} \sim 0.2\,\mathrm{km\,s^{-1}}$, and thus they are strongly supersonic with Mach number $\mathcal{M}_s \sim 5 - 20$. Thus, the overall picture in this scenario is that the supersonic turbulence supports the clouds globally, while simultaneously it produces local nonlinear density fluctuations (the clumps and cores). These small-scale fluctuations suffer a local reduction of the Jeans mass, and therefore become gravitationally unstable and collapse before their immediate parent structures do.

4.3 The global hierarchical collapse (GHC) scenario

Although the turbulent support scenario has been successful in roughly reproducing the observed mass distribution of turbulent density fluctuations (Padoan and Nordlund, 2002; Hennebelle and Chabrier, 2008; Hopkins, 2012), it has been recently proposed that the near-equipartition may be a consequence of gravitational collapse rather than to virial equilibrium. In particular, Ballesteros-Paredes et al. (2011) conclude that although hydrodynamic turbulence is necessary to produce the first condensations, the forming clouds eventually become bounded and thus gravitational accelerations dominate the motions within them. In particular they argued that during the cloud's collapse, the density and the internal pressure increase, and once the collapse has advanced sufficiently, the external pressure becomes negligible. They argued that energy conservation implies that the kinetic energy gained during cloud's collapse must come from the gravitational energy released (*i.e.*, $|E_\mathrm{k}| \approx E_\mathrm{g}$) and thus $\sigma_v^2 \approx 2G\Sigma R$, where Σ is the surface density. Note that this relation is very similar to that from the virial relation $\sigma_v^2/R \approx G\Sigma$, and therefore collapse is also in agreement with observational data (*e.g.*, Heyer et al., 2009). Moreover, they interpreted the scatter in the $\sigma_v - R$ plane and the dependence of the velocity dispersion on the surface density ($\sigma_v^2/R \propto \Sigma$) as the molecular clouds being in a state of hierarchical and chaotic gravitational collapse, *i.e.*, developing local centers of collapse throughout the whole cloud while the cloud itself is also collapsing, making equilibrium unnecessary at all stages prior to the formation of actual stars.

The still common virial-equilibrium interpretation, through the idea that stellar-driven turbulence produces a hypothetical turbulent pressure that provides support against cloud's self-gravity, seems to face further problems. In particular, clouds with little or no ongoing star formation also show near-equipartition (*e.g.*, Maddalena and Thaddeus, 1985), suggesting that local stellar feedback cannot be the driver of the non-thermal motions. Even more, there seems to be no apparent reason why molecular

clouds should adjust themselves to balance the local-scale energy injection to maintain a near-equilibrium at the larger scale of the whole cloud. Although it would be possible to fulfill this condition in some idealized models in which local star formation is self-regulated (*e.g.*, Krumholz et al., 2006; Goldbaum et al., 2011), at least for clouds with masses $< 10^6$ $M_\odot$, full numerical simulations of ionization by feedback suggest that when star formation is fully active overall in the cloud, it evaporates and partially tears apart the parent cloud, disrupting it (Vázquez-Semadeni et al., 2010; Colín et al., 2013; Dale et al., 2012, 2013). More recently, Colín et al. (2013) have found that clouds can appear in near equipartition before stellar feedback begins to dominate the dynamics, and are disrupted once feedback dominates.

Vázquez-Semadeni et al. (2009) and Gómez and Vázquez-Semadeni (2014) proposed a return to the globally collapsing scenario, but instead of being monolithic as initially proposed by Hoyle (1953), the collapse is instead hierarchical and filamentary. In this scenario, the collapse initiates in a turbulent background containing non-linear density fluctuations. The molecular clouds are born turbulent and in a state of global collapse, but have a large collapse time-scale in comparison to their embedded density fluctuations, due to their higher densities. In particular, Heitsch and Hartmann (2008) found that turbulence generated through the cloud formation process provides a mechanism to produce thermal and dynamical fragmentation, which is highly efficient in generating cold, high-density cloudlets. They claim that while the turbulence might slightly decay during the formation of the cloud in the atomic phase, turbulence increases due to gravity during the molecular phase of the cloud formation, in agreement with other numerical works (Vazquez-Semadeni, 1998; Vázquez-Semadeni et al., 2007, 2008; Field et al., 2008; Klessen and Hennebelle, 2010; Robertson and Goldreich, 2012; Murray and Chang, 2015). Thus, molecular clouds consist of a hierarchy of collapses within collapses in the large-scale ISM, rather than actual random turbulence entities. Moreover, Vázquez-Semadeni et al. (2010); Zamora-Aviles and Vazquez-Semadeni (2013) argued that it is possible to destroy molecular clouds early in their evolution by stellar feedback, even before $\sim 10\%$ of their mass is converted into stars, thus solving the Star Formation Rate (SFR) conundrum of Zuckerman and Palmer (1974), (see also Dale et al., 2012; Zamora-Avilés et al., 2012; Colín et al., 2013; Zamora-Avilés and Vázquez-Semadeni, 2014)

4.3.1 The hierarchical fragmentation model

In the GHC scenario (see Vázquez-Semadeni et al., 2010, for a review), the picture is similar to that in the turbulent model, except that the clouds themselves are assumed to undergo a long formation and evolutionary process. The clouds are born as the result of transonic compressions in the warm atomic gas, as thin, low-column density cold atomic clouds (Vázquez-Semadeni et al., 2006). The clouds keep accreting mass for a long time (~ 20 Myr) from the reservoir of material that originated the compression. At the locus of the cloud, the collisions of the streams drive only moderately supersonic turbulence, $\mathcal{M} \sim 3$, in agreement with other numerical works (*e.g.*, Koyama and Inutsuka, 2002; Audit and Hennebelle, 2005; Heitsch et al., 2005) and observations of the cold atomic gas (Heiles and Troland, 2003). At the time of the formation of the cloud, no collapse

occur inside the clouds because the turbulent velocity field is not strong enough to produce local decreases in the Jeans mass. Thus, the role of the turbulence is simply to provide shocks that dissipate the supporting kinetic energy and generate structure that act as seeds for the subsequent fragmentation (Clark and Bonnell, 2005). A few Myr later, the thin-sheet clouds acquire enough mass to exceed their own Jeans mass and begin to globally collapse. While this occurs, the average Jeans mass of the clouds become smaller and smaller until it reaches the typical masses of turbulent clumps, and thus, these structures collapse locally with shorter free-fall times than the large scale collapsing structure. Moreover, the Star Formation Rate (SFR) increases in the parent cloud due to the availability of more and more turbulent fluctuations originated by the increasing density in the parent cloud and the reduction of the average Jeans mass. The final stage in this scenario is the destruction of the clouds by energy feedback of stars formed in the process, when $\sim 10\%$ of the cloud's mass has been converted to stars (Zamora-Avilés et al., 2012; Zamora-Avilés and Vázquez-Semadeni, 2014).

Chapter 5

Prestellar cores

In this chapter we present the numerical work of the early stages in the evolution of prestellar cores that Naranjo-Romero et al. (2015) has developed as part of the present thesis. This work has been motivated by recent numerical studies that suggest that the picture of gravitational collapse is not limited to the scale of dense cores, but instead may extend to the scale of the whole cloud (*e.g.*, Vázquez-Semadeni et al., 2007, 2009, 2010, 2011; Heitsch and Hartmann, 2008; Heitsch et al., 2008) and several observational studies that have shown that the gravitational collapse extends at least to parsec scales (*e.g.*, Galván-Madrid et al., 2009; Peretto et al., 2013; Polychroni et al., 2013). In particular, Ballesteros-Paredes et al. (2011), extending the data presented by Heyer et al. (2009), have shown that the energy budget of giant molecular clouds and high-mass star-forming clumps alike is consistent with generalized free-fall in these structures. In this case, what has been previously interpreted as virialization, may just as well be interpreted as free-fall.

In this paper, we have tested this hypothesis modeling a prestellar core as a small-amplitude fluctuation embedded in a gravitationally unstable uniform density background. Our initial setup is similar to previous studies of the collapse of clouds that are initially centrally peaked (Larson, 1969; Penston, 1969; Whitworth and Summers, 1985), our setup is far from hydrostatic equilibrium and collapses immediately. The main distinction is the inclusion of a uniform background which is itself highly Jeans unstable and thus also engaging in the collapse, as prescribed for molecular clouds in the GHC scenario.

The Astrophysical Journal, 814:48 (11pp), 2015 November 20 doi:10.1088/0004-637X/814/1/48

HIERARCHICAL GRAVITATIONAL FRAGMENTATION. I. COLLAPSING CORES WITHIN COLLAPSING CLOUDS

Raúl Naranjo-Romero, Enrique Vázquez-Semadeni, and Robert M. Loughnane
Instituto de Radioastronomía y Astrofísica, Universidad Nacional Autónoma de México, Apdo. Postal 3-72, Morelia, Michoacán, 58089, México
Received 2015 June 5; accepted 2015 October 14; published 2015 November 17

ABSTRACT

We investigate the Hierarchical Gravitational Fragmentation scenario through numerical simulations of the prestellar stages of the collapse of a marginally gravitationally unstable isothermal sphere immersed in a strongly gravitationally unstable, uniform background medium. The core developes a Bonnor–Ebert (BE)-like density profile, while at the time of singularity (the protostar) formation the envelope approaches a singular-isothermal-sphere (SIS)-like r^{-2} density profile. However, these structures are never hydrostatic. In this case, the central flat region is characterized by an infall speed, while the envelope is characterized by a uniform speed. This implies that the hydrostatic SIS initial condition leading to Shu's classical inside-out solution is not expected to occur, and therefore neither should the inside-out solution. Instead, the solution collapses from the outside-in, naturally explaining the observation of extended infall velocities. The core, defined by the radius at which it merges with the background, has a time-variable mass, and evolves along the locus of the ensemble of observed prestellar cores in a plot of $M/M_{\rm BE}$ versus M, where M is the core's mass and $M_{\rm BE}$ is the critical BE mass, spanning the range from the "stable" to the "unstable" regimes, even though it is collapsing at all times. We conclude that the presence of an unstable background allows a core to evolve dynamically from the time when it first appears, even when it resembles a pressure-confined, stable BE-sphere. The core can be thought of as a ram-pressure confined BE-sphere, with an increasing mass due to the accretion from the unstable background.

Key words: evolution – gravitation – ISM: clouds – ISM: kinematics and dynamics

1. INTRODUCTION

1.1. The Scenario of Hierarchical Gravitational Collapse

Molecular clouds (MCs) are associated with the bulk of star formation in the Galaxy. With supersonic linewidths (Wilson et al. 1970) that scale as $R^{1/2}$, where R is the cloud's radius (Larson 1981; Solomon et al. 1987), and low star formation efficiencies (Myers et al. 1986). MCs have traditionally been interpreted as being in a global state of virial equilibrium between supersonic turbulence and self-gravity. On the smallest scales, when the density increases, the turbulence is believed to dissipate, allowing collapse to proceed (Goodman et al. 1998; Tafalla et al. 2002; Pineda et al. 2010).

However, recent numerical studies suggest that the picture of gravitational collapse is not limited to the scale of dense cores, but instead may extend to the scale of the whole cloud (e.g., Vázquez-Semadeni et al. 2007, 2009, 2010, 2011; Heitsch & Hartmann 2008; Heitsch et al. 2008). Moreover, several observational studies have shown that gravitational collapse extends at least to parsec scales (e.g., Galván-Madrid et al. 2009; Schneider et al. 2010; Peretto et al. 2013; Polychroni et al. 2013). Finally, Ballesteros-Paredes et al. (2011), extending the data presented by Heyer et al. (2009), have shown that the energy budget of giant molecular clouds (GMCs) and high-mass star-forming clumps alike is consistent with generalized free-fall in these structures. In this case, what has been previously interpreted as virialization, may just as well be interpreted as free-fall, within the uncertainties, and in fact, the data are marginally more consistent with free-fall than with virial equilibrium.

In addition, recent observations (e.g., Gutermuth et al. 2008; Myers 2009; André et al. 2010; Men'shchikov et al. 2010; Molinari et al. 2010; Arzoumanian et al. 2011) have revealed a vast network of filaments everywhere inside the MCs, feeding the clumps and the dense cores. Numerical simulations of cloud formation (e.g., Burkert & Hartmann 2004; Hartmann & Burkert 2007; Vázquez-Semadeni et al. 2007, 2009, 2011; Heitsch et al. 2009; Gómez & Vázquez-Semadeni 2014) also exhibit such filamentary structure, and Gómez & Vázquez-Semadeni (2014) and Smith et al. (2014) have interpreted it as the consequence of anisotropic, large-scale gravitational collapse in the clouds. Observations of the kinematics in the filaments (Schneider et al. 2010; Kirk et al. 2013; Peretto et al. 2014) are consistent with the kinematics seen in those simulations.

In the scenario of global hierarchical gravitational collapse and fragmentation, then, the entire cloud is gravitationally collapsing. This is possible because of the coherent production of cold atomic gas over large scales by large-scale shock-compressed layers in the warm, diffuse medium, which trigger thermal instability and a phase transition to the cold phase (Ballesteros-Paredes et al. 1999; Hennebelle & Pérault 1999; Koyama & Inutsuka 2000, 2002; Audit & Hennebelle 2005; Heitsch et al. 2005; Vázquez-Semadeni et al. 2006). The cold cloud formed by this mechanism is supersonically turbulent, albeit, only moderately. Within these large-scale unstable clouds, small-scale, nonlinear density fluctuations produced by turbulence terminate their collapse before the cloud at large does, because their free-fall times are shorter (Heitsch & Hartmann 2008). This implies that the clumps and cores constitute smaller-scale collapse events embedded within larger-scale ones (at the whole cloud scale), amounting to a hierarchical state of collapse that is moreover chaotic (with multiple collapse centers and irregular geometries). Thus, in this paper we investigate the collapse of an unstable core embedded in a larger, also unstable cloud.

1.2. Core Collapse Theory

Within this scenario of global, multi-scale collapse, it is pertinent to re-examine some classical and recent works on the collapse of dense cores. The seminal works of Larson (1969) and Penston (1969), to which we collectively refer to as LP, independently found solutions in which collapse proceeds outside-in, developing an r^{-2} density profile in the core envelope and a velocity profile that approaches a constant value as the core accretes mass from its envelope. Larson (1969) considered uniform initial densities, while Penston (1969) considered slightly centrally condensed density configurations. Thus, they considered the collapse starting from times earlier than the development of a singularity (the protostar).

Shu (1977, hereafter S77) studied this problem analytically, adopting a singular isothermal sphere (SIS) as the initial *equilibrium* condition. This implies that he only considered the evolution starting from the time of protostar formation. He assumed that the SIS is somehow destabilized at $t = 0$, causing the innermost regions to begin collapsing, and producing a rarefaction wave that propagates outwards, leaving a free-falling ($\rho \propto r^{-3/2}$, $v \propto r^{-1/2}$) region behind it, while the region outside the front remains static. This is the well-known "inside-out" collapse solution, which is generally assumed to represent the velocity field inside the cores.

Some time later, Whitworth & Summers (1985, hereafter WS85) investigated the parameter space of the initial conditions, finding that the latter can be parametrized by the initial density and the mass at the center of the collapsing cloud. WS85 broadly divided these solutions in three bands (see Figure 2 of that paper), considering, in general, the contraction from times earlier than the formation of the singularity. In particular, they noted that, if the collapsing core starts out very far from equilibrium, it starts to contract immediately at all radii. In this case, the overall evolutionary pattern consists of a compression wave that starts far from the core's center and propagates *inwards*. This wave front divides the core into an inner ($r < r_{\rm f}$, where $r_{\rm f}$ is the instantaneous radial position of the front) and an outer ($r > r_{\rm f}$) region. The transition between the two regions is smooth, in spite of the fact that eventually supersonic speeds develop in the outer region. The density profile in the inner region is nearly uniform, while outside of the front it decays as r^{-2}. The velocity profile is linear with radius in the inner region, and uniform in the outer region. When the wave front reaches the center, a point of finite mass is formed at the center (the protostar), and a rarefaction wave propagates outward, leaving behind free-fall density and velocity profiles.

Using numerical simulations, Foster & Chevalier (1993, hereafter FC93) investigated the collapse of thermal-pressure bounded spheres near hydrostatic equilibrium, finding results consistent with the LP solution, and confirming that supersonic velocities develop in the outer region, and eventually reach the center. More recently, Simpson et al. (2011) have suggested that prestellar cores accrete quasi-statically until they reach their Jeans mass, and from that point onwards the cores collapse dynamically. However, if the core is accreting it is hard to understand why it would be hydrostatic out to a certain radius in the first place. Mohammadpour & Stahler (2013, hereafter MS13; see also Vorobyov & Basu 2005) have explored a new set of boundary conditions for the problem, using inflow boundaries, across which gas enters subsonically, representing accretion onto the core. They again found that supersonic velocities develop near the time of protostar formation, and concluded that such a setup may not be realistic, and that magnetic support may be necessary in order to prevent supersonic infall velocities at the time of protostar formation, as seemingly required by observations that low-mass cores generally have subsonic infall velocities (e.g., Lee et al. 1999, 2001; Tafalla et al. 2004; Pineda et al. 2010).

In addition, there is the well-known "luminosity problem" (e.g., Kenyon et al. 1990) for Class 0 and Class I sources, namely that their low luminosities would imply low accretion rates, and therefore low infall speeds, if the material were to accrete directly onto the protostellar surface. However, a number of authors (e.g., Kenyon & Hartmann 1995; Whitworth & Ward-Thompson 2001; Dunham & Vorobyov 2012) have argued that this problem can be solved if the accretion of material does not occur directly onto the protostar, but first onto a disk and from there onto the protostar, and in an episodic rather than uniform manner. Therefore, in this paper we shall not be concerned with the luminosity problem.

1.3. Starless and Prestellar Cores

Traditionally, dense cores within MCs have been classified as belonging to either of two main sub-classes, namely starless and protostellar, depending on whether they lack or contain protostellar objects, respectively. The "starless" class includes both cores that may never form stars as well cores that will eventually do so; the latter are called "prestellar," and operationally defined as a gravitationally bound starless core (e.g., André et al. 2014, p. 27). Starless cores that appear unbound are thought to require external pressure confinement (e.g., Bertoldi & McKee 1992; Lada et al. 2008). Interestingly, Foster et al. (2009) found that almost all cores in Perseus, even prestellar cores, seem to be gravitationally bound (see Figure 11 in their paper), although it should be noted that Perseus cores are more massive than those in the Pipe Nebula, which appear pressure-confined (e.g., Lada et al. 2008). As already mentioned in Section 1.2, prestellar cores exhibit infall profiles suggesting subsonic infall velocities (Lee et al. 1999, 2001; Tafalla et al. 2004), although Lee et al. (2001) noted that the inward motions are too extended to be consistent with the inside-out collapse model of S77.

Observations (e.g., Alves et al. 2001; Lada et al. 2007, p. 3) have shown that prestellar cores have a Bonnor–Ebert (BE)-like (Ebert 1955, 1957; Bonnor 1956) density profile which is nearly flat in the innermost region, while at larger radii resembles a SIS density profile ($\rho \sim r^{-2}$). It is worth noting that these profiles represent, respectively, the regular and singular solutions of the Lane–Emden equation of *hydrostatic* balance, although there have been suggestions that cores formed by strong turbulent compressions can also evolve along a sequence of BE-like density profiles (Ballesteros-Paredes et al. 2003; Gómez et al. 2007; Gong & Ostriker 2009). On the other hand, Keto et al. (2015) have concluded, by comparing synthetic line profiles of several different models of gravitational collapse with observations of the L1544 core, that only the quasi-equilibrium contraction of an unstable BE-sphere (Keto & Caselli 2010) is consistent with the observations. However, in this case, the initial BE-like profile is an assumed initial condition, rather than an outcome of the simulations.

1.4. This Work

In the present paper, we investigate a more unified scenario of the gravitational collapse of cores based on the notion that MCs are collapsing as a whole, and that cores form, grow and collapse within this globally collapsing environment. We start with a generic low-amplitude Gaussian density fluctuation, to which we refer to as "the core," embedded within an unstable uniform density distribution, to which we will refer to as "the cloud," allowing the core to develop its density and velocity profiles self-consistently as it grows within the medium, thus relaxing any initial assumptions about those profiles. This study can be considered an extension of the work of MS13, by allowing the presence of a large envelope of uniform density, which represents the "background" often present in observations of cores (e.g., André et al. 2014, p. 27).

The paper is structured as follows: in Section 2 we describe the numerical simulation. The results from the simulations are described in Section 3. In Section 4.1 we compare the results of the simulation with observations, in particular in terms of the locus of observed cores in a diagram describing core stability, while in Section 4.2, we discuss the evolution of the dense cores in the context of earlier analytical solutions. Next, in Section 4.3 we discuss some implications of our results. Finally, in Section 5 we present a summary and some conclusions.

2. THE SIMULATIONS

We have performed numerical simulations of the collapse of a spherically symmetric clump inside a collapsing cloud, using a spectral, fixed mesh numerical code (Leorat et al. 1990; Vázquez-Semadeni et al. 2010). Because sink particles have not been implemented into this code, and because it cannot follow very large gradients in the variables, we limit our study to the prestellar stage of the evolution of the dense core collapse. However, this is sufficient for investigating the development of the initial conditions for star formation.

We consider an isothermal gas with a mean density of $\langle n\rangle = 10^4\,\mathrm{cm}^{-3}$, a mean particle weight of 2.36, and a kinetic temperature of $T = 11.4\,\mathrm{K}$, implying an isothermal sound speed $c_s = 0.2\,\mathrm{km\,s}^{-1}$ in a numerical box with periodic boundaries. The gas is initially at rest and no gravity-counteracting forces such as a magnetic field or small-scale turbulence are included, so the gas is strongly Jeans-unstable. We choose the box side as $L_{\rm box} = \sqrt{10}\,L_{\rm J} \approx 3.16\,L_{\rm J} \approx 0.71$ pc, where $L_{\rm J} \approx 0.22\,\mathrm{pc}$ is the Jeans length. The box mass is $M_{\rm box} \approx 206\,M_\odot$.

The initial density field consists of a uniform background with $n \approx 10^4\,\mathrm{cm}^{-3}$, on top of which we have added a density fluctuation with a Gaussian profile, whose peak is at the box center and has a density $n \approx 1.5 \times 10^4\,\mathrm{cm}^{-3}$ (or ∼50% above the mean) and a FWHM ≈ 0.06 pc. Because the fluctuation is small in size ($r_{\rm core} \sim 0.14\,\mathrm{pc}$) and mass ($m_{\rm core} \approx 7.35\,M_\odot$), the background density is almost the same as the mean density, which is exactly $10^4\,\mathrm{cm}^{-3}$. The free-fall time for the background density is $t_{\rm ff} = \sqrt{3\pi/32G\rho} \approx 0.34$ Myr. The evolution proceeds on a timescale longer than $t_{\rm ff}$ because the initial gradient of the gravitational potential is very mild and of the periodic boundary conditions. Our initial setup is within "band 0" of WS85, which corresponds to clouds that are initially centrally peaked, far from hydrostatic equilibrium and collapsing immediately (the LP solutions also fall within this band, as noted by WS85).

We have also tested different sets of parameters for the background density and the central density fluctuation, but the behavior of these collapsing structures is qualitatively the same, and thus we focus only on the simulation described above. The only exception occurs in the cases when the central peak contains less than the local Jeans mass. In these cases, the density peak first expands and then collapses once enough mass has been accreted at the center.

We have chosen this setup inspired by our observation of how fragmentation proceeds in numerical simulations of cloud formation and evolution (e.g., Vázquez-Semadeni et al. 2007, 2009, 2010; Heitsch & Hartmann 2008; Banerjee et al. 2009; Colín et al. 2013; Gómez & Vázquez-Semadeni 2014). It has been argued in these papers that a forming GMC (and its atomic precursor) may rapidly acquire a large number of Jeans masses if the converging flow that assembles it is coherent and extended over a large region, as may be expected, for example, in a spiral arm, or in the collect-and-collapse scenario at the border of expanding shells (Elmegreen & Lada 1977). In this case, Hoyle (1953)-type fragmentation may be expected, where successively smaller scales may go unstable as the mean cloud density increases and the average Jeans mass decreases due to the global collapse in a nearly isothermal medium. The small-scale density fluctuations located far from the trough of the large-scale potential well may start growing locally while simultaneously being transported by the large-scale flow toward the remote collapse center, in a "conveyor belt" mode (see, e.g., Gómez & Vázquez-Semadeni 2014; Longmore et al. 2014, p. 291). As a first approximation, this type of flow can be represented locally as a static unstable background with a small clump collapsing within it, because the large-scale flow toward the distant global collapse center locally appears as a uniform bulk background motion, which is dynamically irrelevant to the local collapse.

3. RESULTS

In Figure 1, we show various snapshots from the evolution of the radial profiles of the density (*left panel*) and the velocity (*right panel*) of the core and its environment, both with a linear radial axis, to emphasize the external structure of the core and its envelope. It can be seen from this figure that, by embedding the core in a uniform background medium that is also collapsing, the nature of the collapse deviates from the self-similar asymptotic structure of the prestellar (or pre-singularity) stages of the collapse, such as the LP solutions. The core has a natural, well-defined "boundary," namely the place where it merges into the background. This boundary increases in radius during the evolution, but the material outside the boundary remains at the background density, and simply develops an inflow velocity that is continuous across the boundary, steadily accreting onto the core. On the other hand, in agreement with previous studies (Larson 1969; Penston 1969; Foster & Chevalier 1993; Mohammadpour & Stahler 2013), it can also be seen from Figure 1 that the flow remains subsonic during most of the prestellar evolution, although it eventually becomes supersonic at a so-called *sonic point*. Subsequently, the sonic point splits into two such points, to which we refer to as the inner and outer sonic points. The inner sonic point approaches the core center as time progresses, and finally reaches it at the time of singularity formation.

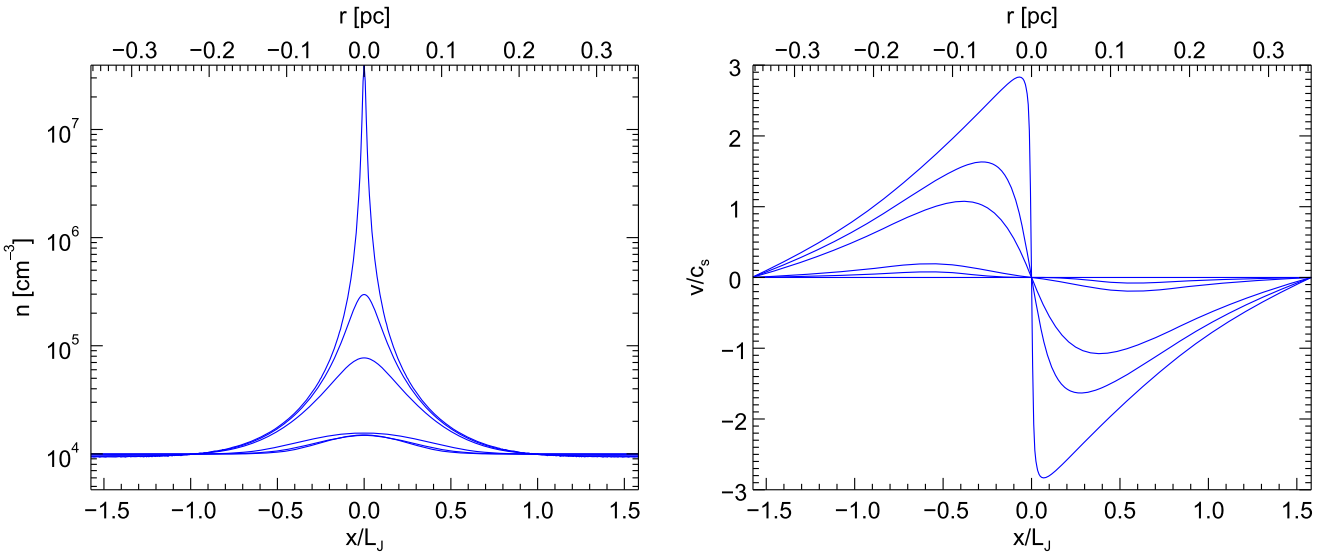

Figure 1. Evolution of the density (top panel) and velocity (bottom panel) profiles of the simulated core (See the text). The various lines in both panels represent the timesteps listed in Table 1.

In Figure 2, we again show the density and velocity profiles at six selected snapshots, together with the average column density and the ratio of the mass to the mean Jeans mass inside each radial position, $\mu \equiv M(r)/\langle M_J(r)\rangle$. In this figure, we use a logarithmic radial axis to emphasize the internal structure of the core. The selected snapshots are: $t = 0$ (panel a of Figure 2), showing the initial conditions; $t = 0.46\,t_{\rm ff}$ (panel b), where $t_{\rm ff}$ is the free-fall time of the background density. At this time, the gas has developed some moderate velocity in its external parts, near the *Jeans point* (the radius at which the mass ratio μ equals unity); $t = 0.92\,t_{\rm ff}$ (panel c), in which we begin to see a radially linear subsonic velocity profile and a uniform density profile within the region delimited by the Jeans point; $t = 1.84\,t_{\rm ff}$ (panel d), at which the flow develops a sonic point ($v = c_s$) at $r \approx 0.19$ $L_J \approx 0.05$ pc, located very close to the Jeans point ($\mu = 1$) at $r \approx 0.23$ pc; $t = 2.01\,t_{\rm ff}$ (panel e), at which the transonic point has already split into two points, bounding a region of almost uniform supersonic inward velocity (Mach number $\mathcal{M} \sim 1.40$); finally, $t = 2.14\,t_{\rm ff}$ (panel f), at which the core has an almost uniform supersonic velocity profile everywhere, with Mach number $\mathcal{M} \sim 1.95$, while the density adopts a power-law profile, with a slope approaching r^{-2}. On the last panel, we have overploted an SIS density profile (solid black line) for comparison to the actual profile of our core, which is clearly more extended than an SIS, although with a slope in its envelope that approaches the r^{-2} slope of the SIS. Table 1 lists various physical properties of the core at the same six selected snapshots as in Figure 2.

4. DISCUSSION AND IMPLICATIONS

4.1. Comparison with Observations: $M_{\rm core}/M_{\rm BE}$ versus $M_{\rm core}$ Diagram

Lada et al. (2008, hereafter L08) studied the stability of the dense core population in the Pipe Nebula region. They defined the cores using an extinction threshold of $A_V = 1.2$ mag, and derived median values of the density and mass of $n_{H_2} = 7.1 \times 10^3\,{\rm cm}^{-3}$, $M_{\rm core} \sim 0.2$–$20\,M_\odot$, respectively, and argued that most of the cores are gravitationally unbound and thermal-pressure-confined, with the external pressure provided by the weight of the surrounding MC. They modeled the cores as BE-spheres, assuming a temperature of 10 K, in order to determine their stability, finding that the entire population is characterized by a single critical BE-mass ($M_{\rm BE} = 1.82\big(\langle n\rangle/10^4\,{\rm cm}^{-3}\big)^{-0.5}(T/10\,{\rm K})^{1.5}\,M_\odot$) of $\sim 2\,M_\odot$. Most relevant to our interest here is that they plotted the ratio of the cores' mass to their BE-mass ($M_{\rm core}/M_{\rm BE}$) versus the cores' mass (see their Figure 9), finding that the observed core sample occupies a well-defined locus in this diagram.

Subsequently, Rathborne et al. (2009, hereafter R09) obtained a more robust determination of the physical properties of the Pipe cores by combining extinction and molecular-line data. They found mean radii $\langle R\rangle \sim 0.09$ pc, densities $n_{H_2} \sim 7.3 \times 10^3\,{\rm cm}^{-3}$, non-thermal velocity dispersions $\sigma_{\rm nt} \sim 0.18\,{\rm km\,s}^{-1}$, and masses $0.2\,M_\odot \leqslant M_{\rm core} \leqslant 19.4\,M_\odot$, so in what follows we use the R09 sample for our discussion. In addition, Ikeda et al. (2007, hereafter I07) have carried out a core survey in the Orion A MC. They derived core masses in the range of 2–80 $M_\odot$, with a mean mass of $12 \pm 12\,M_\odot$, a mean density $n \sim 2 \times 10^4\,{\rm cm}^{-2}$, consistent with the critical density of the $H^{13}CO^+(1$–$0)$ transition, and mean velocity dispersions of $0.52 \pm 0.17\,{\rm km\,s}^{-1}$. This corresponds to a more massive and supersonic core sample than the Pipe sample, and thus offers an interesting complementary set.

In order to compare our simulated core to the observational data, we must precisely define its boundaries. This is one of the most challenging tasks when investigating cores, because the boundaries often depend on circumstantial factors such as the tracer used, the signal-to-noise ratio, the background level, etc. In practice, the core's boundary is often defined by finding gradient breaks in the column density profiles (e.g., André et al. 2014, p. 27)—for example, the radial position of the point where the core appears to merge with the background, where the profile changes from a power law (the envelope) to a uniform-density (the background). Our setup, embedding the core in a uniform background, naturally lends itself to this definition. Thus, we operationally define the core's boundary as the radius at which the density is a certain (small) multiple of the background density. Specifically, we consider density

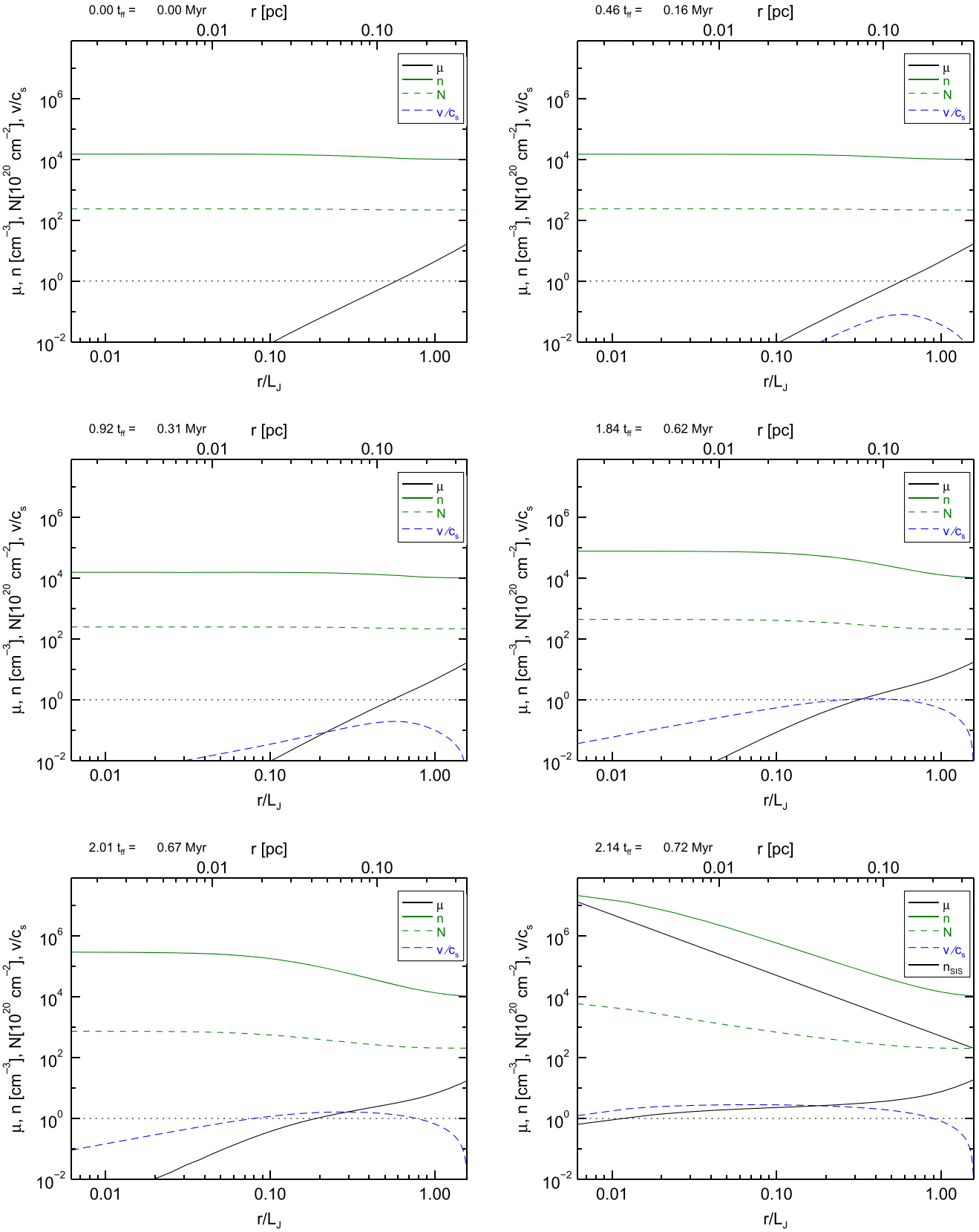

Figure 2. μ ratio, density, column density, and velocity profiles of the collapsing core (see the text for a description). The panels correspond to snapshots 0, 14, 28, 56, 61, and 65, out of a total of 66 snapshots. The solid black line in the last panel represents an SIS density profile given by $(c_s/2\pi Gr^2)(1/\mu_w m_H)$, where μ_w is the mean particle weight and m_H is the mass of hydrogen.

Table 1
Physical Properties of the Simulated Core

Time		n_{core}/n_{cloud}	N_{core}/N_{cloud}	v_{max}/c_s	$r_{\mu=1}$	$M_{\mu=1}$	$v/c_{s,\mu=1}$
(t_{ff})	(Myr)				(pc)	($M_\odot$)	
0.00	0.00	1.50	1.09	0.00	0.133	6.39	0.00
0.46	0.16	1.49	1.10	0.08	0.130	6.18	0.08
0.92	0.31	1.57	1.14	0.19	0.124	5.98	0.19
1.84	0.62	8.05	2.10	1.07	0.072	3.47	1.06
2.01	0.67	31.43	3.61	1.63	0.043	2.09	1.56
2.14	0.72	4224.50	36.10	2.83	0.003	0.19	2.07

Note. The rows correspond to same snapshots as in Figure 2.

Table 2
Physical Properties of the Simulated Core at the Different Background Density Thresholds

Time		$1.125n_{bg}$				$1.250n_{bg}$				$1.50n_{bg}$			
		R	M	M_{BE}	$\langle n\rangle$	R	M	M_{BE}	$\langle n\rangle$	R	M	M_{BE}	$\langle n\rangle$
(t_{ff})	(Myr)	(pc)	($M_\odot$)	($M_\odot$)	(10^4 cm^{-3})	(pc)	($M_\odot$)	($M_\odot$)	(10^4 cm^{-3})	(pc)	($M_\odot$)	($M_\odot$)	(10^4 cm^{-3})
0.00	0.00	0.74	1.73	1.99	1.23	0.52	0.66	1.92	1.33	…	…	…	…
0.69	0.73	…	…	…	…	…	…	…	…	0.05	5.74×10^{-4}	1.81	1.49
2.14	2.27	1.93	35.44	1.77	1.57	1.57	25.26	1.58	1.97	1.27	17.99	1.36	2.64

Note. Only the initial and final derived values are shown. The snapshots corresponds to the same snapshots as in Figure 2.

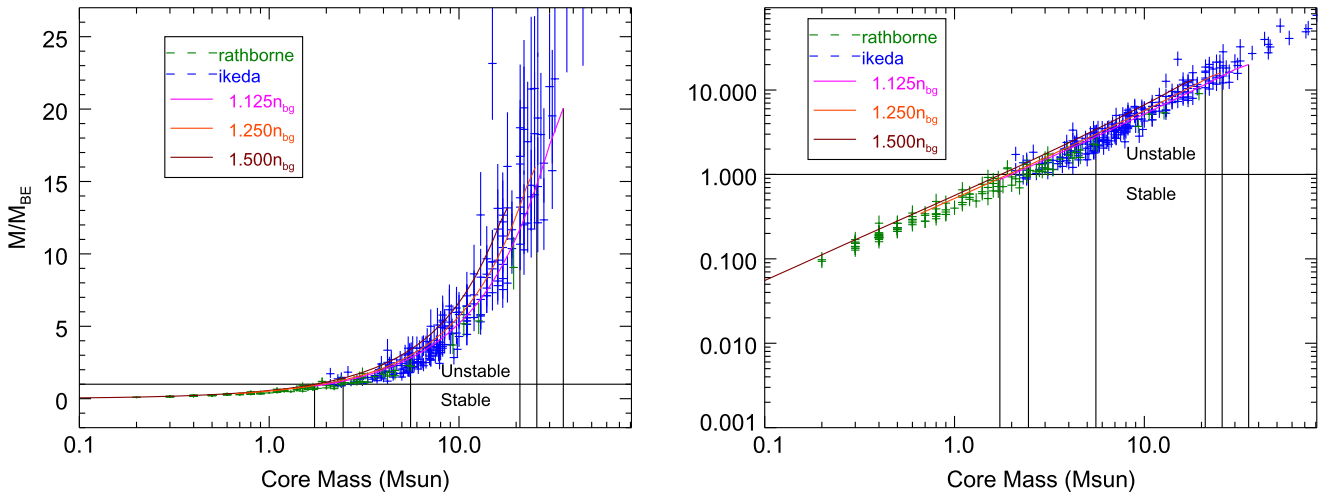

Figure 3. Ratio of core mass to BE critical mass for the cores in Table 2 from Rathborne et al. (2009; green), Table 1 from Ikeda et al. (2007; blue) and our simulated core at different background density thresholds (continuous curves; see the text). Each point has a vertical error bar that spans the values of the BE-mass at temperatures of 10 and 13 K (from top to bottom). The vertical lines denote the times shown in Figure 2.

thresholds of 1.125, 1.25, and 1.5 times the background density as the boundary of the core.

Figure 3 shows the ratio M_{core}/M_{BE} versus M_{core} for the aforementioned observations and for our simulated core throughout its evolution, as defined by the three density thresholds (see also Table 2). The times corresponding to the selected snapshots shown in Figure 2 are indicated by vertical lines. For our core, we compute the BE-mass using the nominal temperature of 11.4 K. For the observational core sample, no explicit temperature information is provided by the authors. R09 assume a gas temperature of 10 K in all cases, while I07 mention that the typical temperature in Orion is 20 K, but make no explicit mention that this may be the actual temperature in the dense cores. In fact, it is quite likely that the temperature there is lower, because of the higher densities. Thus, we have calculated the BE-mass for all the observed cores assuming $T \approx 11.5$ K, and assigning error bars whose extremes correspond to $T = 10$ and 13 K.

From Figure 3 we note that the Orion cores from the I07 sample essentially ocuppy the same locus as the Pipe cores from the R09 sample in this diagram, although extending toward higher masses and/or higher values of the mass ratio. Also, we note that the evolutionary track of our core, as defined by the threshold at 1.125 times the background density, tracks almost exactly the locus of the observed cores. These results strongly suggest that *the sequences of observed (both low- and high-mass) cores are all part of a self-similar collapse process, only at different evolutionary stages and total masses, including the apparently stable ones*. The latter only appear as stable because they are in an early stage of development,

with only a small density contrast over ther background, but they are nevertheless growing, as their entire background is gravitationally unstable.

4.2. Comparison With Earlier Numerical and Analytical Collapse Studies

In agreement with previous studies (e.g., Larson 1969; Whitworth & Summers 1985; Vorobyov & Basu 2005; Gómez et al. 2007, MS13), the density profile of the simulated prestellar core resembles a BE-sphere at all times, being flat at the center, and developing a power-law at the external parts, to which we refer to as "the envelope." As the collapse proceeds, the central part increases in density while decreasing in radius. A supersonic region then emerges, bounded by two transonic points that become increasingly distant from each other, one moving inwards and the other outwards, as time progresses. At the latest stages, just before the formation of the protostar, the density profile assumes a SIS-like shape, but truncated at the radius at which the core merges with the background.

These results can be put in the context of early analytical studies on spherical gravitational collapse that have commonly used similarity techniques (Larson 1969; Shu 1977; Whitworth & Summers 1985). As is well known, S77 considered the collapse of a hydrostatic SIS, finding, among others, the classical "inside-out" solution, characterized by a collapsing inner region bounded by an expanding rarefaction wavefront, beyond which the gas is static. Inside the transition front, the core is characterized by density and infall velocity profiles that scale as $r^{-3/2}$ and r^{-2}, respectively. However, a slightly less well known fact is that S77 discussed, more generally, the large-radius (or early-time) asymptotic behavior of those solutions for which the velocity is not initially zero everywhere, but instead only approaches zero in this limit. These solutions are characterized by an initial density profile of the form

$$\rho(r) = \frac{c_s^2 A}{4\pi G} r^{-2}, \tag{1}$$

and initial velocity profile given by

$$u(r) = -c_s^2 (A - 2)\frac{t}{r}, \tag{2}$$

where the minus sign indicates that the velocity is directed inwards, c_s is the isothermal sound speed, and A is a constant that determines whether the velocity is initially zero and remains at that value ($A = 2$), or instead starts with a finite value and further increases with time ($A > 2$). The former static solution corresponds to a hydrostatic SIS, while the latter dynamic solution corresponds to an SIS-like structure (i.e., with an r^{-2} density profile) but with a larger mass and with an initial inward velocity, so that it is gravitationally unstable and collapses after $t = 0$. In this case, the outer parts of the core are never at rest. It is important to recall that S77 also calculated the accretion rate onto the protostar after the formation of the singularity[1] (the protostar itself) as

$$\dot{M} = \frac{m_0 c_s^3}{G}, \tag{3}$$

where m_0 is a constant related to A. The "canonical" value, $m_0 = 0.975$, corresponds to $A \to 2^+$, i.e., to a hydrostatic initial condition. In addition, S77 argued that the earlier similarity solution found by LP was unrealistic because its asymptotic large-radius (or small-time before singularity formation) limit consists of a uniform inward velocity of $-3.3c_s$ and a density that is 4.4 times that of the SIS at each radius, which he deemed "unlikely to occur in a natural way." However, subsequent analytical and numerical studies (Hunter 1977; Whitworth & Summers 1985; Foster & Chevalier 1993) that considered a larger region in parameter space, showed the existence of a continuum of solutions and, in particular, the numerical simulations of FC93 showed that the LP solution is approached only over a finite radial extent, ameliorating S77's objection to it.

Moreover, S77's inside-out solution has been criticized by some authors (e.g., Whitworth et al. 1996; Vázquez-Semadeni et al. 2005) because its initial condition, the hydrostatic SIS, is an *unstable* equilibrium, onto which it is impossible for the core to settle within the context of a turbulent, dynamic medium such as a MC. It has also been reported that observations of MC cores exhibit extended infall radial motions that are inconsistent with the inside-out solution of S77 (e.g., Tafalla et al. 1998; Lee et al. 2001).

Most early numerical simulations considered the case of bounded, marginally gravitationally unstable initial conditions, neglecting the possibility of accretion onto the core during the prestellar phase (prior to the formation of the central singularity). More recently, accretion has been addressed by various groups (Vorobyov & Basu 2005; Gómez et al. 2007; Gong & Ostriker 2009, MS13). Gómez et al. (2007) and Gong & Ostriker (2009) considered the formation and collapse or re-expansion of a core formed by a spherically symmetric compression. They found that cores formed in this way are bounded by an accretion shock, inside of which the core evolves along a sequence of BE-configurations, but with a mass that increases over time due to the accretion until the configuration becomes unstable and collapses, or else rebounds, if the accretion is insufficient to render it Jeans-unstable. On the other hand, MS13 considered a constant accretion flow onto the core, imposed as a boundary condition. Although their simulations behaved very similarly to ours, the accretion they used was imposed rather than self-consistent, and forced to be subsonic at all times.

Very recently, Keto et al. (2015) have investigated the collapse process of various types of structures. Among other cases, they considered the collapse of an SIS, of an unstable-equilibrium (UE) BE-sphere[2], and of a non-equilibrium (NE) pseudo-BE-sphere.[3] They found that the latter two configurations retained a BE-like density profile, but that their velocity

[1] In the earlier literature, the moment at which the singularity forms is referred to as "core formation." Here we avoid this nomenclature in order to avoid confusion with the dense core of the MC.

[2] I.e., a solution of the Lane–Emden equation, truncated out to a radius large enough that the ratio of central to peripheral density is larger than that of a critical BE-sphere, and slightly perturbed so that it proceeds to collapse.

[3] This is not a true BE-sphere as it is not a solution of the Lane–Emden equation. Instead, it is constructed by obtaining one such solution and then increasing the density everywhere by 10%, so that the configuration is nowhere in equilibrium anymore.

profiles differed significantly, with the NE sphere developing large velocities out to its truncation radius, while the UE one retained a nearly zero velocity at its edge. However, accretion was not included in their simulations.

Our simulation, instead, includes the novel feature of enveloping the collapsing core in a globally gravitationally unstable, *uniform* background, to mimic the physical conditions of cores in globally, hierarchically collapsing clouds, and the fact that cores are often observed to exist over a roughly uniform background (e.g., di Francesco et al. 2007, p. 17; André et al. 2014, p. 27, and references therein). This situation falls within the "band 0" class of solutions investigated by WS85, and essentially exhibits the behavior envisaged by those authors: the pre-singularity (prestellar) collapse proceeds in an outside-in fashion (i.e., at early times the maximum infall speed occurs at the edge of the core; see also Gong & Ostriker 2011) and consists of two main regions: an inner region, characterized by a roughly flat density profile with an infall velocity that increases linearly with radius, and an outer region, characterized by an r^{-2} density profile with a uniform infall velocity. However, in our simulation, this uniform-infall-speed region is finite and bound by the outer transonic point, beyond which the infall speed rapidly drops to zero again.[4] These results are easy to understand intuitively. Since the collapse is local, far from its center we should not expect any motions directed toward it. Nevertheless, the outer transonic point moves outwards, implying that the collapse spreads out to larger regions. This is qualitatively similar to S77's expanding rarefaction wave although, in our case, the transition from collapsing to static occurs smoothly, rather than through an abrupt wavefront. Finally, inside the inner transonic point, the flow exhibits an infall velocity that is linear with radius, implying that *the velocity smoothly approaches zero toward the center during the entire prestellar evolution of the core.* (See further discussion of the implications of this property in Section 4.3.)

Consequently, during its prestellar stage, our simulation evolves through a sequence of BE-spheres of increasing central-to-external density ratios, so that it appears like a *stable* BE-sphere at early times and like an *unstable* one at later times. The inner transonic point migrates inwards and reaches the center at the time of singularity formation. At this time, the entire core is characterized by a density configuration that resembles a SIS, except that in our case this state is *not* hydrostatic, but rather quite dynamic, with a uniform infall velocity of $\sim 3\, c_s$, thus corresponding to S77's initial condition with $A > 2$.

Our setup differs from studies that start with *hydrostatic* BE or BE-like spheres (e.g., Foster & Chevalier 1993; Vorobyov & Basu 2005; Keto et al. 2015). Instead, our simulation lets the density and velocity profiles develop self-consistently, rather than imposing them as initial conditions. Although it also starts with hydrostatic conditions, these correspond to an early enough stage that, by the time the core has developed a pseudo-BE density profile, it is already collapsing everywhere, rather than being hydrostatic. This can occur, in spite of the very moderate amplitude of the initial density fluctuation, because the whole background is unstable, so *the fluctuation does not need to exceed the critical central-to-peripheral density ratio in order to begin collapsing*. This is a reasonable situation since, after all, the core must be *assembled* by moving material from the surroundings into it, and this requires a non-zero, convergent velocity field.

In order to produce a developed hydrostatic BE-sphere, as in the standard practice of starting with hydrostatic BE-like structures, the velocity field that assembled the core would have to first decay to zero, and then resume again to continue collapsing. This appears as a highly contrived process. Keto et al. (2015) have suggested that one process that may temporarily halt the contracting motions is the turbulent pressure, which must then dissipate to allow the collapse to resume. However, this implicitly assumes that the non-thermal motions actually have a sufficiently random nature, and have sufficiently small characteristic size scales, that they can produce an effective pressure which provides support against gravity. This notion that has been challenged recently (Vázquez-Semadeni et al. 2008; Ballesteros-Paredes et al. 2011; González-Samaniego et al. 2014).

Conversely, in the hierarchical gravitational collapse scenario, the possibility of turbulent support is discarded from the outset, and the motions are assumed to be dominated by an inward component driven by gravity. Within this scenario, the fragmentation occurs as forseen by Hoyle (1953), so that, as a cloud contracts and becomes denser, the average Jeans mass becomes smaller, and so progressively smaller density fluctuations can collapse. However, because the cloud is turbulent, the fluctuations are nonlinear, and thus have shorter free-fall times than the cloud at large, implying that they terminate their collapse earlier, as observed in numerical simulations of cloud formation and evolution by converging flows (e.g., Vázquez-Semadeni et al. 2007, 2009; Heitsch & Hartmann 2008; Heitsch et al. 2009; Gómez & Vázquez-Semadeni 2014). In this scenario, the clumps and cores produced by the turbulence only act as seeds for local gravitational collapse, and are never supported by non-thermal motions, but instead simply grow gravitationally from the outset, as represented in the simulation presented here. As shown in Section 4.1, this setup naturally explains a fundamental property of observed dense cores: their location in the $M_{\rm core}/M_{\rm BE}$ versus $M_{\rm core}$ diagram.

4.3. Implications for the Interpretation of Observed Core Structure

In Section 3 we found that the core evolves along a sequence of BE-like density profiles, but with a global infall velocity, so that this profile is not indicative of a hydrostatic configuration, not even during the apparently stable stages (when the central-to-boundary density ratio is smaller than the critical value for instability). This result provides a clear interpretation to the ubiquity of BE-like profiles observed in prestellar cores without introducing the conundrum that a core needs to grow in spite of being hydrostatic. The resolution of this dilemma lies in the fact that, although the density profile is BE-*like*, it is not a true BE-sphere in the sense that it does not result as a solution of the hydrostatic Lane–Emden equation, but rather as a dynamic solution of the time-dependent hydrodynamic equations, which is characterized by inwards motion at all times.

Moreover, in Section 4.1 we have shown that our simulated core, with its boundary defined as the position where the density becomes equal to the background, traces the locus of the aforementioned core surveys in the $M_{\rm core}/M_{\rm BE}$ versus

[4] In our simulation, the infall motion cannot reach the boundary of the box because of the periodic boundary conditions, but the boundaries are far enough from the collapsing core that we do not expect them to significantly affect its evolution during the time interval we explore.

$M_{\rm core}$ diagram. This result suggests the possibility that those core ensembles actually represent random samplings of cores at all possible evolutionary stages, so that their locus in that diagram traces the evolutionary track of a single core. It also suggests the possibility that the range of core masses in a given low- or high-mass star-forming region is determined simply by the mass increase of the cores during their evolution, but that the initial fragmentation occurs at the same initial mass, which corresponds simply to the Jeans mass of the background medium. This is consistent with the result by L08 that their whole sample is well characterized by a *single* BE-mass. Indeed, since the prestellar stages of evolution lead to an approach to an r^{-2} density profile above the background, for which the mean density is only three times larger than the density at the boundary, then the BE mass, proportional to the inverse square root of the mean density (assuming isothermality), is at most within a factor $\sqrt{3}$ larger than that determined by the background. Thus, in the present scenario, the BE mass is essentially determined by the background density, rather than by the local core properties. This is also consistent with the recent finding by Palau et al. (2015) that the number of fragmentats in massive cores appears to be determined simply by the number of thermal Jeans masses contained in the core.

Also, we reported that the velocity field is smooth across the core boundary (compare both panels of Figure 1). This implies that, if one insists in describing the core as "pressure bounded," the confining pressure is *ram* pressure from the material accreting onto the core, rather than thermal pressure maintaing a hydrostatic configuration. But considering it as "pressure bounded" is misleading, because any Lagrangian (i.e., moving with the flow) spherical shell is moving inwards at any time due to gravity, and thus no bounding is needed. The correct physical description is that the core is the "tip of the iceberg" of the globally collapsing cloud.

The fact that the velocity profile in the inner part of the core is linear with radius during the prestellar evolution implies that the velocities are smaller closer to the center. This, in turn, implies that multi-tracer observations of the core would give smaller velocity dispersions at higher densities/smaller radii, giving the impression of a "transition to coherence" (e.g., Goodman et al. 1998). However, in our scenario, this is not due to dissipation of turbulence, but rather to the fact that the infall velocities are smaller in the inner part of the core. Finally, the property that the largest velocities occur in the outer parts of the core where the density begins to drop, implies that the line profiles may be narrower than would correspond to those largest velocities. We dicuss this at more length in Section 4.4.

4.4. Are the Supersonic Velocities Really a Problem?

Our simulation, like most other simulations of Larson–Penston-like flow, develops supersonic velocities in the final stages of evolution, which however correspond to the stages most likely to be observed, as the core is most prominent at those times. Such large velocities are generally not observed in low-mass cores (see, e.g., the review by Bergin & Tafalla 2007). MS13 noted this problem, and concluded that their simulation (quite similar to ours) is not the correct model for the collapse of actual cores, and that magnetic tension may be necessary to render the collapse less dynamic. MS13 also pointed out that the supersonic infall produces accretion rates that are too high, leading to the so-called "luminosity problem" (Kenyon et al. 1990). Our simulation, being spherically symmetric, suffers from the same problems. However, it is possible that the resolution of these issues does not lie in invoking the magnetic field to provide support, but rather in geometrical and/or observational-bias factors.

Concerning geometry, our simulation, like all other non-magnetic, isothermal, spherically symmetric ones, represents the most dynamic possible scenario for collapse. Indeed, recent studies (Pon et al. 2012; Toalá et al. 2012) have shown that flattened or filamentary structures collapse on longer timescales than spherical structures of the same volume density. Thus, considering the non-spherical nature of the cores may contribute toward alleviating the problem. Moreover, the luminosity problem may be resolved if the accretion does not proceed directly onto the protostar, but rather it is mediated by a circumstellar disk (Kenyon & Hartmann 1995; Whitworth & Ward-Thompson 2001; Dunham & Vorobyov 2012), which is also a non-spherical structure. The resolution of this issue must await analysis of cores arising self-consistently in fully 3D numerical simulations of MC evolution (e.g., Smith et al. 2013).

Concerning possible observational biases, we note that observational determinations of infall velocities depend on the underlying assumptions for the topology of the velocity field in the clump. Because a line profile is essentially a density-weighted radial velocity histogram along the line of sight (with possible self-absorption features), the fact that in our simulation the largest velocities occur in the core's envelope rather than at the center may cause these large velocities to appear at the line wings rather than at the central parts of the line, thus giving the appearance that the infall speeds are smaller than they actually are. We plan to address this possibility in a future contribution (R.M. Loughnane et al. 2015, in preparation).

5. SUMMARY AND CONCLUSIONS

We have presented a highly idealized simulation of the prestellar stages of the gravitational collapse of an isothermal spherical core within the scenario of hierarchical gravitational collapse. To accomplish this, we have embedded the core in a uniform-density background that is, itself, gravitationally unstable. The evolution of the core was followed since its earliest stages, starting with a minor density fluctuation of amplitude 1.5 times the background density, containing a mass slightly larger than the Jeans mass of the background density, and with a generic Gaussian profile. We have found the following results.

1. The core evolves according to the "Band 0" solution of WS85, which refers to objects that start out far from equilibrium, and includes the LP solutions.
2. In agreement with previous studies, and with the regularly observed structure of prestellar cores, the simulated core develops a BE-like profile, with a nearly uniform-density (or "flat") central region, and a nearly power-law envelope, but it is *always* in the process of collapsing—even during the early stages, when the central to background density contrast is smaller than that of a critical BE sphere ($\rho_{\rm c}/\rho_{\rm b} \sim 14$), and the core would be labeled as "stable." This result removes the apparent inconsistency between the apparently hydrostatic density structure of the cores (i.e., of stable BE-spheres) and the need for them to grow in order to eventually form stars. It also suggests that a smaller

fraction of cores are "starless" (in the sense that they will never form stars) than usually thought. Instead, it is possible that these are just in their very earliest stages of growth.

3. The collapse proceeds in an "outside-in" fashion, developing the largest (and nearly radially constant) speeds in the power-law density envelope, and a linear-with-radius velocity profile in the central flat region. This implies that the velocities in the centermost parts of the core are small and subsonic during the whole prestellar evolution. This is contrary to the famous inside-out solution of Shu (1977), which is *not* expected because its initial condition, a *hydrostatic* SIS, is an unstable equilibrium, and therefore unrealizable from a dynamical previous evolution.
4. The boundary of the core, defined as the position where it merges with the background, increases in radius as time progresses, so that the core thus defined effectively grows in mass and size. The velocity field is smooth across this boundary, so that the material outside the boundary accretes onto the core smoothly, although it does not increase its density until it crosses the boundary.
5. The largest velocities in the system—those appearing in the power-law envelope—are supersonic by the time the core has grown enough to be clearly detectable (with at least a tenfold enhancement over the background). However, the fact that the largest velocities are located at the envelope implies that they will receive a lower density weighting for the production of a line profile, so that infall profiles may underestimate the velocities. In a future study we will investigate the nature of the lines produced by our core (R.M. Loughnane et al. 2015, in preparation).
6. The ratio of the core's mass ($M_{\rm core}$) to the critical BE-mass ($M_{\rm BE}$) increases as the core's mass increases, and traces the locus of observed cores in the $M_{\rm core}/M_{\rm BE}$ versus $M_{\rm core}$ diagram, evolving from apparently stable to apparently unstable configurations, although the core is unstable at all times. Thus, the locus of observed cores in this diagram can be interpreted as a random sample of evolving collapsing cores within globally unstable clouds. This result suggests that the sequences of observed (both low- and high-mass) cores are all part of a self-similar collapse process, only at different evolutionary stages and total masses, including the apparently stable ones.

We conclude that the evolution of marginally unstable cores embedded in a strongly unstable environment, as prescribed by the hierarchical gravitational collapse scenario, is not only consistent with the observed density structure of MC cores and their location in the $M_{\rm core}/M_{\rm BE}$ versus $M_{\rm core}$ diagram, but provides a natural explanation to the problem of how a core may grow in mass while appearing gravitationally stable. Another conclusion is that the choice of initial conditions is crucial for the subsequent evolution of the system, and thus care must be exercised in choosing the most realistic initial conditions within the realm of the physical problem at hand.

Some problems remain, of course, regarding the appearance of supersonic speeds during the prestellar evolution, which are generally not observed in low-mass cores, as pointed out by MS13. In future contributions, we plan to investigate whether this apparent discrepancy can be resolved in terms of a non-spherical collapse geometry and/or the effects of the outside-in velocity field on the formation of infall line profiles.

We thankfully acknowledge an anoymous referee, whose insightful and sharp recommendations helped improve the clarity and coherence of the paper. The numerical simulations were performed in the cluster acquired with CONACYT grant 102488 to E.V.-S. Also, R.M.L. was supported with funds from this grant.

REFERENCES

Alves, J. F., Lada, C. J., & Lada, E. A. 2001, Natur, 409, 159
André, P., Di Francesco, J., Ward-Thompson, D., et al. 2014, in Protostars and Planets VI, ed. H. Beuther et al. (Tucson, AZ: Univ. Arizona Press), 27
André, P., Men'shchikov, A., Bontemps, S., et al. 2010, A&A, 518, L102
Arzoumanian, D., André, P., Didelon, P., et al. 2011, A&A, 529, L6
Audit, E., & Hennebelle, P. 2005, A&A, 433, 1
Ballesteros-Paredes, J., Hartmann, L., & Vázquez-Semadeni, E. 1999, ApJ, 527, 285
Ballesteros-Paredes, J., Hartmann, L. W., Vázquez-Semadeni, E., Heitsch, F., & Zamora-Avilés, M. A. 2011, MNRAS, 411, 65
Ballesteros-Paredes, J., Klessen, R. S., & Vázquez-Semadeni, E. 2003, ApJ, 592, 188
Banerjee, R., Vázquez-Semadeni, E., Hennebelle, P., & Klessen, R. S. 2009, MNRAS, 398, 1082
Bergin, E. A., & Tafalla, M. 2007, ARA&A, 45, 339
Bertoldi, F., & McKee, C. F. 1992, ApJ, 395, 140
Bonnor, W. B. 1956, MNRAS, 116, 351
Burkert, A., & Hartmann, L. 2004, ApJ, 616, 288
Colín, P., Vázquez-Semadeni, E., & Gómez, G. C. 2013, MNRAS, 435, 1701
di Francesco, J., Evans, N. J., II, Caselli, P., et al. 2007, in Protostars and Planets V, ed. B. Reipurth, D. Jewitt, & K. Keil (Tucson, AZ: Univ. Arizona Press), 17
Dunham, M. M., & Vorobyov, E. I. 2012, ApJ, 747, 52
Ebert, R. 1955, ZAp, 36, 222
Ebert, R. 1957, ZAp, 42, 263
Elmegreen, B. G., & Lada, C. J. 1977, ApJ, 214, 725
Foster, J. B., Rosolowsky, E. W., Kauffmann, J., et al. 2009, ApJ, 696, 298
Foster, P. N., & Chevalier, R. A. 1993, ApJ, 416, 303
Galván-Madrid, R., Keto, E., Zhang, Q., et al. 2009, ApJ, 706, 1036
Gómez, G. C., & Vázquez-Semadeni, E. 2014, ApJ, 791, 124
Gómez, G. C., Vázquez-Semadeni, E., Shadmehri, M., & Ballesteros-Paredes, J. 2007, ApJ, 669, 1042
Gong, H., & Ostriker, E. C. 2009, ApJ, 699, 230
Gong, H., & Ostriker, E. C. 2011, ApJ, 729, 120
González-Samaniego, A., Vázquez-Semadeni, E., González, R. F., & Kim, J. 2014, MNRAS, 440, 2357
Goodman, A. A., Barranco, J. A., Wilner, D. J., & Heyer, M. H. 1998, ApJ, 504, 223
Gutermuth, R. A., Bourke, T. L., Allen, L. E., et al. 2008, ApJL, 673, L151
Hartmann, L., & Burkert, A. 2007, ApJ, 654, 988
Heitsch, F., Ballesteros-Paredes, J., & Hartmann, L. 2009, ApJ, 704, 1735
Heitsch, F., Burkert, A., Hartmann, L. W., Slyz, A. D., & Devriendt, J. E. G. 2005, ApJL, 633, L113
Heitsch, F., & Hartmann, L. 2008, ApJ, 689, 290
Heitsch, F., Hartmann, L. W., Slyz, A. D., Devriendt, J. E. G., & Burkert, A. 2008, ApJ, 674, 316
Hennebelle, P., & Pérault, M. 1999, A&A, 351, 309
Heyer, M., Krawczyk, C., Duval, J., & Jackson, J. M. 2009, ApJ, 699, 1092
Hoyle, F. 1953, ApJ, 118, 513
Hunter, C. 1977, ApJ, 218, 834
Ikeda, N., Sunada, K., & Kitamura, Y. 2007, ApJ, 665, 1194
Kenyon, S. J., & Hartmann, L. 1995, ApJS, 101, 117
Kenyon, S. J., Hartmann, L. W., Strom, K. M., & Strom, S. E. 1990, AJ, 99, 869
Keto, E., & Caselli, P. 2010, MNRAS, 402, 1625
Keto, E., Caselli, P., & Rawlings, J. 2015, MNRAS, 446, 3731
Kirk, H., Myers, P. C., Bourke, T. L., et al. 2013, ApJ, 766, 115
Koyama, H., & Inutsuka, S.-I. 2000, ApJ, 532, 980
Koyama, H., & Inutsuka, S.-i. 2002, ApJL, 564, L97
Lada, C. J., Alves, J. F., & Lombardi, M. 2007, in Protostars and Planets V, ed. B. Reipurth, D. Jewitt, & K. Keil (Tucson, AZ: Univ. Arizona Press), 3

Lada, C. J., Muench, A. A., Rathborne, J., Alves, J. F., & Lombardi, M. 2008, ApJ, 672, 410
Larson, R. B. 1969, MNRAS, 145, 271
Larson, R. B. 1981, MNRAS, 194, 809
Lee, C. W., Myers, P. C., & Tafalla, M. 1999, ApJ, 526, 788
Lee, C. W., Myers, P. C., & Tafalla, M. 2001, ApJS, 136, 703
Leorat, J., Passot, T., & Pouquet, A. 1990, MNRAS, 243, 293
Longmore, S. N., Kruijssen, J. M. D., Bastian, N., et al. 2014, in Protostars and Planets VI, ed. H. Beuther, R. S. Klessen, C. P. Dullemond, & T. Henning (Tucson, AZ: Univ. Arizona Press), 291
Men'shchikov, A., André, P., Didelon, P., et al. 2010, A&A, 518, L103
Mohammadpour, M., & Stahler, S. W. 2013, MNRAS, 433, 3389
Molinari, S., Swinyard, B., Bally, J., et al. 2010, A&A, 518, L100
Myers, P. C. 2009, ApJ, 700, 1609
Myers, P. C., Dame, T. M., Thaddeus, P., et al. 1986, ApJ, 301, 398
Palau, A., Ballesteros-Paredes, J., Vazquez-Semadeni, E., et al. 2015, MNRAS, 453, 3785P
Penston, M. V. 1969, MNRAS, 144, 425
Peretto, N., Fuller, G. A., André, P., et al. 2014, A&A, 561, A83
Peretto, N., Fuller, G. A., Duarte-Cabral, A., et al. 2013, A&A, 555, A112
Pineda, J. E., Goodman, A. A., Arce, H. G., et al. 2010, ApJL, 712, L116
Polychroni, D., Schisano, E., Elia, D., et al. 2013, ApJL, 777, L33
Pon, A., Toalá, J. A., Johnstone, D., et al. 2012, ApJ, 756, 145
Rathborne, J. M., Lada, C. J., Muench, A. A., et al. 2009, ApJ, 699, 742
Schneider, N., Csengeri, T., Bontemps, S., et al. 2010, A&A, 520, A49
Shu, F. H. 1977, ApJ, 214, 488
Simpson, R. J., Johnstone, D., Nutter, D., Ward-Thompson, D., & Whitworth, A. P. 2011, MNRAS, 417, 216
Smith, R. J., Glover, S. C. O., & Klessen, R. S. 2014, MNRAS, 445, 2900
Smith, R. J., Shetty, R., Beuther, H., Klessen, R. S., & Bonnell, I. A. 2013, ApJ, 771, 24
Solomon, P. M., Rivolo, A. R., Barrett, J., & Yahil, A. 1987, ApJ, 319, 730
Tafalla, M., Mardones, D., Myers, P. C., et al. 1998, ApJ, 504, 900
Tafalla, M., Myers, P. C., Caselli, P., & Walmsley, C. M. 2004, A&A, 416, 191
Tafalla, M., Myers, P. C., Caselli, P., Walmsley, C. M., & Comito, C. 2002, ApJ, 569, 815
Toalá, J. A., Vázquez-Semadeni, E., & Gómez, G. C. 2012, ApJ, 744, 190
Vázquez-Semadeni, E., Banerjee, R., Gómez, G. C., et al. 2011, MNRAS, 414, 2511
Vázquez-Semadeni, E., Colín, P., Gómez, G. C., Ballesteros-Paredes, J., & Watson, A. W. 2010, ApJ, 715, 1302
Vázquez-Semadeni, E., Gómez, G. C., Jappsen, A. K., et al. 2007, ApJ, 657, 870
Vázquez-Semadeni, E., Gómez, G. C., Jappsen, A.-K., Ballesteros-Paredes, J., & Klessen, R. S. 2009, ApJ, 707, 1023
Vázquez-Semadeni, E., González, R. F., Ballesteros-Paredes, J., Gazol, A., & Kim, J. 2008, MNRAS, 390, 769
Vázquez-Semadeni, E., Kim, J., Shadmehri, M., & Ballesteros-Paredes, J. 2005, ApJ, 618, 344
Vázquez-Semadeni, E., Ryu, D., Passot, T., González, R. F., & Gazol, A. 2006, ApJ, 643, 245
Vorobyov, E. I., & Basu, S. 2005, MNRAS, 360, 675
Whitworth, A., & Summers, D. 1985, MNRAS, 214, 1
Whitworth, A. P., Bhattal, A. S., Francis, N., & Watkins, S. J. 1996, MNRAS, 283, 1061
Whitworth, A. P., & Ward-Thompson, D. 2001, ApJ, 547, 317
Wilson, R. W., Jefferts, K. B., & Penzias, A. A. 1970, ApJL, 161, L43

5.1 Implications of GHC for prestellar cores

The evolution of marginally unstable cores embedded in a strongly unstable environment, as prescribed by the GHC scenario, is consistent with the observed density structure of MC cores and their location in the $M_{\rm core}/M_{\rm BE}$ versus $M_{\rm core}$ diagram and naturally explains the mass growth of cores that appear gravitationally stable.

This approach solves the problem in the thermal pressure confinement scenario whereby stable cores should never collapse if they were not part of a large scale collapsing structure. In addition, our scenario predicts that the sequences of observed (both low- and high-mass) cores are all part of a self-similar collapse process, only at different evolutionary stages and total masses, including the apparently stable ones. The latter only appear as stable because they are in an early stage of development, with only a small density contrast over their background, but they are nevertheless growing, as their entire background is gravitationally unstable.

One remaining problem with our scenario is that, observationally, low-mass cores typically exhibit subsonic velocities only using infall tracers such as moderately optically thick molecular lines. Ours, instead, develop supersonic velocities close to the time of protostar formation. This apparent contradiction, however, may possibly be solved as follows. Line profiles are essentially density-weighted velocity histograms along the line of sight. Therefore, observational determinations of infall velocities from line profiles depend on the underlying assumption for the shape of the infall velocity profile. Consequently, Loughnane *et al. in prep*, have performed synthetic observations of the prestellar core model of (Naranjo-Romero et al., 2015) at $\sim 0.63\,$Myr. The derived infall speed from these observations is only $\sim 1/2$ of $c_{\rm s}$, *i.e.*, ~ 4 times lower than maximum actual speed. Thus, these diagnostics may systematically underestimate the infall speeds. Moreover, we must emphasize that the standard inside-out collapse model of Shu et al. (1987) is not likely to represent the actual dynamical state of prestellar cores (*e.g.*, Whitworth et al., 1996).

Our results highlight that the choice of initial conditions of numerical simulations of prestellar cores is crucial for the subsequent evolution of the system, and thus care must be exercised in choosing the most realistic initial conditions within the realm of the physical problem at hand. In particular, it is crucial to first examine the fundamental processes, instead of starting with extremely detailed physical ingredients that excessively increase the complexity of data analysis of density and velocity structures, and hamper the identification of the dominating processes.

Chapter 6

Prestellar filaments

In the previous chapter, we tested the implications of the scenario of GHC on the formation and evolution of prestellar cores immersed in an unstable parent molecular cloud constituting a simple two-level hierarchy with one element in each hierarchy. In this chapter, we will study a deeper hierarchy level including the intermediate step of filamentary structure. Additionally, we test the use a stratified density background for the filament as suggested by the sheet-like molecular clouds found in numerical simulations of MC formation (Heitsch et al., 2005; Vázquez-Semadeni et al., 2006; Folini and Walder, 2006; Audit and Hennebelle, 2010). We wish to extend our results and understand the observed structure of filaments and their dynamics, with the premise that filaments are a channel funneling material accreted from the molecular cloud down to prestellar cores. Our approach is quite different from previous work, because we assume that the filaments are not hydrostatic structures as previously thought, in agreement with self-consistent filament formation in numerical simulations of cloud formation by colliding flows (Gómez and Vázquez-Semadeni, 2014).

For theoretical context, Vázquez-Semadeni et al. (2009) numerically studied the effects of gravity on global and local scales in the formation of molecular clouds in large-scale colliding flows including self-gravity. They found that the gravity at global scale builds up large-scale filaments, while at the local scale, triggered by a combination of strong thermal and dynamical instabilities, facilitates the rapid formation of massive protostellar cores of a few hundred solar masses (*e.g.*, Sridharan et al., 2005; Beuther et al., 2005; Garay, 2005). They found that the forming clouds do not reach an equilibrium state, although they appear to be virialized. For observational context, instance, Schneider et al. (2010) used molecular line data to discern whether or not the massive star-forming gas in the DR21 region is in global gravitational collapse or in an equilibrium state supported by turbulence or magnetic fields. They found that dense cores have a lower velocity dispersion than their surrounding gas and velocity gradients that are not (only) due to rotation, and obtained a typical infall speed of $\sim 0.5\,\mathrm{km\,s^{-1}}$, and mass accretion rates on the order of a few 10^{-3} $\mathrm{M_\odot\,yr^{-1}}$ for the two main clumps constituting the filament. They also conclude that this region was formed by the convergence of flows on large scales and that it is in a state of global gravitational collapse.

More recently, Gómez and Vázquez-Semadeni (2014) found that the forming cloud

begins to undergo gravitational collapse because it rapidly acquires a mass much larger than the average Jeans mass, collapsing in a nearly pressureless way, which proceeds along its shortest dimension first, naturally producing filaments in the cloud and clumps within the filaments. They also claimed that filaments are not in equilibrium at any time, but instead are long-lived flow features continually replenished by accretion, through which the gas flows from the cloud to the clumps. Moreover, the clumps also exhibit a hierarchical nature, with the gas in a filament flowing onto a main central clump but also other, smaller-scale clumps forming along the infalling gas.

In what follows, we present a simple, idealized model of the collapse of a cloud in the presence of a filamentary perturbation, inside which a spherical perturbation exists. Our goal is to characterize the fundamental flow patterns that develops, and to investigate whether a stationary flow pattern develops, as suggested in the more complex simulation of Gómez and Vázquez-Semadeni (2014).

Draft version January 11, 2018
Typeset using LaTeX **preprint** style in AASTeX61

HIERARCHICAL GRAVITATIONAL FRAGMENTATION. III. FILAMENTARY COLLAPSE FLOW IN MOLECULAR CLOUDS

Raúl Naranjo-Romero & Enrique Vázquez-Semadeni[1]

[1] *Instituto de Radioastronomía y Astrofísica, Universidad Nacional Autónoma de México, Apdo. Postal 3-72, Morelia, Michoacán, 58089, México*

ABSTRACT

Recent observations have shown the ubiquity of filaments in molecular clouds, which appear to be funneling gas to dense cores located at the sites where various filaments converge. On the other hand, recent numerical simulations of cloud formation and collapse naturally reproduce this behaviour and suggest that the filaments constitute part of the collapse flow. Nevertheless, existing models of filamentary structures assume either radially hydrostatic structure or radial accretion, but have not considered the longitudinal flow along the filament so far. We present idealized numerical simulations of gravitationally collapsing cores and filaments embedded in globally unstable backgrounds, fully forgoing any assumption of a hydrostatic state, with the aim of extracting the essential flow features that develop in this scenario of global, hierarchical collapse. The evolution of the filamentary flow seems to approach a stationary regime in which the filamentary structure acts as a "funneling" channel, where the material radially accreted from the cloud is longitudinally "drained" down to the core, although this stationary stage is not fully attained in the prestellar stage. The value of the central flat part of the filament, fitted by a Plummer profile, approaches the typical observed values of order 0.1 pc at the end of the simulations.

Keywords: ISM: clouds — ISM: evolution — Physical Data and Processes: gravitation

1. INTRODUCTION

1.1. *Molecular Cloud substructure and star formation*

Although observation of Molecular Clouds (MCs) over many decades have shown that MCs are the nurseries of star formation, the process through which MCs evolve to form stars has undergone major transformations in recent years. Improved observations, especially with the *Herschel* Observatory (see, e.g., the review by André et al. 2014, hereafter A14) and numerical simulations (*e.g.*, Heitsch et al. 2009; Smith et al. 2011; Gómez and Vázquez-Semadeni 2014) have shown that there is a number of intermediate stages before the final formation of stars, identified as filaments, hubs and dense cores. In particular, as discussed by A14, the *Herschel* continuum observations and surveys have revealed that filamentary structures are ubiquitous in MCs, that they contain the majority of the prestellar cores in MCs, and that the formation of filaments appears to precede star formation.

This multi-stage collapse process can be understood in terms of a global, hierarchical collapse, in which small-scale collapses occur within larger-scale ones (collapses within collapses; Vázquez-Semadeni et al. 2009). Moreover, the larger-scale collapses produce filamentary structures because they occur in a nearly pressureless form, in which anisotropies are amplified (Lin et al. 1965; Gómez and Vázquez-Semadeni 2014). Hence, filaments correspond to the intermediate-scale collapse, in-between the cloud and the core scales. It is noteworthy that the latter authors argue that the collapse of clouds proceeds from the cloud at large to sheet-like objects, then to filaments, and finally to clumps, so it is possible that the filaments tend to be embedded in sheet-like clouds.

Observations from the *Herschel* Gould belt survey Arzoumanian et al. (*e.g.*, 2011); Palmeirim et al. (*e.g.*, 2013) have also found that the filaments have radial column density profiles falling off as $r^{-1.5}$ to $r^{-2.5}$ at large radii, and flattened profiles at small radii, with typical widths ~ 0.1 pc, although the universality of this width has been questioned by Panopoulou et al. (2017), who argued that it is an artifact of sampling a truncated power law with uncertainties.

Filaments appear to be highly dynamic entities. Rivera-Ingraham et al. (2017) have shown evidence that the filaments evolve, as they reported a transition from a subcritical (i.e., stable; Inutsuka and Miyama 1992) to a supercritical (*i.e.*, unstable) regime by accretion from their environment in recent observations of nearby ($d < 500\,\mathrm{pc}$) filaments (Rivera-Ingraham et al. 2016). They found that self-gravitating filaments in dense environments ($A_\mathrm{v} \sim 3$, $N_{H_2} \sim 2.9 \times 10^{20}\,\mathrm{cm}^{-2}$) can become supercritical on timescales of $\sim 1\,\mathrm{Myr}$, and suggested that filaments evolve coeval with their environment. Also, Arzoumanian et al. (2013) found that thermally subcritical filaments have transonic velocity dispersions independent of their column density, while thermally supercritical filaments have higher velocity dispersions scaling roughly as the square root of column density. They suggest that the higher velocity dispersions of supercritical filaments may not directly arise from supersonic interstellar turbulence, but instead may be driven by gravitational contraction/accretion. Finally, a number of molecular-line studies of filaments have suggested that there is a net gas flow *along* the filaments, perhaps feeding the hubs and clumps as a consequence of global collapse of the filaments (e.g., Schneider et al. 2010; Peretto et al. 2013; Kirk et al. 2013).

Many existing analytical models (e.g., Ostriker 1964; Inutsuka and Miyama 1992; Fischera and Martin 2012) consider hydrostatic equilibrium, while others (e.g., Heitsch 2013a,b; Hennebelle and André 2013), together with some numerical simulations (e.g., Clarke et al. 2016), do consider accretion. To our knowledge, however, the longitudinal flow along filaments, seen both in observations (Schneider et al. 2010; Peretto et al. 2013; Kirk et al. 2013) and reported in simulations of MC evolu-

tion (Gómez and Vázquez-Semadeni 2014) has not been discussed in analytical models or controlled numerical simulations, to investigate the essentials of the flow regime.

In this work, we extend our previous study of the collapse of an idealized spherical core embedded in a uniform, unstable background medium (Naranjo-Romero et al. 2015, hereafter Paper I), by adding a filamentary perturbation that triggers non-spherical collapse motions. We investigate the fundamental underlying flow pattern in a filamentary structure that is part of the collapse flow from the clump scale (a few parsecs) down to the core scale (a few times 0.01 pc), and discuss whether or not this regime is capable of explain some of the observed structural and kinematic features of MC filaments. In Sec. 2, we first present the numerical simulations, and in Sec. 3 we present the results concerning the flow pattern, the approximation to a stationary state, and the evolution of structural features. Next, in Sec. 4 we discuss the results and compare with the observations. Finally, in Sec. 5 we present a summary and some discussions.

2. THE SIMULATIONS

We use a spectral, fixed mesh numerical code (Léorat et al. 1990; Vázquez-Semadeni et al. 2010) to perform two numerical simulations of hierarchically collapsing density perturbations initially at rest. These are modeled by a spherical density enhancement with a gaussian radial profile ("the core") embedded in a cylindrical perturbation, also with a radial density profile ("the filament"), which in turn is immersed in a uniform density background ("the cloud"). The filament is in the z direction of the numerical box. As in Paper I, we restrict our study to the prestellar stage of the evolution because of the limitations of the numerical code, which does not have a prescription for the creation of sink particles.

We consider an isothermal gas with mean particle weight $\mu = 2.36$ at a temperature of T=11.4K, and an isothermal sound speed of $c_s = 0.2\ \mathrm{km\,s^{-1}}$ in a numerical box of size $L_{\rm box} \approx 7.1\,\mathrm{pc}$ with periodic boundaries and a resolution of 0.014 pc. The Jeans length is $L_{\rm J} = 2.24\,\mathrm{pc}$, corresponding to $M_{\rm J} = 34.21\mathrm{M}_\odot$. The box contains $60.39 M_{\rm J}$ and the gas is initially at rest and no gravity-counteracting forces such as a magnetic field or small-scale turbulence are included.

For the density background we have implemented two different configurations, corresponding to each of our two simulations. The first, labeled RunA, has a uniform density background, so that it has axial symmetry (i.e., axisymmetric), while the second (RunS) is stratified in the y direction, i.e., perpendicularly to the filament, and uniform in the direction normal to this planar stratification (see Fig. 1). This prescription emulates the case of a filament embedded in a sheet-like cloud (e.g., Vázquez-Semadeni et al. 2006; Heitsch et al. 2008; Heitsch 2013b).

In RunS, we will refer to the central plane perpendicular to the stratification direction as the *dense plane* (or simply the *central plane*). We will discuss the variation of physical quantities in three directions, one *perpendicular* to the dense plane, one *parallel* to it (*on* the plane, but perpendicular to the filament), and one along the filament, to which we will refer as the *longitudinal* direction.

Fig. 2 shows the density profiles along each of these three orientations at the initial conditions for the two simulations. The numbers next to the profiles indicate the measured FWHM for each profile. The relative amplitudes of the core over the filament are a factor of ≈ 1.49 and ≈ 1.5 for RunA and RunS, respectively, while the relative amplitudes of the filament over the central plane are ≈ 2.53 and ≈ 2.0, respectively. For RunS, the relative amplitude of the filament over the minimum density in the box is ~ 2.95. For both the core and the filament (which we generically refer to as *the substructures*), the distance from the center at which they merge with their respective parent structure naturally

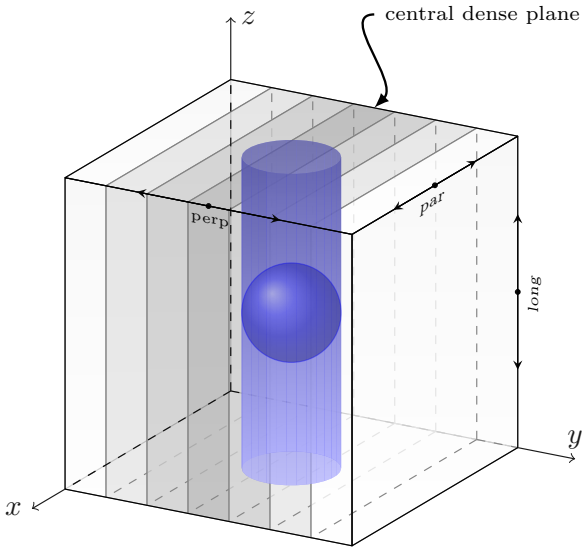

Figure 1. Illustration of the setup for the density field in the stratified simulation, RunS.

defines their respective operational boundaries[1], which are roughly one local Jeans length. That is, each structure is marginally Jeans-unstable within its parent structure.

[1] This is operationally equivalent to the way in which these objects are defined in observational column density maps.

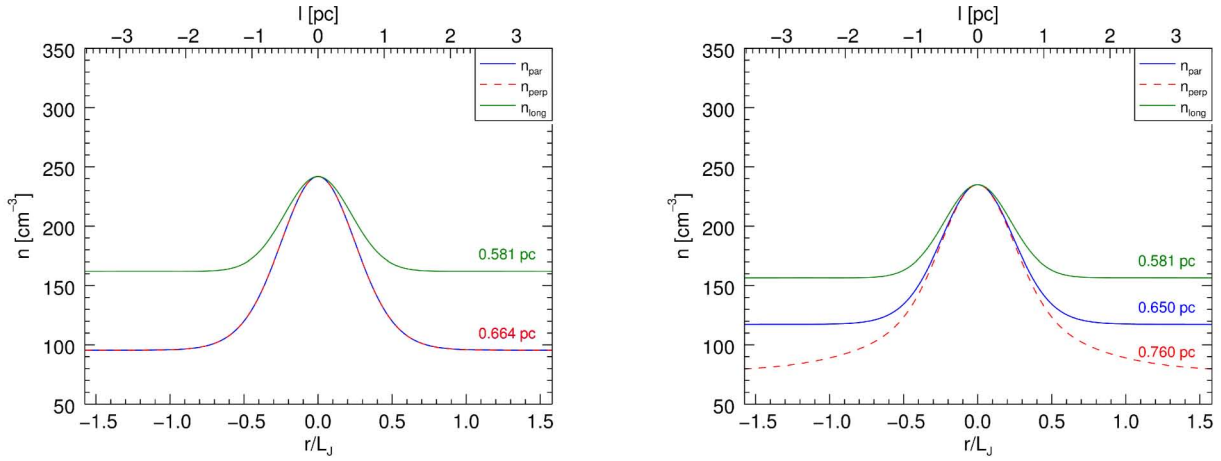

RunA RunS

Figure 2. Density profiles at the initial conditions along the three main directions, passing through the center of the computational box: the axisymmetric (RunA, left panel) and the stratified (RunS, right panel). The red lines represent the direction perpendicular to the dense plane; the blue lines, represent the direction parallel to (on) the plane (perpendicular to the filament), and the green lines, the longitudinal direction (along the filament). The numbers next to each line correspond to the FWHM of the density peak for each of the profiles. In RunA, the parallel and perpendicular profiles overlap due to the axial symmetry.

To identify the boundary on each substructure, we have chosen to use a density threshold criterion, which is a small factor $\alpha_{\rm fil}$ or $\alpha_{\rm core}$ over the density value of the corresponding parent structure:

$$\rho_{\rm bnd,fil} = \alpha_{\rm fil}\ \langle\rho\rangle_{\rm box} \tag{1}$$

$$\rho_{\rm bnd,core} = \alpha_{\rm core}\ \rho_{\rm ax,l}, \tag{2}$$

where $\rho_{\rm bnd,fil}$ (respectively $\rho_{\rm bnd,core}$) is the density at the filament (resp. core) boundary, and $\rho_{\rm ax,l}$ is the density at the axis of the filament but a distance l away from the border of the computational box. The latter will be useful when measuring properties of the filament, away from the core. Finally, $\alpha_{\rm fil}$ and $\alpha_{\rm core}$ are constants slightly larger than unity.

Additionally, it is useful to identify two different regions along the filament, depending on whether they contain the core or not (see Fig. 3) for comparison with observed cores and filaments, respectively. We choose the off-core region roughly halfway between the center of the core and the border of the computational box, a location safely removed from the core while not being too strongly affected by the periodic boundaries of our box.

To investigate the evolution of the filament-core systems, we have selected several timesteps in both runs (see Table 1).

3. RESULTS

In this section, we first describe the uniform-background, axisymmetric simulation (RunA), and then the stratified-background simulation (RunS). All figures are labeled with the type of background setup, the timestep, and the orientation along which we have calculated the plotted quantities for each panel.

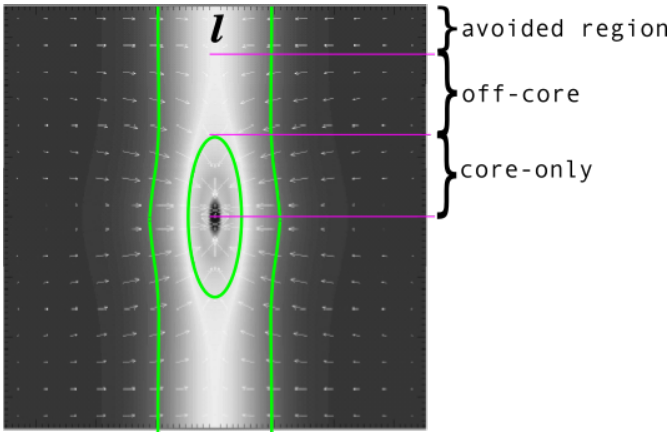

Figure 3. Illustration of the selection of the core and non-core filament sections.

Table 1. Selected timesteps for the runs.

Run	Timestep	Time	
		($t_{\rm ff}$)	(Myr)
RunA	0	0.00	0.00
	1	0.30	0.11
	16	0.53	1.77
	33	1.09	3.64
RunS	0	0.00	0.00
	1	0.03	0.11
	16	0.53	1.77
	31	1.02	3.42

3.1. *Overall evolution*

Figure 4 shows cross sections of the (volume) density field of the two simulations on various planes passing through the center of the computational box (see labels), with the normalized velocity field overlaid. It is noteworthy that RunS produces a ribbon-like filament instead of a cylindrical filament. The ranges in the color scales correspond to the minimum and maximum values of the number density (in $\rm cm^{-3}$) in the overall evolution for each run. The color bar also indicates the values of the density at the boundaries of the filament and the core (labeled f and c), according to eqs. (1) and (2), with $\alpha_{\rm fil} = 1.3$ and $\alpha_{\rm core} = 9$. The horizontal lines define a slice across the filament at a fixed distance $L_{\rm J,init}/2 \sim 1.12\,$pc away from the boundary at the initial conditions, where we have computed various physical quantities.

In the axisymmetric run (left panels), the position of the filament's boundary does not vary significantly throughout the evolution (except in the on-core region), growing from $\sim 0.73\,\mathrm{pc}$ at the initial conditions to $\sim 1.3\,\mathrm{pc}$. A similar situation occurs for the stratified run in the direction perpendicular to the plane. On the other hand, for the stratified run in the parallel direction (on the plane), the filament boundary steadily moves outwards. Concerning the core boundary, it is seen that in all cases it changes dramatically in shape, evolving from a nearly spherical shape to a highly elongated one.

The density field is almost uniform along the filament and away from the core, and in the background region away from the filament. Also, as suggested in the less idealized simulation of Gómez and Vázquez-Semadeni (2014), the velocity field smoothly changes direction as it approaches the filament, being mostly perpendicular far from the filament to becoming longitudinal in the filament's central axis, pointing towards the core. It is important to note that *no shocks develop during the prestellar evolution.* In addition, the velocity field direction remains quite constant throughout the evolution, suggesting a stationary flow. We return to this point below in sec. 3.2.

Figure 5 shows the density profiles for the selected timesteps in both simulations, with RunA shown on the two top panels and RunS shown in the three bottom panels, respectively. The various lines shown correspond to the various timesteps we consider (see Table 1). The longitudinal-slice plots (right panels on the two rows) show the core on top of the filament, while the other plots show the filament on top of the background cloud.

The longitudinal slices (right top and bottom panels) confirm that the density in the filament, away from the core, increases steadily in time through accretion from the cloud, although in RunA the increase rate appears to decrease towards the final stages of the prestellar evolution. This slowing of the increase might be suggestive of an approach to stationarity.

Figure 6 shows, in its top panels, the evolution of the mass of the whole filament (including the core, labeled "fil+core", shown with blue lines) and of the filament without the core (labeled "fil", shown with red lines). The bottom panels show the evolution of the linear mass density (often misleadingly referred to as the "line mass" in the literature) for the filament+core system and the filament alone. Finally, the green lines in the bottom panels show the linear density for the filament+core system but only out to the fixed value of the filament's radius from the initial conditions.

It is interesting to note that the filament evolution seems to transition from a regime of *increasing* rates of mass and linear density growth to a regime of *decreasing* growth rates, again suggesting an approximation to a stationary regime (which, however, does not seem to be reached during the prestellar stage investigated in this paper).

Figure 7 shows the radial profile for the number density, column density and *total* velocity for RunA (left column) and for RunS, both in the direction parallel to the dense plane (middle column) and perpendicular to it (right column). The solid lines show the profiles at the center of the box (*i.e.*, at the position of the core), while the dashed lines show the profiles midway between the core and the boundary; *i.e.*, on the off-core region of the filament. In this figure, we use a logarithmic radial axis to emphasize the internal structure of the filament.

From the solid lines, we can see that the collapse in the on-core position proceeds from the outside-in, in a similar way as in the spherical case described in Paper I and other works (e.g., Gómez et al. 2007; Gong and Ostriker 2009). Early in the evolution, the velocities are largest at large radial distances from the axis of the filament, while the inner parts develop a velocity profile roughly linear

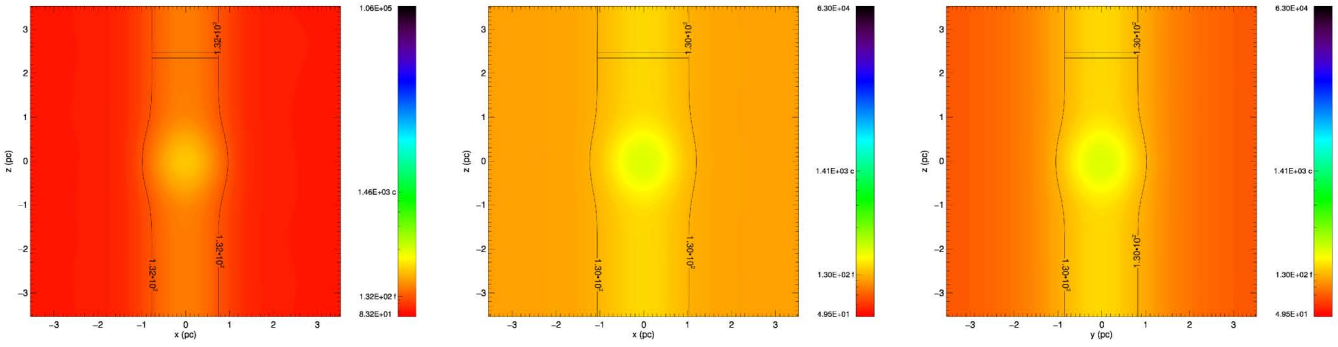

(RunA-00-par/perp) (RunS-00-par) (RunS-00-perp)

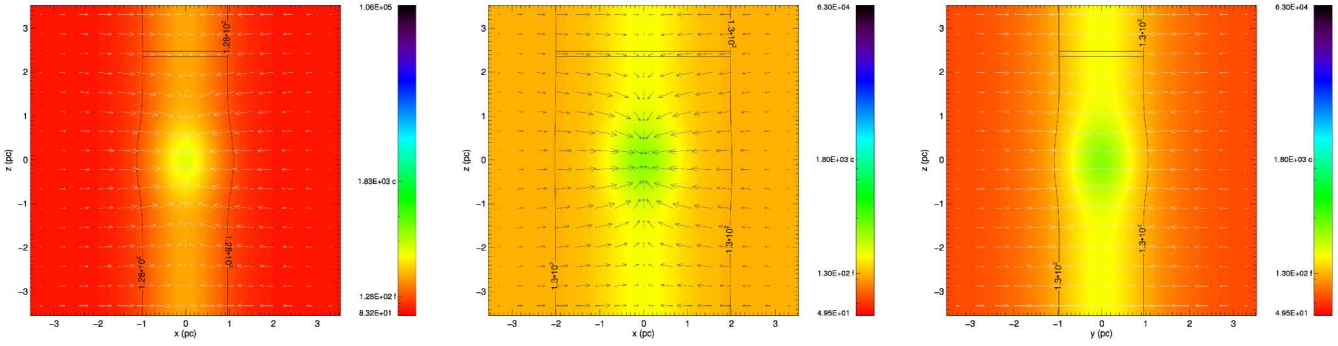

(RunA-16-par/perp) (RunS-16-par) (RunS-16-perp)

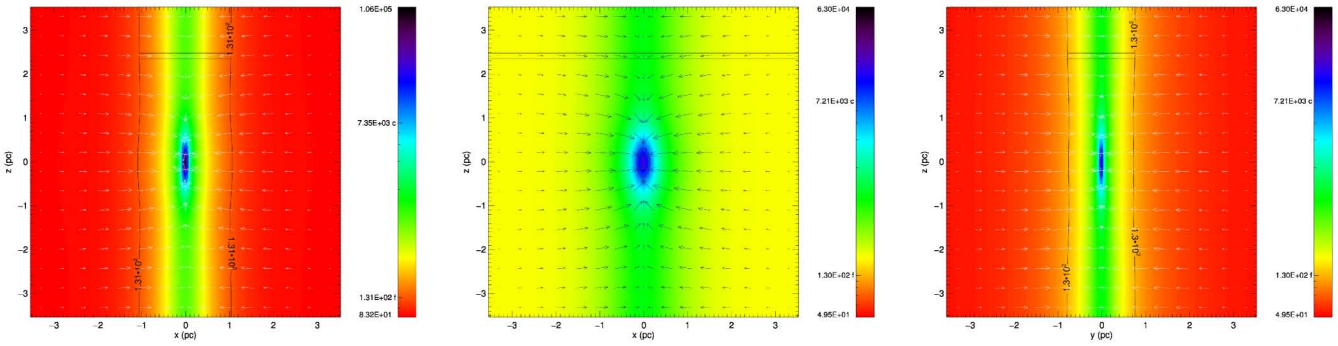

(RunA-33-par/perp) (RunS-31-par) (RunS-31-perp)

Figure 4. Density images for both simulations on the central plane (left and middle columns) and the perpendicular plane (right column) at the initial conditions (top panels), an intermediate timestep (middle panels) and at the end of the simulation (bottom panels). The labels indicate the run, timestep and orientation of the each map. Velocity vectors are normalized to the maximum velocity on each simulation. The evolution time for each panel corresponds to that on Table 1.

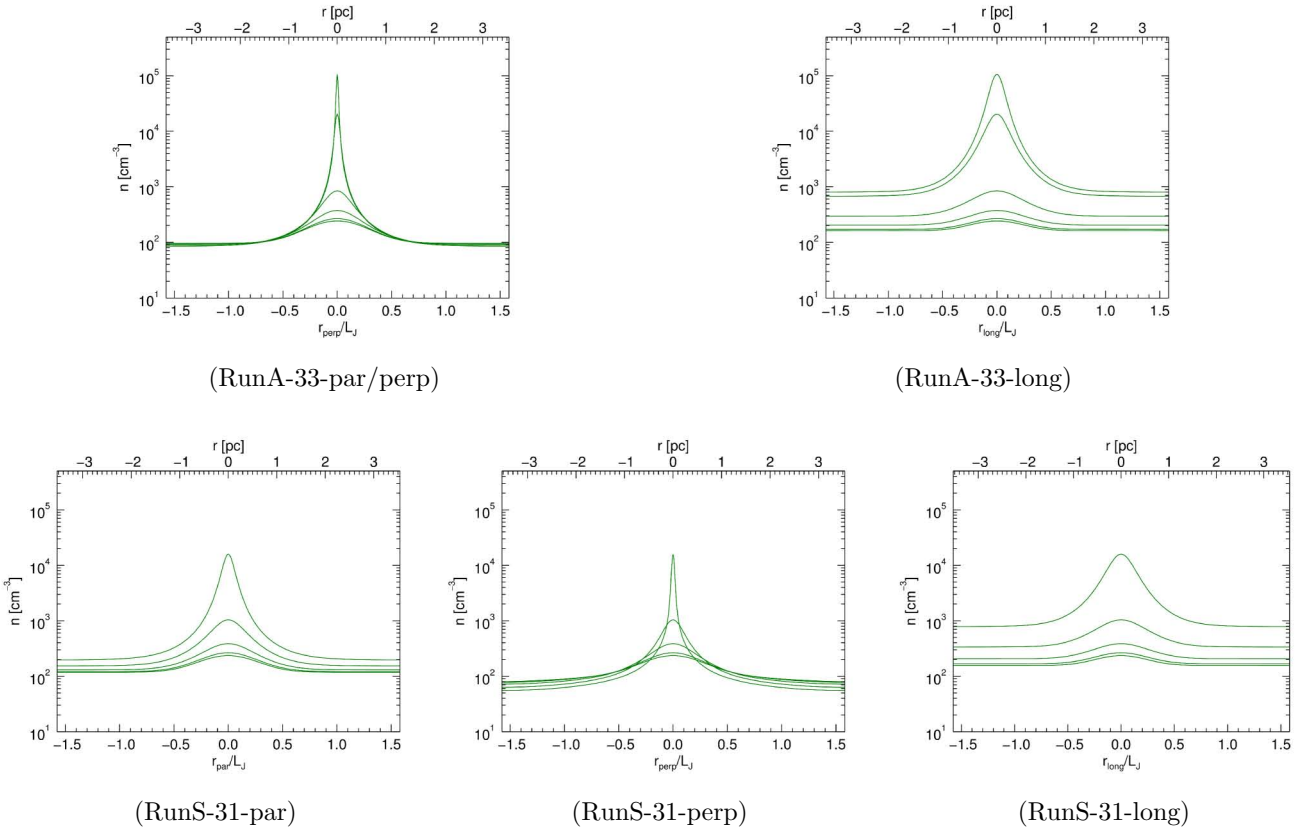

(RunA-33-par/perp) (RunA-33-long)

(RunS-31-par) (RunS-31-perp) (RunS-31-long)

Figure 5. Evolution of the density profile for labeled runs at the end of each simulation. The evolutionary steps shown in each panel corresponds to those listed in Table 1.

with radius. At timestep 9, $t \approx 0.3\ t_{\rm ff} \approx 1.0\,{\rm Myr}$[2], a transonic point appears at $\sim 0.5\,{\rm pc}$ away from the center of the filament, that then splits into two points that move in opposite directions (*i.e.*, one outwards and one inwards) from the position of the initial transonic point. At later timesteps, these transonic points enclose a region of almost uniform supersonic inward velocity. The filament shows a flattened density profile in the inner regions where the velocity is uniform, approaching an r^{-2} slope.

In contrast, from the dashed lines (*i.e.*, in the off-core region), we can see that the filament develops a uniform radial profile of the total velocity, almost over its full radial extension and throughout the evolution, with no drop towards the central axis. Also, the volume density profile is seen to be flat at the central parts of the filament and to approach a power-law at the external parts (towards the end of the simulation), until the radius at which it merges with the uniform density background. Together with the change in direction of the velocity from radial to longitudinal seen in Fig. 4 at the off-core positions, this implies that the momentum is completely transferred from the radial to the longitudinal direction near the filament axis.

Similarly to the Figure 7, Figure 8 shows the radial profiles along the longitudinal direction along the filamentary structure in the last timestep of each simulation. The behaviour is quite similar to that of the core on top of the uniform density background described in Paper I, with the main

[2] From hereafter, $t_{\rm ff}$ is the free-fall time at the initial conditions

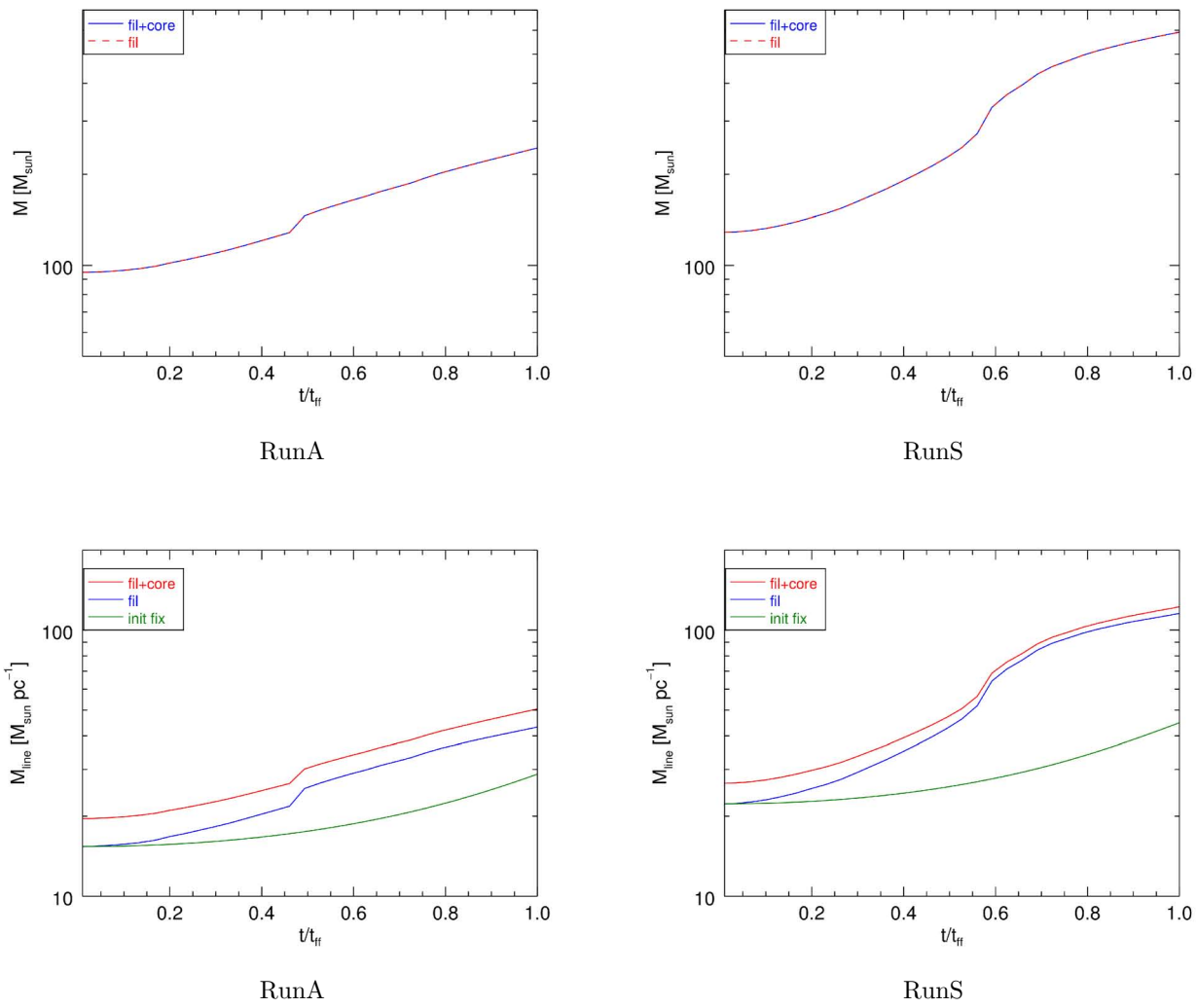

Figure 6. Mass per unit length evolution of the identified filament regions.

difference that the flat inner part of the density and column density profiles for the core is more extended.

Figure 9 shows the radial column density profile of the filament and a fit of a Plummer-like function at the end of the simulations. The parameters of the fitting are the central flat part of the filament's radial profile, $R_{\rm flat}$, its power-law exponent p, and A_p (see also Tables 8-2), which is a finite constant factor for $p > 1$. For comparisons, it also shows the profile for an infinite, hydrostatic isothermal cylinder, for which $p = 4$ (Ostriker 1964)[3], and the derived profile for observed filaments, for which $p = 2$ (Arzoumanian et al. 2011). It also shows the profile of an observed filament from Arzoumanian et al. 2011, with the upper and lower errors denoted by the dotted lines. We can see that the fitted values of the slope, $p = 1.33$ for RunA, and $p = 1.7$ and $p = 1.25$ for RunS in the perpendicular and

[3] For an infinite isothermal filament in hydrostatic equilibrium, $A_p = \pi/2$, and $R_{\rm flat}$ corresponds to the thermal Jeans length at the center of the filament.

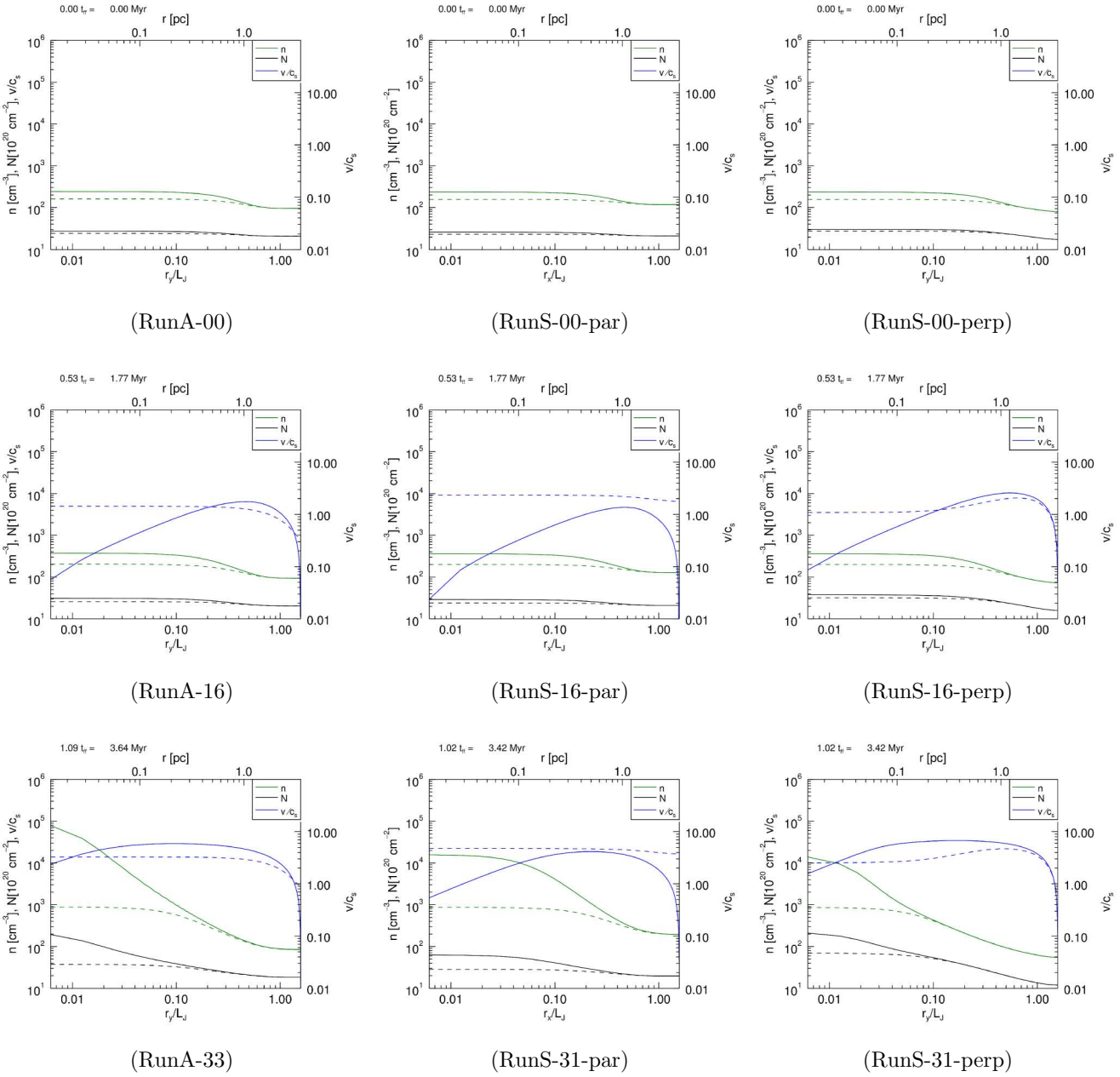

Figure 7. Radial density, column density and velocity profiles on-core (solid) and off-core (dashed) for labeled runs at the initial conditions (top), an intermediate timestep (middle) and final timestep (bottom). The evolution time for each panel corresponds to that on Table 1.

parallel directions, respectively, are in general less than the observed slope, although it is possible that the final slope is not attained until after the formation of a singularity (*i.e.*, a protostar), which we do not consider here.

Figure 10 shows the evolution of $R_{\rm flat}$ obtained by fitting the column density profiles (see Fig. 9) for both runs. As we can see from both panels, even though at early times the fitted values of $R_{\rm flat}$

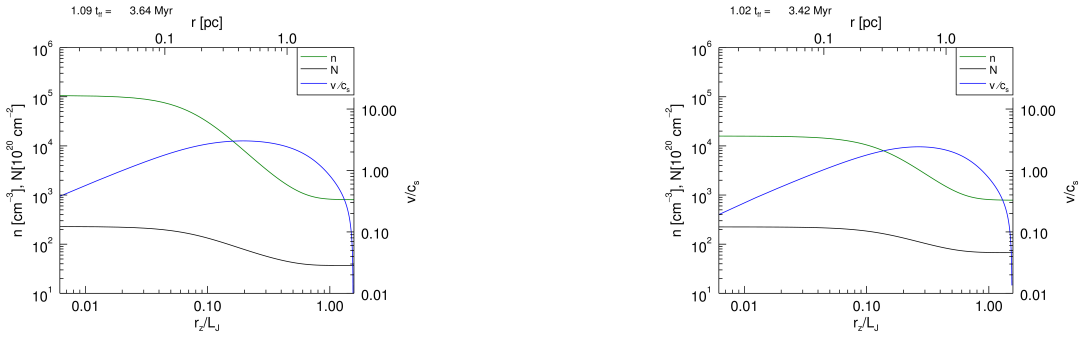

(RunA-33-long) (RunS-31-long)

Figure 8. Radial density, column density and velocity profiles on-core (solid) and off-core (dashed) for labeled runs at final timestep. The evolution time for each panel corresponds to that on Table 1.

Table 2. Fitted parameters for the column density profile for RunA.

timestep	$R_{\rm flat}$ (pc)	p	A
0	0.81	1.20	4.03
16	0.61	1.23	3.65
33	0.18	1.32	0.06

are quite larger than the typical values ~ 0.1 pc reported from *Herschel* observations, at later times, this typical size scale is approached.

It is noteworthy that the evolution of $R_{\rm flat}$ in the perpendicular direction in RunS is very similar to the evolution in RunA, decreasing by a factor ~ 5 between the initial and final states. For the parallel direction in RunS, the variation in $R_{\rm flat}$ is even lower, on the order of a factor of ~ 2 between the initial and final states. We speculate that, after singularity formation, $R_{\rm flat}$ may become constant as a consequence of the stationarity of the system (as long as the gas supply from the cloud remains). This may explain the apparent observed "universality" of the filament widths (*e.g.*, Arzoumanian et al. 2011; Palmeirim et al. 2013; André et al. 2014).

Table 3. Fitted parameters for the column density profile for RunS along parallel (top) and perpendicular (bottom) orientations.

timestep	$R_{\rm flat}$ (pc)	p	A
0	1.48	1.67	2.59
16	1.02	1.71	2.78
31	0.19	1.69	0.73
0	0.945	1.15	3.41
16	0.78	1.18	2.77
31	0.36	1.24	0.16

3.2. *The approach to a stationary regime and mass flux in the filament*

As discussed in Sec. 3.1 (cf. Fig. 4), the velocity field in the simulations tends to remain constant in space, in both magnitude and direction, as time advances, suggesting an approach to a stationary regime. To further search for evidence of this, in Fig. 11 we plot the histogram of the angles of the velocity vectors with respect to the horizontal axis at various times. It can be seen that, in both runs, the relative frequency of these angles has an almost constant overall shape over time, its peak shifting only few degrees throughout the evolution, reinforcing the view that the velocity field remains almost constant in time.

In fact, an approach to stationarity is expected. At early times, when the filament density is increasing, the longitudinal mass flux along the filament, ρv_z, also increases, even if the longitudinal velocity, v_z, remains constant, precisely due to the the density increase. Eventually, the longitudinal mass flux must become comparable to the radial mass flux onto the filament from the cloud. When this happens, however, the filament density must begin to decrease again, reducing the longitudinal flux. So, it appears that a stationary regime where the longitudinal mass flux balances the radial one, may be an attractor for the flow.

To test numerically the hypothesis of a stationary regime, we have selected a slice of the filament of thickness 10 pixels, at a distance $l = L_{\rm J,init}/2$ from the boundary, to measure the mass per unit length (the linear mass density, λ), as well as the longitudinal and radial mass fluxes in the filament. This choice for the slice was made so that the slice is sufficiently removed both from the core, since we are interested in the filament in this case, and from the boundary of the numerical box, where the longitudinal flow velocity is forced to remain at zero.

If the flow approaches stationarity, then the mass flux *into* the slice, $\dot{M}_{\rm in}$ (both through the top "lid" of the slice, in the direction toward the core, as well as in the radial direction, due to accretion from the cloud) must approach the flux *out of* the slice, $\dot{M}_{\rm out}$, through its bottom lid. That is, we

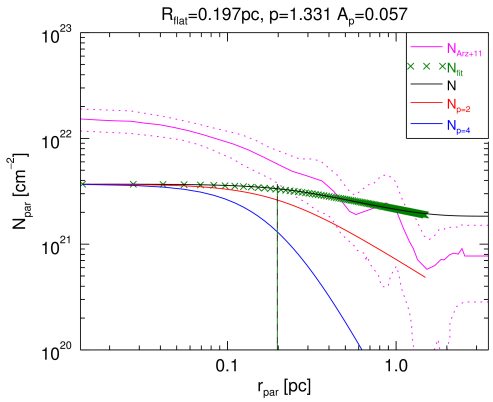

(RunA-33)

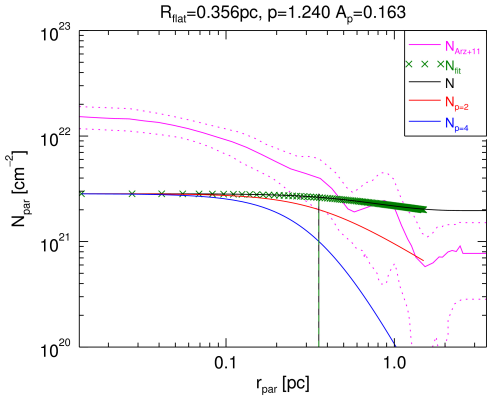

(RunS-31-par)

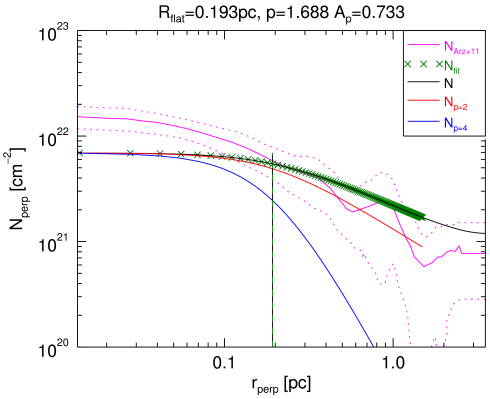

(RunS-31-perp)

Figure 9. Radial column density profiles of the filament at the off-core position (black) at the end of the simulations. The green crosses indicate the points used for computing the best-fit parameters using a Plummer-like function. For comparison, the plot shows the profile for a typical observed filament from (Arzoumanian et al. 2011) (magenta continuous line) with errors delimited by the magenta dotted curves, as well as the characteristic profile for an infinite isothermal filament ($p = 4$) and the observed filaments ($p = 2$).

expect that the total mass change rate ratio,

$$\mu_{\rm tot} \equiv \frac{\dot{M}_{\rm in}}{\dot{M}_{\rm out}} \sim 1, \tag{3}$$

where

$$\dot{M}_{\rm in} = \int_A \rho \boldsymbol{v} \cdot \boldsymbol{dA} + \int_B \rho \boldsymbol{v} \cdot \boldsymbol{dB},$$
$$\dot{M}_{\rm out} = \int_C \rho \boldsymbol{v} \cdot \boldsymbol{dC}, \tag{4}$$

and A is the area of the top lid, B is the perimetral area of the slice, and C is the area of the bottom lid (see Fig. 12).

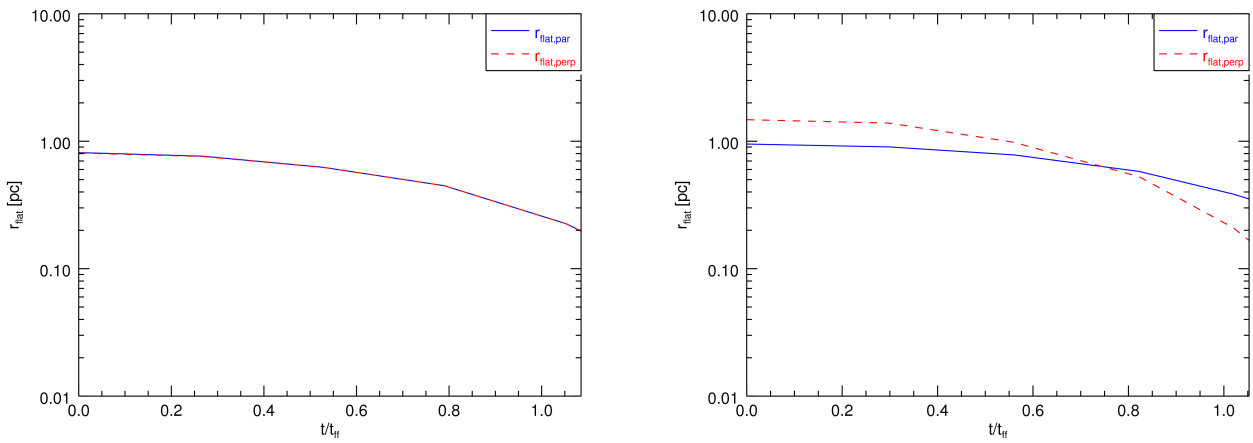

(RunA) (RunS)

Figure 10. Evolution of $R_{\rm flat}$ for both runs.

Figure 13 shows the evolution of $\mu_{\rm tot}$ through the slice for the two runs. As we can see, the mass flux ratio for the axisymmetric run has not yet reached unity by the time it stops, although $\mu_{\rm tot}$ is clearly approaching unity. For the stratified run, on the other hand, $\mu_{\rm tot}$ does reach unity, although, somewhat surprisingly, it exceeds this value at the end of the simulation and likely would continue to grow. Although this behaviour may be transient, it is necessary to perform simulations that evolve past the time of formation of a singularity (a protostar), which, however, requires us to use a different numerical code. We therefore postpone this task to a future study.

Another relevant diagnostic is the ratio of the mass accretion rate onto the slice through the perimetral area, $M_{\rm in,B}$, to the total mass rate of change of the slice itself, $\dot{M}_{\rm slice}$. These are respectively given by

$$\dot{M}_{\rm slice} = \dot{M}_{\rm in} - \dot{M}_{\rm out}, \tag{5}$$

and

$$\dot{M}_{\rm in,B} = \int_B \rho \boldsymbol{v} \cdot \boldsymbol{dB}. \tag{6}$$

We then expect that, at early times, most of the mass change in the slice is due to the perimetral accretion, and so the mass rate ratio

$$\mu_{\rm B} \equiv \frac{\dot{M}_{\rm in,B}}{\dot{M}_{\rm slice}} \tag{7}$$

should be close to unity. Instead, at late times, if the mass of the slice tends to a constant ($\dot{M}_{\rm slice} \to 0$), then this ratio should diverge, indicating that the mass accreted through the perimetral area, plus the mass accreted through the top lid, is expelled through the bottom lid, and so the perimetral accretion no longer contributes to an increase in the slice's mass.

Figure 14 shows the evolution of $\mu_{\rm B}$ for the two simulations. For both, this ratio is indeed close to (although slightly larger than) unity at early stages. This means that the mass flux through the perimetral area is close to, but slightly larger than, the total mass increase rate of the slice. This in

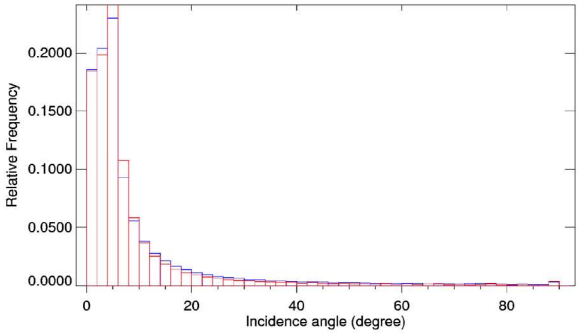

(RunA)

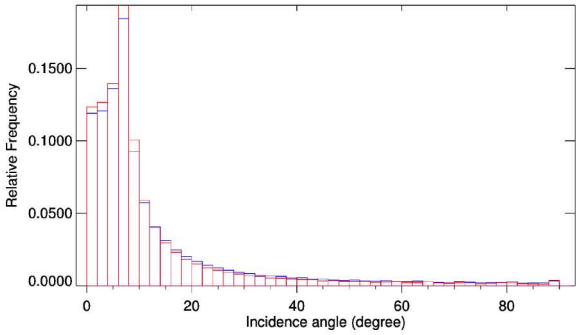

(RunS-par)

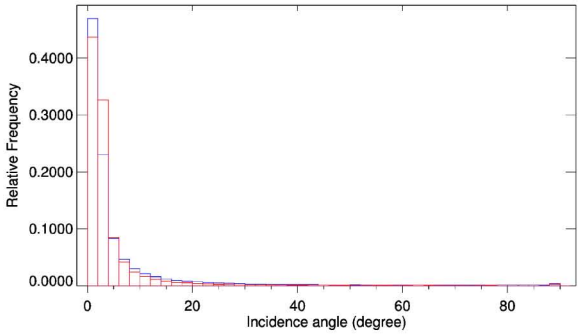

(RunS-perp)

Figure 11. Histogram of velocity vectors with respect to the horizontal axis for labeled runs. The initial timestep is shown in blue and the final timestep in red.

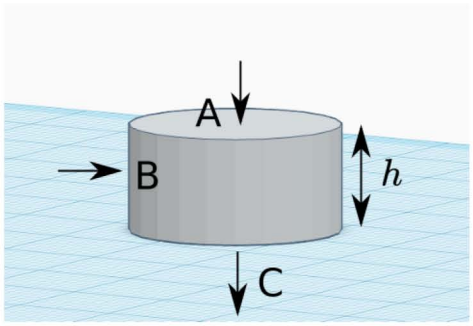

Figure 12. Illustration of mass flow through the filament's slice.

turn implies that, during the early stages, this perimetral mass flux is the main driver of the mass growth of the slice, although some of it is lost by evacuation from the bottom lid.

On the other hand, at later times, the ratio begins to increase, indicating that the evacuation (through the bottom lid) increases in relation to the perimetral inflow rate, so that the mass of

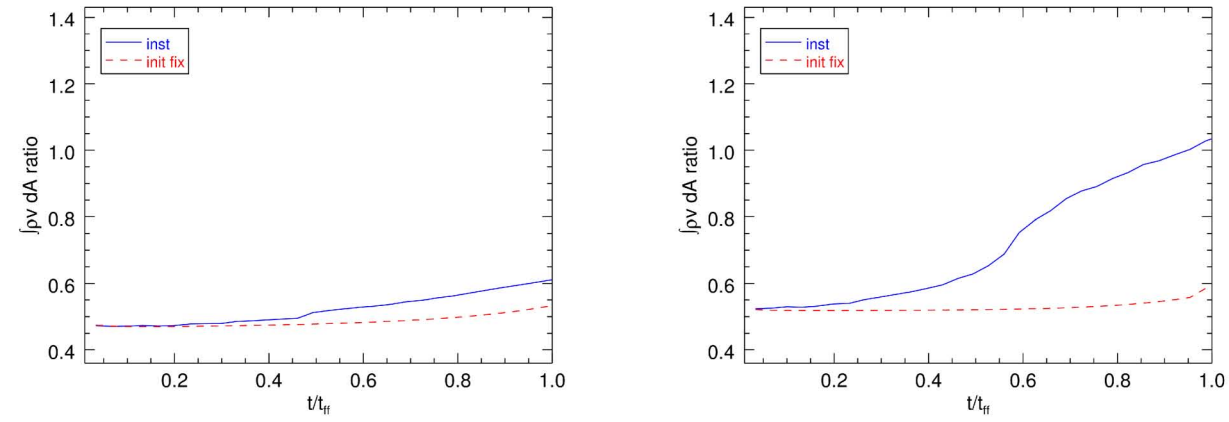

(RunA) (RunS)

Figure 13. Evolution of the mass-flux rate ratio, $\mu_{\rm tot}$, (eq. [3]) in the slice. The blue solid lines indicate the ratio calculated for the mass fluxes across the moving filament boundary defined by eq. (1). The red dashed lines indicate the fluxes calculated across a boundary fixed at its initial position.

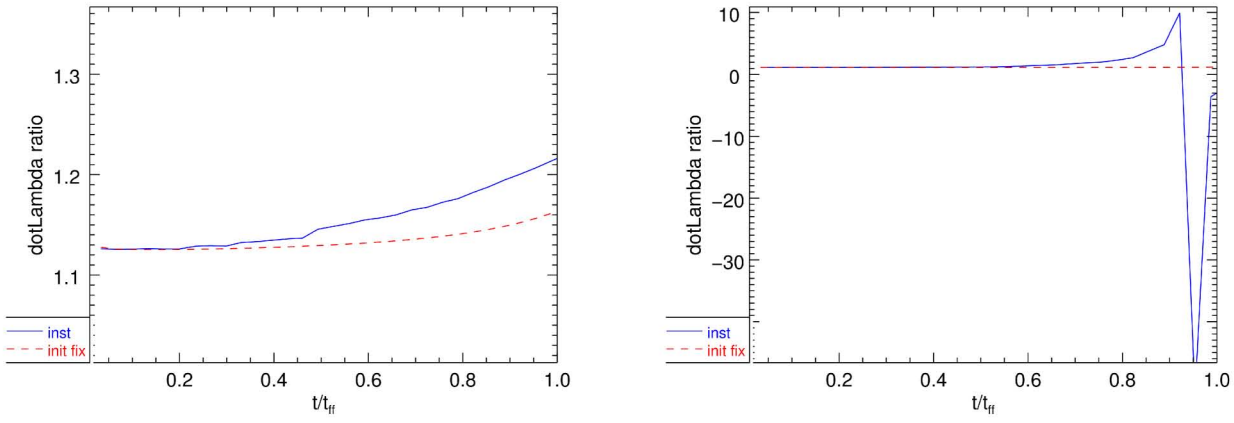

(RunA) (RunS)

Figure 14. Evolution of the ratio of perimetral accretion rate to total mass change rate, $\mu_{\rm B}$, (eq. [7]) for the filament slice. The blue solid lines indicate the ratio calculated for the mass fluxes across the moving filament boundary defined by eq. (1). The red dashed lines indicate the fluxes calculated across a boundary fixed at its initial position.

the slice begins to approach constancy (its mass rate of change decreases); i.e., the slice approaches stationarity. In fact, for RunS, after $t \sim 0.7t_{\rm ff}$, $\mu_{\rm B}$ increases strongly and changes sign, indicating that the total mass change rate for the slice becomes negative; i.e., the slice begins to lose mass. Fig. 15, however, shows the evolution of the mass of the slice (blue lines) for the two runs. Surprisingly, the slice mass is growing monotonically in the two runs, a fact that appears inconsistent with the conclusion from the mass change ratios that the slice begins to lose mass at $t \approx 0.93t_{\rm ff}$ in RunS.

This apparent inconsistency is resolved by noting that, so far, we have considered the boundary of the filament (and thus the perimetral area of the slice) using the definition given by eq. (1). As discussed in Sec. 3.1, with this definition the boundary of the filament in RunS moves outwards as it evolves. Thus, the mass growth occurs because the filament radius increases, in spite of the fact that the net instantaneous mass flux across the filament's boundaries is negative. This behaviour is confirmed by the red dashed lines in Figs. 13, 14, and 15, which show the evolution of the ratios of mass increase and the slice mass when the boundary of the filament is forced to remain fixed at its initial radius. In this case, it is seen in Fig. 14 that the ratio of the perimetral accretion rate to the total mass rate of change, $\mu_{\rm B}$, remains close to unity, and, while it still increases, it does so much more slowly than in the moving-boundary case.

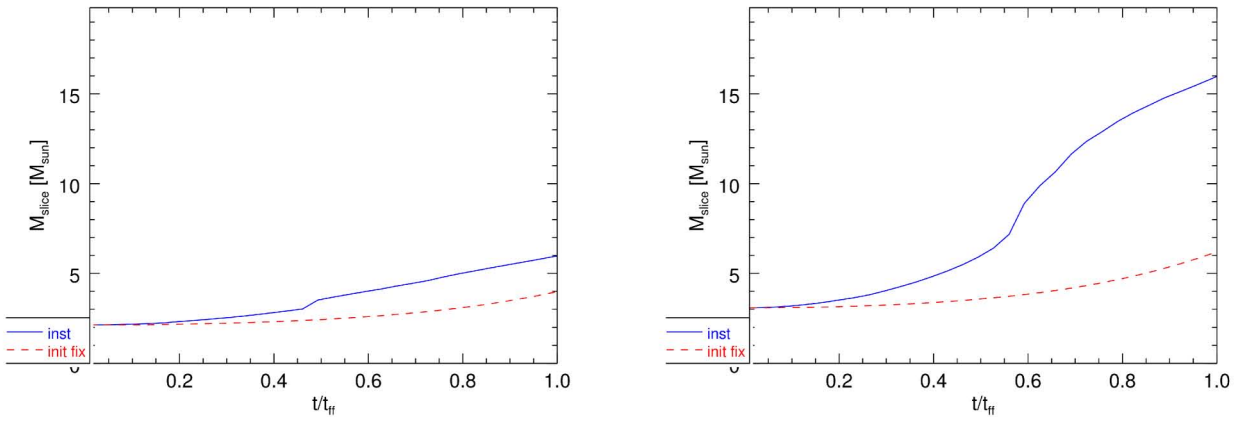

(RunA) (RunS)

Figure 15. Slice mass *vs.* time. The blue solid lines indicate the mass contained within the moving filament boundary defined by eq. (1). The red dashed lines indicate the mass contained within a boundary fixed at its initial position.

It is also worth noting in Fig. 15 that, in the case when the filament boundary is defined dynamically by eq. (1) (solid blue lines), the filament slice mass grows in two stages, first accelerating and then decelerating, in both simulations. Instead, when the filament boundary is defined to remain fixed at its initial position, the filament slice mass growth curve is always concave —i.e., always accelerating, at least during the prestellar stage considered in this work. This behaviour suggests that the more extended boundary represents a region where the approach to stationarity has advanced further than the region enclosed by the fixed boundary, which remains further inside the filament.

3.3. *Comparison with observations of prestellar cores*

As in Paper I (see Sec. 4.1 and Fig. 3 there for further details about the observed prestellar cores and the simulated core), Fig. 16 shows a plot of $M_{\rm core}/M_{\rm BE}$ *vs.* $M_{\rm core}$, where $M_{\rm core}$ is the core mass and $M_{\rm BE}$ is the Bonnor-Ebert mass for the mean density and temperature of the core. This diagram was studied by Lada et al. (2008), who concluded that in the Pipe molecular cloud, most low-mass cores are gravitationally unbound and confined by external pressure. In Fig. 16, we have plotted the

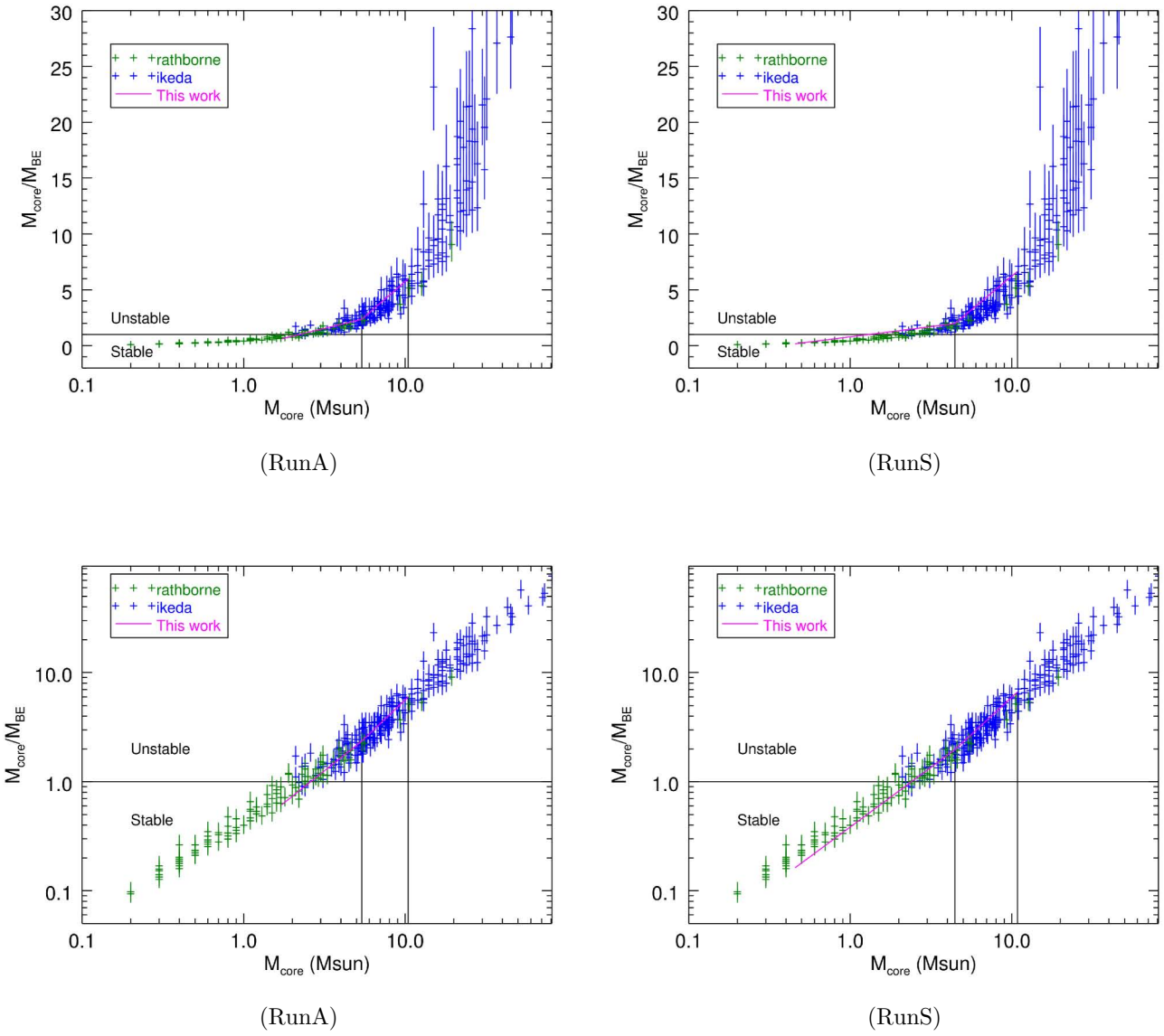

Figure 16. Evolution in the diagram $M_{\rm core}/M_{\rm BE}$ *vs.* $M_{\rm core}$ (*cf.*, Lada et al. 2008) of the cores (immersed in the filaments) from the axisymmetric (left) and stratified (right) simulations and the observed cores from Table 2 in (Rathborne et al. 2009), and Table 1 from (Ikeda et al. 2007). Each point has a vertical error bar that spans the values of the BE-mass at temperatures of 10 and 13 K (top and bottom respectively). The bottom panels show the same data as those in the top panel, but with a logarithmic vertical axis, to better appreciate the location of the low-mass cores.

same sample of observed cores from the Pipe (Rathborne et al. 2009) and the Orion (Ikeda et al. 2007) clouds, as well as the evolutionary track in this diagram of our filament-embedded cores. Note that in the case of the cores from the Pipe, even though not all prestellar cores in the sample of (Rathborne et al. 2009) are extracted from the main filamentary structure, it has been suggested that the molecular cloud is indeed formed by the collision of filaments (Frau et al. 2015). The

Orion molecular cloud is more complex, but the sample includes prestellar cores from a filamentary structure in the north part of the cloud and also prestellar cores within the south region of more diffuse emission where no clear filamentary structure has been found (Ikeda et al. 2007).

From Fig. 16, we can see that the evolutionary track of our cores, with their boundaries defined by eq. (2), using a threshold $\alpha_{\rm core} = 9$, tracks almost exactly the locus of the observed prestellar cores.

The agreement between the pictures of formation of prestellar cores immersed in both, a filamentary structure (this work) and in apparent isolation[4] (Paper I), indeed suggests that *the GHC scenario is a plausible mode for star formation from the large scale and down to the small scale (i.e., cloud-sheet-filament-core), where the main physical mechanisms are the gravitational focusing and the direct accretion from the different successive hierarchies in the sequence of collapse.*

Note, that we had to choose here a factor $\alpha_{\rm core} = 9$ that is rather large compared to those (1.125, 1.2, and 1.5, respectively) utilized in Paper I. Lower choices of this factor resulted in the evolutionary tracks being displaced to the right (higher masses) in this diagram. It remains to be tested whether this choice is consistent with regular observational core-definition procedures, a task that we defer to a future study.

4. DISCUSSION

The results from the previous section can be summarized as follows:

1. We have numerically simulated the collapse of a filamentary perturbation containing a spherical enhancement (a core) in its center. We considered two variants of this filamentary collapse, one with axial symmetry (RunA), and one with additional stratification in one of the directions perpendicular to the filament (RunS). The latter represents the case in which the filament is in turn embedded in a sheet-like cloud.

2. The presence of the filamentary perturbation changes the symmetry of the collapse flow which, away from the core, proceeds first toward the filament, and smoothly changes direction as it approaches the filament axis, to becoming longitudinal there, oriented towards the core. No shocks develop at the filament axis.

3. To measure properties of the filament and the core, and intending to represent common observational procedures, we defined their boundaries in terms of a certain density enhancement above their respective parent structures (eqs. [1] and [2]). Thus defined, both, the filament and the core evolve by growing in mass. In RunS, the filament radius grows over time on the dense central plane (the "parallel" direction). In the direction perpendicular to this plane, and in RunA, the filament radius remains roughly constant in time.

4. The filament is never hydrostatic, and instead seems to approach a stationary regime in which the material accreted through the boundary flows longitudinally toward the core. We suggested that such a stationary regime may be an attractor for the evolution of the filament, because, if the longitudinal "drainage" of material is lower than the peripheral accretion, the filament density must increase, increasing the longitudinal flux. Conversely, if the longitudinal flux exceeds the peripheral accretion, then the filament density must decrease, reducing the longitudinal flux.

[4] Apparent, because the cloud itself indeed is their large-scale parent structure.

5. In both runs, we measured the evolution of various mass flux rates, as well as the total rate of mass change and their ratios, in a slice in the filament far from the core, to determine whether or not the slice mass approaches stationarity, and if so, how it is approached. The mass fluxes were measured across the perimetral boundary of the filament and along the filament. We found that the perimetral mass flux first causes an increase in the filament mass, but later the longitudinal flux tends to cancel this effect. The stationary state, however, is not fully attained during the prestellar stage we have considered in this paper, and may require consideration of the subsequent protostellar stages of evolution. We plan to address this possibility in future work.

6. We found that the radial column density profile in the filament away from the core can be fitted by a Plummer profile, and that the radius of the flat central part slowly decreases in time, approaching the "typical" observed values of order 0.1 pc at the end of the simulations, near the time of protostar formation in the core. The profile on the filament retains its flattened shape near the filament axis even at the time when the central density in the core diverges (the time of protostar formation). This behaviour is due to the fact that, while the mass is accumulated at the core, it just "traverses" the filament but does not accumulate there, thus never causing a divergence of the density in the filament axis. The filaments simply act as intermediary "funnels" for the material to flow from the cloud to the core.

4.1. *Comparison with previous work*

Our results are consistent with those of simulations of the formation and evolution of turbulent molecular clouds (e.g., Heitsch et al. 2009; Smith et al. 2011; Gómez and Vázquez-Semadeni 2014), and reinforce the notion that the filaments constitute intermediate stages of the collapse. Our idealized setup, of a perfectly cylindrical geometry with an initially spherical central core, allows us to focus on the essential flow features of filament-core systems.

We find that, as in calculations of spherical collapse (e.g., Larson 1969; Penston 1969, see also Paper I), a shock does not develop anywhere in the system before the formation of a singularity (the time of protostar formation). Moreover, along the filament, the growth rate of the central density in the filament slows down, so that it is nowhere near developing a singularity at the time when this occurs in the core (the end time of our simulations). Indeed, the flow seems to approach a stationary regime where the mass flux across the perimetral boundary of the filament is drained into the core by a longitudinal mass flux. Since the entire prestellar stage, however, may be considered as a transient phenomenon leading to a steady similarity flow arising after protostar formation, we only see the approach to this steady flow during the prestellar stages we have investigated.

The approached steady state may be considered the filamentary analogue of the similarity flow developing in spherical structures after singularity formation (e.g., Shu 1977; Whitworth and Summers 1985). For these, Murray et al. (2017) recently showed that the density at a given radius approaches a constant, implying that the flow becomes stationary. In this spherical case, the mass is drained into the singularity, so that the latter increases its mass, but the gaseous core may maintain a stationary density and velocity configuration (neglecting the increase in the core mass). In the filament, our results suggest that the drainage into the core allows the filament to also develop stationarity, with our simulations approaching, but not quite reaching, it. Moreover, in the case of the filament, because the ultimate mass sink (the center of the core) is far from the middle position on the filament, the

stationary density at the filament axis remains at some finite value, and allows the radial density and column density profiles to remain flat for a long time. Thus, although $R_{\rm flat}$ does evolve in time during the prestellar stages, it does so rather slowly, and approaches a finite stationary value, seemingly consistent with observed values (Arzoumanian et al. 2011; Palmeirim et al. 2013).

5. CONCLUSIONS

We conclude that the dynamic nature of filament-core systems embedded in globally unstable clouds discussed in the present paper is an attractive model for the observed structure and dynamics of molecular cloud filament-hub systems. Of course, several issues remain to be resolved, most importantly the post-singularity evolution, to determine with greater certainty whether or not a stationary regime develops. We will address this in a further contribution.

Raúl Naranjo Romero acknowledges financial support through PAPIIT project IA103517 from DGAPA-UNAM

REFERENCES

André, P., Di Francesco, J., Ward-Thompson, D., Inutsuka, S.-I., Pudritz, R. E., and Pineda, J. E. (2014). From Filamentary Networks to Dense Cores in Molecular Clouds: Toward a New Paradigm for Star Formation. *Protostars and Planets VI*, pages 27–51.

Arzoumanian, D., André, P., Didelon, P., Könyves, V., Schneider, N., Men'shchikov, A., Sousbie, T., Zavagno, A., Bontemps, S., di Francesco, J., Griffin, M., Hennemann, M., Hill, T., Kirk, J., Martin, P., Minier, V., Molinari, S., Motte, F., Peretto, N., Pezzuto, S., Spinoglio, L., Ward-Thompson, D., White, G., and Wilson, C. D. (2011). Characterizing interstellar filaments with Herschel in IC 5146. *A&A*, 529:L6.

Arzoumanian, D., André, P., Peretto, N., and Könyves, V. (2013). Formation and evolution of interstellar filaments. Hints from velocity dispersion measurements. *A&A*, 553:A119.

Clarke, S. D., Whitworth, A. P., and Hubber, D. A. (2016). Perturbation growth in accreting filaments. *MNRAS*, 458:319–324.

Fischera, J. and Martin, P. G. (2012). Physical properties of interstellar filaments. *A&A*, 542:A77.

Frau, P., Girart, J. M., Alves, F. O., Franco, G. A. P., Onishi, T., and Román-Zúñiga, C. G. (2015). Formation of dense structures induced by filament collisions. Correlation of density, kinematics, and magnetic field in the Pipe nebula. *A&A*, 574:L6.

Gómez, G. C. and Vázquez-Semadeni, E. (2014). Filaments in Simulations of Molecular Cloud Formation. *ApJ*, 791:124.

Gómez, G. C., Vázquez-Semadeni, E., Shadmehri, M., and Ballesteros-Paredes, J. (2007). Formation and Collapse of Quiescent Cloud Cores Induced by Dynamic Compressions. *ApJ*, 669:1042–1049.

Gong, H. and Ostriker, E. C. (2009). Protostar Formation in Supersonic Flows: Growth and Collapse of Spherical Cores. *ApJ*, 699:230–244.

Heitsch, F. (2013a). Gravitational Infall onto Molecular Filaments. *ApJ*, 769:115.

Heitsch, F. (2013b). Gravitational Infall onto Molecular Filaments. II. Externally Pressurized Cylinders. *ApJ*, 776:62.

Heitsch, F., Ballesteros-Paredes, J., and Hartmann, L. (2009). Gravitational Collapse and Filament Formation: Comparison with the Pipe Nebula. *ApJ*, 704:1735–1742.

Heitsch, F., Hartmann, L. W., Slyz, A. D., Devriendt, J. E. G., and Burkert, A. (2008). Cooling, Gravity, and Geometry: Flow-driven Massive Core Formation. *ApJ*, 674:316–328.

Hennebelle, P. and André, P. (2013). Ion-neutral friction and accretion-driven turbulence in self-gravitating filaments. *A&A*, 560:A68.

Ikeda, N., Sunada, K., and Kitamura, Y. (2007). A Survey of Dense Cores in the Orion A Cloud. *ApJ*, 665:1194–1219.

Inutsuka, S.-I. and Miyama, S. M. (1992). Self-similar solutions and the stability of collapsing isothermal filaments. *ApJ*, 388:392–399.

Kirk, J. M., Ward-Thompson, D., Palmeirim, P., André, P., Griffin, M. J., Hargrave, P. J., Könyves, V., Bernard, J.-P., Nutter, D. J., Sibthorpe, B., Di Francesco, J., Abergel, A., Arzoumanian, D., Benedettini, M., Bontemps, S., Elia, D., Hennemann, M., Hill, T., Men'shchikov, A., Motte, F., Nguyen-Luong, Q., Peretto, N., Pezzuto, S., Rygl, K. L. J., Sadavoy, S. I., Schisano, E., Schneider, N., Testi, L., and White, G. (2013). First results from the Herschel Gould Belt Survey in Taurus. *MNRAS*, 432:1424–1433.

Lada, C. J., Muench, A. A., Rathborne, J., Alves, J. F., and Lombardi, M. (2008). The Nature of the Dense Core Population in the Pipe Nebula: Thermal Cores Under Pressure. *ApJ*, 672:410–422.

Larson, R. B. (1969). Numerical calculations of the dynamics of collapsing proto-star. *MNRAS*, 145:271.

Léorat, J., Passot, T., and Pouquet, A. (1990). Influence of supersonic turbulence on self-gravitating flows. *MNRAS*, 243:293–311.

Lin, C. C., Mestel, L., and Shu, F. H. (1965). The Gravitational Collapse of a Uniform Spheroid. *ApJ*, 142:1431.

Murray, D. W., Chang, P., Murray, N. W., and Pittman, J. (2017). Collapse in self-gravitating turbulent fluids. *MNRAS*, 465:1316–1335.

Naranjo-Romero, R., Vázquez-Semadeni, E., and Loughnane, R. M. (2015). Hierarchical Gravitational Fragmentation. I. Collapsing Cores within Collapsing Clouds. *ApJ*, 814:48.

Ostriker, J. (1964). The Equilibrium of Polytropic and Isothermal Cylinders. *ApJ*, 140:1056.

Palmeirim, P., André, P., Kirk, J., Ward-Thompson, D., Arzoumanian, D., Könyves, V., Didelon, P., Schneider, N., Benedettini, M., Bontemps, S., Di Francesco, J., Elia, D., Griffin, M., Hennemann, M., Hill, T., Martin, P. G., Men'shchikov, A., Molinari, S., Motte, F., Nguyen Luong, Q., Nutter, D., Peretto, N., Pezzuto, S., Roy, A., Rygl, K. L. J., Spinoglio, L., and White, G. L. (2013). Herschel view of the Taurus B211/3 filament and striations: evidence of filamentary growth? *A&A*, 550:A38.

Panopoulou, G. V., Psaradaki, I., Skalidis, R., Tassis, K., and Andrews, J. J. (2017). A closer look at the 'characteristic' width of molecular cloud filaments. *MNRAS*, 466:2529–2541.

Penston, M. V. (1969). Dynamics of self-gravitating gaseous spheres-III. Analytical results in the free-fall of isothermal cases. *MNRAS*, 144:425.

Peretto, N., Fuller, G. A., Duarte-Cabral, A., Avison, A., Hennebelle, P., Pineda, J. E., André, P., Bontemps, S., Motte, F., Schneider, N., and Molinari, S. (2013). Global collapse of molecular clouds as a formation mechanism for the most massive stars. *A&A*, 555:A112.

Rathborne, J. M., Lada, C. J., Muench, A. A., Alves, J. F., Kainulainen, J., and Lombardi, M. (2009). Dense Cores in The Pipe Nebula: An Improved Core Mass Function. *ApJ*, 699:742–753.

Rivera-Ingraham, A., Ristorcelli, I., Juvela, M., Montillaud, J., Men'shchikov, A., Malinen, J., Pelkonen, V.-M., Marston, A., Martin, P. G., Pagani, L., Paladini, R., Paradis, D., Ysard, N., Ward-Thompson, D., Bernard, J.-P., Marshall, D. J., Montier, L., and Tóth, L. V. (2017). Galactic cold cores. VIII. Filament formation and evolution: Filament properties in context with evolutionary models. *A&A*, 601:A94.

Rivera-Ingraham, A., Ristorcelli, I., Juvela, M., Montillaud, J., Men'shchikov, A., Malinen, J., Pelkonen, V.-M., Marston, A., Martin, P. G., Pagani, L., Paladini, R., Paradis, D., Ysard, N., Ward-Thompson, D., Bernard, J.-P., Marshall, D. J., Montier, L., and Tóth, L. V. (2016). Galactic cold cores. VII. Filament formation and evolution: Methods and observational constraints. *A&A*, 591:A90.

Schneider, N., Csengeri, T., Bontemps, S., Motte, F., Simon, R., Hennebelle, P., Federrath, C., and Klessen, R. (2010). Dynamic star formation in the massive DR21 filament. *A&A*, 520:A49.

Shu, F. H. (1977). Self-similar collapse of isothermal spheres and star formation. *ApJ*, 214:488–497.

Smith, R. J., Glover, S. C. O., Bonnell, I. A., Clark, P. C., and Klessen, R. S. (2011). A quantification of the non-spherical geometry and accretion of collapsing cores. *MNRAS*, 411:1354–1366.

Vázquez-Semadeni, E., Colín, P., Gómez, G. C., Ballesteros-Paredes, J., and Watson, A. W. (2010). Molecular Cloud Evolution. III. Accretion Versus Stellar Feedback. *ApJ*, 715:1302–1317.

Vázquez-Semadeni, E., Gómez, G. C., Jappsen, A.-K., Ballesteros-Paredes, J., and Klessen, R. S. (2009). High- and Low-Mass Star-Forming Regions from Hierarchical Gravitational Fragmentation. High Local Star Formation Rates with Low Global Efficiencies. *ApJ*, 707:1023–1033.

Vázquez-Semadeni, E., Ryu, D., Passot, T., González, R. F., and Gazol, A. (2006). Molecular Cloud Evolution. I. Molecular Cloud and Thin Cold Neutral Medium Sheet Formation. *ApJ*, 643:245–259.

Whitworth, A. and Summers, D. (1985). Self-similar condensation of spherically symmetric self-gravitating isothermal gas clouds. *MNRAS*, 214:1–25.

Chapter 7

Conclusions

In this work, we have numerically tested and characterized the global hierarchical gravitational collapse scenario in which molecular clouds and their substructures are unstable, and we have determined the implications in comparison with the traditional picture in which the molecular clouds are virialized structures.

In particular, we have found that the evolution of apparently isolated dense cores and those within filamentary structures, both immerse into an highly Jeans-unstable density background (both, uniform and stratified) are in agreement with observations of both, "stable" and "unstable", low- and high- mass prestellar cores in the $M_{\rm core}/M_{\rm BE}$ *vs.* $M_{\rm core}$ diagram of Lada et al. (2008).

For the case of isolated prestellar cores (Naranjo-Romero et al., 2015), the collapse proceeds outside-in, naturally explaining the observation of extended infall velocities (Lee et al., 2001). Moreover, preliminary synthetic observations of these simulations have shown a systematic underestimation of the actual infall speeds (Loughnane *et al.* 2017, in prep), explaining the apparent subsonic infall speeds. At early times, the radial density profile of the core resembles Bonnor-Ebert spheres, even though it is collapsing since the beginning. At late times it approaches the density structure of a Singular Isothermal Sphere, but with a finite infall velocity, rather than being in a hydrostatic state. In this case, prestellar cores can be thought as ram-pressure confined structures increasing their masses due to the accretion from the unstable background, the latter allowing the core to evolve dynamically.

On the other hand, the evolution of the filament+core system, presented in Chap. 6 indicates that the filamentary structure acts as a "funneling" channel, where the material radially accreted from the cloud is longitudinally "drained" down to the core. A simple estimate suggested that a stationary regime where the accretion from the filament to the core balances the accretion from the cloud to the filament. The simulation seems to approach this regime, but does not reach it before the core produces a singularity. Moreover, the value of the central flat part of the filament, fitted to by a Plummer profile, approaches the typical observed values of order 0.1 pc at the end of the simulations.

These findings reinforce the GHC scenario as a plausible scenario for star formation from the MC scale and down to the small core scale (*i.e.*, the *cloud-sheet-filament-core* system), due to accretion across the successive hierarchies in the sequence of collapse,

at least in the prestellar stages.

Future work should extend the evolution of these large-to-small collapsing structures to include the protostellar phase, and perform synthetic observations of the filamentary flow, with different projection angles, in order to provide some clues on the infall velocity profiles of the dense cores immerse into filamentary structure in the GHC scenario.

Appendix A

Appendices

In this section, we discusse some of the details in the numerical code used for the simulations, some of its caveats and future work plans.

A.1 The numerical code

In the present work, we have used the pseudo-spectral numerical code of Passot et al. (1995); Vazquez-Semadeni et al. (1995). Spectral methods[1] (Gottlieb and Orszag, 1977) consist in solving the MHD equations in Fourier space, where the solution is assumed to be a superposition of a set of basis functions truncated at some term, and solving the system by finding the temporal evolution of the coefficients of the solution function. The general advantage of these methods is that they allow to convert a set of coupled integro-differential equations into a set of ordinary differential equations. In particular, pseudo-spectral methods made use of the efficient discrete fast Fourier transform to compute the coefficients of the solution at discrete (spatial or temporal) grid points, reaching roughly the same accuracy as pure spectral methods. Although some computationally expensive ($\mathcal{O} \sim N^2$) non-linear terms could appear in the equations that describe the physical problem (for instance, the advection term, which involve the convolution of the density and velocity), the numerical technique consists in computing a representation of the density and velocity components in real space through the inverse Fourier transform, then computing the convolution and return back to Fourier space. This allows to compute the convolution in $\sim N\ log_2\ N$ operations. Note that in comparison with finite difference numerical methods ($\mathcal{O} \sim N$), pseudo-spectral methods involve more computations. For a more detailed description of the simplest original numerical code and its tests see Passot and Pouquet (1987).

In the numerical code, the MHD equations are expressed in terms of dimensionless variables using the region size, $L/2\pi$, the sound speed and the mean density ρ_0 as units. The dimensionless parameters of the code are: the Reynolds number $R = 2\pi LV\rho_0/\mu$ (where μ is the dynamical viscosity), the acoustic coefficient $M = U/c_0$ (where c_0 is the flow speed in code units. [2]. Thus, M is essentially the Mach number of the characteristic speed U) and the gravitational coefficient $J = (L/c_0)(G\rho_0/\pi)^{1/2} = L/L_{\rm J}$. Table A.1 can be used to transform all the relevant code variables into physical quantities through the relations, and also rescale the simulations in order to obtain different setups essentially adjusting their box sizes, masses and densities through the dimensionless variables and parameters.

[1] The term *Spectral methods* can come from the fact that a solution $u(x,t)$ is expanded into a series of orthogonal eigenfunctions of some linear operator $\mathcal{L}$ (with partial or ordinary derivatives) and thus, the numerical solution is related to its spectrum of Fourier modes.

[2] In our simulations, we ignore viscosity effects due to the molecular viscosity is negligible in comparison to other transport coefficients and therefore we suppose an infinite Reynolds number

Table A.1. Relation between physical and code units used for the numerical code. See text.

Dimensionless variable	Code units	Physical units
L_0	2π	J $L_{\rm J}$
U_0	$\frac{1}{rma} = 1$	$c_{\rm s}$
$t_0 = \frac{L_0}{U_0} = 2\pi$	$\frac{J\ L_{\rm J}}{c_{\rm s}}$	$\left(\frac{32}{3}\right)^{1/2}\ J\ t_{\rm ff}$

A.1.1 Limitations

With respect to the choice of the periodic boundaries scheme adopted in the simulations, it is a reasonable election as long as the scale of the physical processes acting on the different setups (spherical geometry with uniform background, and cylindrical geometry with axisymmetric uniform background, cylindrical geometry with sheet-like background) lie between the largest scale in the simulation (*i.e.*, the numerical box, L_{box}) and the maximum resolution of the box, $l_{res} = L_{box}/512$. This last is the main reason why we restrict our study to the prestellar evolution of the dense cores, close to the protostar formation (*i.e.*, the central singularity). Namely, the Wilbraham-Gibbs phenomenon (*e.g.*, Gibbs, 1898; Hewitt and Hewitt, 1979) in the numerical code due to that in Fourier space, the n-th partial sum of the Fourier series of a periodic, continuous differentiable function behaves in a jump discontinuity increasing the maximum of the partial sum above that of the function itself, thus presenting large oscillations near the jump. Even though, in our simulations the timesteps in which this phenomenon is even slightly present are only the very last and thus we discarded it, we have had to restrict our study to the pre-singularity stages of the evolution. Moreover, although one can think in adding more terms to the Fourier series and thus controlling the error of the approximation (the oscillations) by reducing their width and energy, it turns out that this converges to a fixed height. Instead, a sink-particle-like prescription should be added to the code, a task we postpone for a future study.

A.2 Future work

As we have seen, the present work has been limited to the prestellar stage in the evolution of the simulated dense cores. Therefore, it would be interesting to progressively implement different relevant physical ingredients in the simulations using other numerical codes publicly available. This has the advantage that some of them are already implemented or instead would be almost effortless to implement. One of this would be sink particle formation into an adaptive mesh refinement (or smoothed particle hy-

drodynamics) code, in order to follow the evolution beyond the protostar formation. Another simplification is that our models has only 2 to 4 levels in the hierarchy of the initial density structures (from the cloud to dense core) in the GHC scenario, with a smooth transition between successive substructures. One interesting feature that can be easily implemented is the inclusion of random density fluctuations with their amplitudes reflecting the values in the observations of this structures. Although this could require a more detailed analysis[1], it can mimic the effect of anisotropies in the flow, and probably the formation of elongated flows features accreting material down filaments (*e.g.*, Cox et al., 2016) without requiring the inclusion magnetic fields Chen et al. (2017, *c.f.*). Another aspect to improve is to run non-isothermal simulations with small temperature variations through cooling functions that could derive in the fragmentation of clumps and filaments. And later, implementing the formation of at least some basic molecules and study its depletion effects (*e.g.*, Caselli et al., 1999).

Moreover, in the case of the cloud-core system setups, one of the over-simplification was to locate the dense core at the position of the center of the large-scale gravitational potential on the initial conditions. Therefore, we could study the tidal effects due to the differences in the gravitational potential at the extremes of the core. This would not only stretch the core during the evolution, but also produce alteration in the velocity and density profiles as well as earlier fragmentation of the core.

For the case of the filamentary setups, it would be relatively easy to avoid the infinite length in the filament as well as to include more cores along the filament, in order to study competitive accretion down-to the cores.

Specially interest must be put onto synthetic observations. Although we have a first step in this direction in the work of Loughnane *et al.*, (in prep.), we plan to present synthetic observations of the filament+core system from different angles with respect to the line of sight to determine the most probable observational aspect.

[1] In this case, it would be necesary to convolve the density field with a the beam-size used in the observations as a first step to more directly compare simulations with observations

Bibliography

Alves, J. F., Lada, C. J., and Lada, E. A. (2001). Internal structure of a cold dark molecular cloud inferred from the extinction of background starlight. Nature, 409:159–161. 34

André, P. (2017). Interstellar filaments and star formation. *Comptes Rendus Geoscience*, 349:187–197. 32, 33

André, P., Di Francesco, J., Ward-Thompson, D., Inutsuka, S.-I., Pudritz, R. E., and Pineda, J. E. (2014). From Filamentary Networks to Dense Cores in Molecular Clouds: Toward a New Paradigm for Star Formation. *Protostars and Planets VI*, pages 27–51. 8, 32, 33, 34, 37

André, P., Men'shchikov, A., Bontemps, S., Könyves, V., Motte, F., Schneider, N., Didelon, P., Minier, V., Saraceno, P., Ward-Thompson, D., di Francesco, J., White, G., Molinari, S., Testi, L., Abergel, A., Griffin, M., Henning, T., Royer, P., Merín, B., Vavrek, R., Attard, M., Arzoumanian, D., Wilson, C. D., Ade, P., Aussel, H., Baluteau, J.-P., Benedettini, M., Bernard, J.-P., Blommaert, J. A. D. L., Cambrésy, L., Cox, P., di Giorgio, A., Hargrave, P., Hennemann, M., Huang, M., Kirk, J., Krause, O., Launhardt, R., Leeks, S., Le Pennec, J., Li, J. Z., Martin, P. G., Maury, A., Olofsson, G., Omont, A., Peretto, N., Pezzuto, S., Prusti, T., Roussel, H., Russeil, D., Sauvage, M., Sibthorpe, B., Sicilia-Aguilar, A., Spinoglio, L., Waelkens, C., Woodcraft, A., and Zavagno, A. (2010). From filamentary clouds to prestellar cores to the stellar IMF: Initial highlights from the Herschel Gould Belt Survey. A&A, 518:L102. 34

Arzoumanian, D., André, P., Didelon, P., Könyves, V., Schneider, N., Men'shchikov, A., Sousbie, T., Zavagno, A., Bontemps, S., di Francesco, J., Griffin, M., Hennemann, M., Hill, T., Kirk, J., Martin, P., Minier, V., Molinari, S., Motte, F., Peretto, N., Pezzuto, S., Spinoglio, L., Ward-Thompson, D., White, G., and Wilson, C. D. (2011). Characterizing interstellar filaments with Herschel in IC 5146. A&A, 529:L6. 29, 33, 34

Audit, E. and Hennebelle, P. (2005). Thermal condensation in a turbulent atomic hydrogen flow. A&A, 433:1–13. 13, 41

Audit, E. and Hennebelle, P. (2010). On the structure of the turbulent interstellar clouds . Influence of the equation of state on the dynamics of 3D compressible flows. A&A, 511:A76. 56

Avila-Reese, V. and Vázquez-Semadeni, E. (2001). Turbulent Dissipation in the Interstellar Medium: The Coexistence of Forced and Decaying Regimes and Implications for Galaxy Formation and Evolution. ApJ, 553:645–660. 39

Ballesteros-Paredes, J., Hartmann, L. W., Vázquez-Semadeni, E., Heitsch, F., and Zamora-Avilés, M. A. (2011). Gravity or turbulence? Velocity dispersion-size relation. MNRAS, 411:65–70. 3, 35, 36, 40, 43

Ballesteros-Paredes, J., Klessen, R. S., Mac Low, M.-M., and Vazquez-Semadeni, E. (2007). Molecular Cloud Turbulence and Star Formation. *Protostars and Planets V*, pages 63–80. 39

Ballesteros-Paredes, J., Klessen, R. S., and Vázquez-Semadeni, E. (2003). Dynamic Cores in Hydrostatic Disguise. ApJ, 592:188–202. 34

Ballesteros-Paredes, J., Vázquez-Semadeni, E., and Scalo, J. (1999). Clouds as Turbulent Density Fluctuations: Implications for Pressure Confinement and Spectral Line Data Interpretation. ApJ, 515:286–303. 40

Balsara, D., Ward-Thompson, D., and Crutcher, R. M. (2001). A turbulent MHD model for molecular clouds and a new method of accretion on to star-forming cores. MNRAS, 327:715–720. 34

Barranco, J. A. and Goodman, A. A. (1998). Coherent Dense Cores. I. NH_3 Observations. ApJ, 504:207–222. 36

Bergin, E. A. and Tafalla, M. (2007). Cold Dark Clouds: The Initial Conditions for Star Formation. ARA&A, 45:339–396. 8

Beuther, H., Sridharan, T. K., and Saito, M. (2005). Caught in the Act: The Onset of Massive Star Formation. ApJ, 634:L185–L188. 56

Binney, J. (1998). *Galactic Astronomy (Princeton Series in Astrophysics)*. Princeton University Press. 31

Blitz, L. (1993). Giant molecular clouds. In Levy, E. H. and Lunine, J. I., editors, *Protostars and Planets III*, pages 125–161. 32

Blitz, L. and Shu, F. H. (1980). The origin and lifetime of giant molecular cloud complexes. ApJ, 238:148–157. 38

Bonnor, W. B. (1956). Boyle's Law and gravitational instability. MNRAS, 116:351. 22, 34

Boulares, A. and Cox, D. P. (1990). Galactic hydrostatic equilibrium with magnetic tension and cosmic-ray diffusion. ApJ, 365:544–558. 31

Bourke, T. L., Myers, P. C., Robinson, G., and Hyland, A. R. (2001). New OH Zeeman Measurements of Magnetic Field Strengths in Molecular Clouds. ApJ, 554:916–932. 39

Burke, J. R. and Hollenbach, D. J. (1983). The gas-grain interaction in the interstellar medium - Thermal accommodation and trapping. ApJ, 265:223–234. 14

Busquet, G., Zhang, Q., Palau, A., Liu, H. B., Sánchez-Monge, Á., Estalella, R., Ho, P. T. P., de Gregorio-Monsalvo, I., Pillai, T., Wyrowski, F., Girart, J. M., Santos, F. P., and Franco, G. A. P. (2013). Unveiling a Network of Parallel Filaments in the Infrared Dark Cloud G14.225-0.506. ApJ, 764:L26. 32

Camacho, V., Vázquez-Semadeni, E., Ballesteros-Paredes, J., Gómez, G. C., Fall, S. M., and Mata-Chávez, M. D. (2016). Energy Budget of Forming Clumps in Numerical Simulations of Collapsing Clouds. ApJ, 833:113. 35

Caselli, P., Benson, P. J., Myers, P. C., and Tafalla, M. (2002). Dense Cores in Dark Clouds. XIV. N_2H^+ (1-0) Maps of Dense Cloud Cores. ApJ, 572:238–263. 36

Caselli, P. and Myers, P. C. (1995). The Line Width–Size Relation in Massive Cloud Cores. ApJ, 446:665. 35

Caselli, P., Walmsley, C. M., Tafalla, M., Dore, L., and Myers, P. C. (1999). Co depletion in the starless cloud core l1544. *The Astrophysical Journal Letters*, 523(2):L165. A.4

Chen, C.-Y., Li, Z.-Y., King, P. K., and Fissel, L. M. (2017). Fantastic Striations and Where to Find Them: The Origin of Magnetically Aligned Striations in Interstellar Clouds. ApJ, 847:140. A.4

Chomiuk, L. and Povich, M. S. (2011). Toward a Unification of Star Formation Rate Determinations in the Milky Way and Other Galaxies. AJ, 142:197. 38

Clark, P. C. and Bonnell, I. A. (2005). The onset of collapse in turbulently supported molecular clouds. MNRAS, 361:2–16. 42

Colín, P., Vázquez-Semadeni, E., and Gómez, G. C. (2013). Molecular cloud evolution - V. Cloud destruction by stellar feedback. MNRAS, 435:1701–1714. 41

Cox, D. P. (2005). The Three-Phase Interstellar Medium Revisited. ARA&A, 43:337–385. 31, 32

Cox, D. P. and Smith, B. W. (1974). Large-Scale Effects of Supernova Remnants on the Galaxy: Generation and Maintenance of a Hot Network of Tunnels. ApJ, 189:L105. 31

Cox, N. L. J., Arzoumanian, D., André, P., Rygl, K. L. J., Prusti, T., Men'shchikov, A., Royer, P., Kóspál, Á., Palmeirim, P., Ribas, A., Könyves, V., Bernard, J.-P., Schneider, N., Bontemps, S., Merin, B., Vavrek, R., Alves de Oliveira, C., Didelon, P., Pilbratt, G. L., and Waelkens, C. (2016). Filamentary structure and magnetic field orientation in Musca. A&A, 590:A110. 33, 34, A.4

Crutcher, R. M., Wandelt, B., Heiles, C., Falgarone, E., and Troland, T. H. (2010). Magnetic Fields in Interstellar Clouds from Zeeman Observations: Inference of Total Field Strengths by Bayesian Analysis. ApJ, 725:466–479. 39

Dale, J. E., Ercolano, B., and Bonnell, I. A. (2012). Ionizing feedback from massive stars in massive clusters - II. Disruption of bound clusters by photoionization. MNRAS, 424:377–392. 41

Dale, J. E., Ercolano, B., and Bonnell, I. A. (2013). Ionizing feedback from massive stars in massive clusters - III. Disruption of partially unbound clouds. MNRAS, 430:234–246. 41

Dame, T. M., Elmegreen, B. G., Cohen, R. S., and Thaddeus, P. (1986). The largest molecular cloud complexes in the first galactic quadrant. ApJ, 305:892–908. 35

de Jong, T., Dalgarno, A., and Boland, W. (1980). Hydrostatic Models of Molecular Clouds. In Andrew, B. H., editor, *Interstellar Molecules*, volume 87 of *IAU Symposium*, page 177. 14

Dickey, J. M., Salpeter, E. E., and Terzian, Y. (1977). Temperature Distribution of Neutral Hydrogen at High Galactic Latitudes. ApJ, 211:L77. 31

Dobbs, C. L., Burkert, A., and Pringle, J. E. (2011). Why are most molecular clouds not gravitationally bound? MNRAS, 413:2935–2942. 35

Dobbs, C. L., Krumholz, M. R., Ballesteros-Paredes, J., Bolatto, A. D., Fukui, Y., Heyer, M., Low, M.-M. M., Ostriker, E. C., and Vázquez-Semadeni, E. (2014). Formation of Molecular Clouds and Global Conditions for Star Formation. *Protostars and Planets VI*, pages 3–26. 3, 36, 37

Ebert, R. (1955). Über die Verdichtung von H I-Gebieten. Mit 5 Textabbildungen. ZAp, 37:217. 22, 34

Falgarone, E., Pety, J., and Phillips, T. G. (2001). Filamentary Structure and Helical Magnetic Fields in the Environment of a Starless Dense Core. ApJ, 555:178–190. 34

Falgarone, E., Puget, J.-L., and Perault, M. (1992). The small-scale density and velocity structure of quiescent molecular clouds. A&A, 257:715–730. 35

Federrath, C. (2016). On the universality of interstellar filaments: theory meets simulations and observations. MNRAS, 457:375–388. 34

Ferrière, K. M. (2001). The interstellar environment of our galaxy. *Reviews of Modern Physics*, 73:1031–1066. 13, 31, 32

Field, G. B., Blackman, E. G., and Keto, E. R. (2008). A model of cloud fragmentation. MNRAS, 385:181–188. 41

Field, G. B., Goldsmith, D. W., and Habing, H. J. (1969). Cosmic-Ray Heating of the Interstellar Gas. ApJ, 155:L149. 31

Fischera, J. and Martin, P. G. (2012). Physical properties of interstellar filaments. A&A, 542:A77. 8, 30

Folini, D. and Walder, R. (2006). Supersonic turbulence in shock-bound interaction zones. I. Symmetric settings. A&A, 459:1–19. 56

Galván-Madrid, R., Keto, E., Zhang, Q., Kurtz, S., Rodríguez, L. F., and Ho, P. T. P. (2009). Formation of an O-Star Cluster by Hierarchical Accretion in G20.08-0.14 N. ApJ, 706:1036–1053. 43

Galván-Madrid, R., Zhang, Q., Keto, E., Ho, P. T. P., Zapata, L. A., Rodríguez, L. F., Pineda, J. E., and Vázquez-Semadeni, E. (2010). From the Convergence of Filaments to Disk-outflow Accretion: Massive Star Formation in W33A. ApJ, 725:17–28. 8

Garay, G. (2005). Massive and dense cores: the maternities of massive stars. In Cesaroni, R., Felli, M., Churchwell, E., and Walmsley, M., editors, *Massive Star Birth: A Crossroads of Astrophysics*, volume 227 of *IAU Symposium*, pages 86–91. 56

Gazol, A., Vázquez-Semadeni, E., Sánchez-Salcedo, F. J., and Scalo, J. (2001). The Temperature Distribution in Turbulent Interstellar Gas. ApJ, 557:L121–L124. 31

Gibbs, J. W. (1898). Fourier's Series. Nature, 59:200. A.3

Gibson, D., Plume, R., Bergin, E., Ragan, S., and Evans, N. (2009). Molecular Line Observations of Infrared Dark Clouds. II. Physical Conditions. ApJ, 705:123–134. 3, 36

Glover, S. C. O. and Clark, P. C. (2012). Is molecular gas necessary for star formation? MNRAS, 421:9–19. 14

Glover, S. C. O. and Clark, P. C. (2014). Molecular cooling in the diffuse interstellar medium. MNRAS, 437:9–20. 13

Goldbaum, N. J., Krumholz, M. R., Matzner, C. D., and McKee, C. F. (2011). The Global Evolution of Giant Molecular Clouds. II. The Role of Accretion. ApJ, 738:101. 41

Goldreich, P. and Kwan, J. (1974). Molecular Clouds. ApJ, 189:441–454. 38

Goldsmith, P. F. (1987). Molecular clouds - an overview. In Hollenbach, D. J. and Thronson, Jr., H. A., editors, *Interstellar Processes*, volume 134 of *Astrophysics and Space Science Library*, pages 51–70. 14

Gómez, G. C. and Vázquez-Semadeni, E. (2014). Filaments in Simulations of Molecular Cloud Formation. ApJ, 791:124. 8, 32, 35, 41, 56, 57

Goodman, A. A., Barranco, J. A., Wilner, D. J., and Heyer, M. H. (1998). Coherence in Dense Cores. II. The Transition to Coherence. ApJ, 504:223–246. 36

Gottlieb, D. and Orszag, S. (1977). *Numerical Analysis of Spectral Methods*. Society for Industrial and Applied Mathematics. A.2

Green, C.-E., Cunningham, M. R., Dawson, J. R., Jones, P. A., Novak, G., and Fissel, L. M. (2017). Removing Visual Bias in Filament Identification: A New Goodness-of-fit Measure. ApJ, 840:L17. 34

Hacar, A. and Tafalla, M. (2011). Dense core formation by fragmentation of velocity-coherent filaments in L1517. A&A, 533:A34. 33

Hacar, A., Tafalla, M., Kauffmann, J., and Kovács, A. (2013). Cores, filaments, and bundles: hierarchical core formation in the L1495/B213 Taurus region. A&A, 554:A55. 33

Heiles, C. and Troland, T. H. (2003). The Millennium Arecibo 21 Centimeter Absorption-Line Survey. II. Properties of the Warm and Cold Neutral Media. ApJ, 586:1067–1093. 31, 41

Heitsch, F. (2013a). Gravitational Infall onto Molecular Filaments. ApJ, 769:115. 8

Heitsch, F. (2013b). Gravitational Infall onto Molecular Filaments. II. Externally Pressurized Cylinders. ApJ, 776:62. 8

Heitsch, F., Burkert, A., Hartmann, L. W., Slyz, A. D., and Devriendt, J. E. G. (2005). Formation of Structure in Molecular Clouds: A Case Study. ApJ, 633:L113–L116. 41, 56

Heitsch, F. and Hartmann, L. (2008). Rapid Molecular Cloud and Star Formation: Mechanisms and Movies. ApJ, 689:290–301. 8, 41, 43

Heitsch, F., Hartmann, L. W., Slyz, A. D., Devriendt, J. E. G., and Burkert, A. (2008). Cooling, Gravity, and Geometry: Flow-driven Massive Core Formation. ApJ, 674:316–328. 8, 43

Hennebelle, P. and André, P. (2013). Ion-neutral friction and accretion-driven turbulence in self-gravitating filaments. A&A, 560:A68. 8

Hennebelle, P. and Chabrier, G. (2008). Analytical Theory for the Initial Mass Function: CO Clumps and Prestellar Cores. ApJ, 684:395–410. 40

Hewitt, E. and Hewitt, R. E. (1979). The gibbs-wilbraham phenomenon: An episode in fourier analysis. *Archive for History of Exact Sciences*, 21(2):129–160. A.3

Heyer, M., Krawczyk, C., Duval, J., and Jackson, J. M. (2009). Re-Examining Larson's Scaling Relationships in Galactic Molecular Clouds. ApJ, 699:1092–1103. 3, 35, 36, 39, 40, 43

Heyer, M. H. and Brunt, C. M. (2004). The Universality of Turbulence in Galactic Molecular Clouds. ApJ, 615:L45–L48. 35

Hollenbach, D. and Salpeter, E. E. (1971). Surface Recombination of Hydrogen Molecules. ApJ, 163:155. 14

Hollenbach, D. J. and Tielens, A. G. G. M. (1999). Photodissociation regions in the interstellar medium of galaxies. *Reviews of Modern Physics*, 71:173–230. 14

Hopkins, P. F. (2012). The stellar initial mass function, core mass function and the last-crossing distribution. MNRAS, 423:2037–2044. 40

Hoyle, F. (1953). On the Fragmentation of Gas Clouds Into Galaxies and Stars. ApJ, 118:513. 18, 41

Hunter, C. (1977). The collapse of unstable isothermal spheres. ApJ, 218:834–845. 27

Ibáñez-Mejía, J. C., Mac Low, M.-M., Klessen, R. S., and Baczynski, C. (2016). Gravitational Contraction versus Supernova Driving and the Origin of the Velocity Dispersion-Size Relation in Molecular Clouds. ApJ, 824:41. 8, 35

Jijina, J., Myers, P. C., and Adams, F. C. (1999). Dense Cores Mapped in Ammonia: A Database. ApJS, 125:161–236. 37

Kawachi, T. and Hanawa, T. (1998). Gravitational Collapse of Filamentary Clouds. PASJ, 50:577–586. 33

Kennicutt, R. C. and Evans, N. J. (2012). Star Formation in the Milky Way and Nearby Galaxies. ARA&A, 50:531–608. 31, 32

Kirk, H., Myers, P. C., Bourke, T. L., Gutermuth, R. A., Hedden, A., and Wilson, G. W. (2013). Filamentary Accretion Flows in the Embedded Serpens South Protocluster. ApJ, 766:115. 8

Klessen, R. S. and Glover, S. C. O. (2016). Physical Processes in the Interstellar Medium. *Star Formation in Galaxy Evolution: Connecting Numerical Models to Reality, Saas-Fee Advanced Course, Volume 43. ISBN 978-3-662-47889-9. Springer-Verlag Berlin Heidelberg, 2016, p. 85*, 43:85. 13

Klessen, R. S. and Hennebelle, P. (2010). Accretion-driven turbulence as universal process: galaxies, molecular clouds, and protostellar disks. A&A, 520:A17. 41

Koyama, H. and Inutsuka, S.-i. (2002). An Origin of Supersonic Motions in Interstellar Clouds. ApJ, 564:L97–L100. 13, 14, 41

Krumholz, M. R., Matzner, C. D., and McKee, C. F. (2006). The Global Evolution of Giant Molecular Clouds. I. Model Formulation and Quasi-Equilibrium Behavior. ApJ, 653:361–382. 41

Lada, C. J., Alves, J. F., and Lombardi, M. (2007). Near-Infrared Extinction and Molecular Cloud Structure. *Protostars and Planets V*, pages 3–15. 22

Lada, C. J., Muench, A. A., Rathborne, J., Alves, J. F., and Lombardi, M. (2008). The Nature of the Dense Core Population in the Pipe Nebula: Thermal Cores Under Pressure. ApJ, 672:410–422. 82

Larson, R. B. (1969). Numerical calculations of the dynamics of collapsing proto-star. MNRAS, 145:271. 27, 43

Larson, R. B. (1981). Turbulence and star formation in molecular clouds. MNRAS, 194:809–826. 32, 35, 38, 39

Lee, C. W., Myers, P. C., and Tafalla, M. (2001). A Survey for Infall Motions toward Starless Cores. II. CS (2-1) and N_2H^+ (1-0) Mapping Observations. ApJS, 136:703–734. 82

Lin, C. C., Mestel, L., and Shu, F. H. (1965). The Gravitational Collapse of a Uniform Spheroid. ApJ, 142:1431. 16

Mac Low, M.-M. and Klessen, R. S. (2004). Control of star formation by supersonic turbulence. *Reviews of Modern Physics*, 76:125–194. 39, 40

Mac Low, M.-M., Klessen, R. S., Burkert, A., and Smith, M. D. (1998). Kinetic Energy Decay Rates of Supersonic and Super-Alfvénic Turbulence in Star-Forming Clouds. *Physical Review Letters*, 80:2754–2757. 39

Maddalena, R. J. and Thaddeus, P. (1985). A large, cold, and unusual molecular cloud in Monoceros. ApJ, 294:231–237. 40

McClure-Griffiths, N. M., Dickey, J. M., Gaensler, B. M., Green, A. J., and Haverkorn, M. (2006). Magnetically Dominated Strands of Cold Hydrogen in the Riegel-Crutcher Cloud. ApJ, 652:1339–1347. 32

McKee, C. F. (1989). Photoionization-regulated star formation and the structure of molecular clouds. ApJ, 345:782–801. 38

McKee, C. F. and Ostriker, E. C. (2007). Theory of Star Formation. ARA&A, 45:565–687. 40

McKee, C. F. and Ostriker, J. P. (1977). A theory of the interstellar medium - Three components regulated by supernova explosions in an inhomogeneous substrate. ApJ, 218:148–169. 31

Mestel, L. (1965). Problems of Star Formation - I. QJRAS, 6:161. 39

Mouschovias, T. C. (1987). Star formation in magnetic interstellar clouds: II. Basic theory. Howto manufacture stars by studying waves on strings. In Morfill, G. E. and Scholer, M., editors, *NATO ASIC Proc. 210: Physical Processes in Interstellar Clouds*, pages 491–552. 39

Mouschovias, T. C. (1991). Magnetic braking, ambipolar diffusion, cloud cores, and star formation - Natural length scales and protostellar masses. ApJ, 373:169–186. 38

Murray, N. and Chang, P. (2015). Star Formation in Self-gravitating Turbulent Fluids. ApJ, 804:44. 41

Myers, P. C. (1978). A compilation of interstellar gas properties. ApJ, 225:380–389. 13

Myers, P. C. (1983). Dense cores in dark clouds. III - Subsonic turbulence. ApJ, 270:105–118. 36

Myers, P. C. (2009). Filamentary Structure of Star-forming Complexes. ApJ, 700:1609–1625. 33

Myers, P. C. and Goodman, A. A. (1988). Evidence for magnetic and virial equilibrium in molecular clouds. ApJ, 326:L27–L30. 35

Nakamura, F. and Umemura, M. (1999). On the Mass of Population III Stars. ApJ, 515:239–248. 33

Nakano, T. and Nakamura, T. (1978). Gravitational Instability of Magnetized Gaseous Disks 6. PASJ, 30:671–680. 20

Naranjo-Romero, R., Vázquez-Semadeni, E., and Loughnane, R. M. (2015). Hierarchical Gravitational Fragmentation. I. Collapsing Cores within Collapsing Clouds. ApJ, 814:48. 25, 29, 43, 55, 82

Nejad-Asghar, M. (2016). Modified Bonnor-Ebert spheres with ambipolar diffusion heating. Ap&SS, 361:384. 22

Ntormousi, E., Hennebelle, P., André, P., and Masson, J. (2016). The effect of ambipolar diffusion on low-density molecular ISM filaments. A&A, 589:A24. 34

Ostlie, D. A. and Carroll, B. W. (2006). *An Introduction to Modern Stellar Astrophysics*. Benjamin Cummings. 16

Ostriker, J. (1964). The Equilibrium of Polytropic and Isothermal Cylinders. ApJ, 140:1056. 8, 33

Padoan, P. and Nordlund, Å. (1999). A Super-Alfvénic Model of Dark Clouds. ApJ, 526:279–294. 39

Padoan, P. and Nordlund, Å. (2002). The Stellar Initial Mass Function from Turbulent Fragmentation. ApJ, 576:870–879. 40

Palau, A., Ballesteros-Paredes, J., Vázquez-Semadeni, E., Sánchez-Monge, Á., Estalella, R., Fall, S. M., Zapata, L. A., Camacho, V., Gómez, L., Naranjo-Romero, R., Busquet, G., and Fontani, F. (2015). Gravity or turbulence? - III. Evidence of pure thermal Jeans fragmentation at ˜0.1 pc scale. MNRAS, 453:3785–3797. 37

Palmeirim, P., André, P., Kirk, J., Ward-Thompson, D., Arzoumanian, D., Könyves, V., Didelon, P., Schneider, N., Benedettini, M., Bontemps, S., Di Francesco, J., Elia, D., Griffin, M., Hennemann, M., Hill, T., Martin, P. G., Men'shchikov, A., Molinari, S., Motte, F., Nguyen Luong, Q., Nutter, D., Peretto, N., Pezzuto, S., Roy, A., Rygl, K. L. J., Spinoglio, L., and White, G. L. (2013). Herschel view of the Taurus B211/3 filament and striations: evidence of filamentary growth? A&A, 550:A38. 33

Panopoulou, G. V., Psaradaki, I., Skalidis, R., Tassis, K., and Andrews, J. J. (2017). A closer look at the 'characteristic' width of molecular cloud filaments. MNRAS, 466:2529–2541. 33, 34

Passot, T. and Pouquet, A. (1987). Numerical simulation of compressible homogeneous flows in the turbulent regime. *Journal of Fluid Mechanics*, 181:441–466. A.2

Passot, T., Vazquez-Semadeni, E., and Pouquet, A. (1995). A Turbulent Model for the Interstellar Medium. II. Magnetic Fields and Rotation. ApJ, 455:536. A.2

Penston, M. V. (1969). Dynamics of self-gravitating gaseous spheres-III. Analytical results in the free-fall of isothermal cases. MNRAS, 144:425. 27, 43

Peretto, N., Fuller, G. A., Duarte-Cabral, A., Avison, A., Hennebelle, P., Pineda, J. E., André, P., Bontemps, S., Motte, F., Schneider, N., and Molinari, S. (2013). Global collapse of molecular clouds as a formation mechanism for the most massive stars. A&A, 555:A112. 8, 43

Pilbratt, G. L., Riedinger, J. R., Passvogel, T., Crone, G., Doyle, D., Gageur, U., Heras, A. M., Jewell, C., Metcalfe, L., Ott, S., and Schmidt, M. (2010). Herschel Space Observatory. An ESA facility for far-infrared and submillimetre astronomy. A&A, 518:L1. 32

Pineda, J. E., Goodman, A. A., Arce, H. G., Caselli, P., Foster, J. B., Myers, P. C., and Rosolowsky, E. W. (2010). Direct Observation of a Sharp Transition to Coherence in Dense Cores. ApJ, 712:L116–L121. 3, 36, 37

Polychroni, D., Schisano, E., Elia, D., Roy, A., Molinari, S., Martin, P., André, P., Turrini, D., Rygl, K. L. J., Francesco, J. D., Benedettini, M., Busquet, G., di Giorgio, A. M., Pestalozzi, M., Pezzuto, S., Arzoumanian, D., Bontemps, S., Hennemann, M., Hill, T., Könyves, V., Men'shchikov, A., Motte, F., Nguyen-Luong, Q., Peretto, N., Schneider, N., and White, G. (2013). Two mass distributions in the l 1641 molecular clouds: The herschel connection of dense cores and filaments in orion a. *The Astrophysical Journal Letters*, 777(2):L33. 8, 34, 43

Rivera-Ingraham, A., Ristorcelli, I., Juvela, M., Montillaud, J., Men'shchikov, A., Malinen, J., Pelkonen, V.-M., Marston, A., Martin, P. G., Pagani, L., Paladini, R., Paradis, D., Ysard, N., Ward-Thompson, D., Bernard, J.-P., Marshall, D. J., Montier, L., and Tóth, L. V. (2016). Galactic cold cores. VII. Filament formation and evolution: Methods and observational constraints. A&A, 591:A90. 30

Robertson, B. and Goldreich, P. (2012). Adiabatic Heating of Contracting Turbulent Fluids. ApJ, 750:L31. 41

Salji, C. J., Richer, J. S., Buckle, J. V., di Francesco, J., Hatchell, J., Hogerheijde, M., Johnstone, D., Kirk, H., Ward-Thompson, D., and JCMT GBS Consortium (2015). The JCMT Gould Belt Survey: properties of star-forming filaments in Orion A North. MNRAS, 449:1782–1796. 34

Schneider, N., Csengeri, T., Bontemps, S., Motte, F., Simon, R., Hennebelle, P., Federrath, C., and Klessen, R. (2010). Dynamic star formation in the massive DR21 filament. A&A, 520:A49. 8, 56

Seifried, D., Sánchez-Monge, Á., Suri, S., and Walch, S. (2017). Modelling the chemistry of star-forming filaments - II. Testing filament characteristics with synthetic observations. MNRAS, 467:4467–4483. 34

Shu, F. H. (1977). Self-similar collapse of isothermal spheres and star formation. ApJ, 214:488–497. 3, 21, 23, 24, 25

Shu, F. H. (1992). *The physics of astrophysics. Volume II: Gas dynamics.* 19

Shu, F. H., Adams, F. C., and Lizano, S. (1987). Star formation in molecular clouds - Observation and theory. ARA&A, 25:23–81. 38, 39, 55

Simpson, R. J., Johnstone, D., Nutter, D., Ward-Thompson, D., and Whitworth, A. P. (2011). The initial conditions of isolated star formation - X. A suggested evolutionary diagram for pre-stellar cores. MNRAS, 417:216–227. 34

Sipilä, O., Harju, J., and Juvela, M. (2015). On the stability of nonisothermal Bonnor-Ebert spheres. II. The effect of gas temperature on the stability. A&A, 582:A48. 22

Smith, A. M. and Stecher, T. P. (1971). Carbon Monoxide in the Interstellar Spectrum of Zeta Ophiuchi. ApJ, 164:L43. 14

Smith, R. J., Glover, S. C. O., Bonnell, I. A., Clark, P. C., and Klessen, R. S. (2011). A quantification of the non-spherical geometry and accretion of collapsing cores. MNRAS, 411:1354–1366. 34

Solomon, P. M., Rivolo, A. R., Barrett, J., and Yahil, A. (1987). Mass, luminosity, and line width relations of Galactic molecular clouds. ApJ, 319:730–741. 35

Sridharan, T. K., Beuther, H., Saito, M., Wyrowski, F., and Schilke, P. (2005). High-Mass Starless Cores. ApJ, 634:L57–L60. 56

Stahler, S. W. and Palla, F. (2005). *The Formation of Stars.* Wiley-VCH. 22

Stone, J. M., Ostriker, E. C., and Gammie, C. F. (1998). Dissipation in Compressible Magnetohydrodynamic Turbulence. ApJ, 508:L99–L102. 39

Tafalla, M. and Hacar, A. (2015). Chains of dense cores in the Taurus L1495/B213 complex. A&A, 574:A104. 34

Vazquez-Semadeni, E. (1997). Energy Budget and the Virial Theorem in Interstellar Clouds. *ArXiv Astrophysics e-prints.* 15, 38

Vazquez-Semadeni, E. (1998). Interstellar Turbulence, Cloud Formation and Pressure Balance. *ArXiv Astrophysics e-prints.* 41

Vázquez-Semadeni, E., Banerjee, R., Gómez, G. C., Hennebelle, P., Duffin, D., and Klessen, R. S. (2011). Molecular cloud evolution - IV. Magnetic fields, ambipolar diffusion and the star formation efficiency. MNRAS, 414:2511–2527. 8, 43

Vázquez-Semadeni, E., Colín, P., Gómez, G. C., Ballesteros-Paredes, J., and Watson, A. W. (2010). Molecular Cloud Evolution. III. Accretion Versus Stellar Feedback. ApJ, 715:1302–1317. 8, 41, 43

Vázquez-Semadeni, E., Gazol, A., Passot, T., and et al. (2003). Thermal Instability and Magnetic Pressure in the Turbulent Interstellar Medium. In Falgarone, E. and Passot, T., editors, *Turbulence and Magnetic Fields in Astrophysics*, volume 614 of *Lecture Notes in Physics, Berlin Springer Verlag*, pages 213–251. 31

Vázquez-Semadeni, E., Gazol, A., and Scalo, J. (2000). Is Thermal Instability Significant in Turbulent Galactic Gas? ApJ, 540:271–285. 31

Vázquez-Semadeni, E., Gómez, G. C., Jappsen, A. K., Ballesteros-Paredes, J., González, R. F., and Klessen, R. S. (2007). Molecular Cloud Evolution. II. From Cloud Formation to the Early Stages of Star Formation in Decaying Conditions. ApJ, 657:870–883. 8, 32, 41, 43

Vázquez-Semadeni, E., Gómez, G. C., Jappsen, A.-K., Ballesteros-Paredes, J., and Klessen, R. S. (2009). High- and Low-Mass Star-Forming Regions from Hierarchical Gravitational Fragmentation. High Local Star Formation Rates with Low Global Efficiencies. ApJ, 707:1023–1033. 8, 41, 43, 56

Vázquez-Semadeni, E., González, R. F., Ballesteros-Paredes, J., Gazol, A., and Kim, J. (2008). The nature of the velocity field in molecular clouds - I. The non-magnetic case. MNRAS, 390:769–780. 41

Vázquez-Semadeni, E., Kim, J., Shadmehri, M., and Ballesteros-Paredes, J. (2005). The Lifetimes and Evolution of Molecular Cloud Cores. ApJ, 618:344–359. 8, 25

Vazquez-Semadeni, E., Ostriker, E. C., Passot, T., Gammie, C. F., and Stone, J. M. (2000). Compressible MHD Turbulence: Implications for Molecular Cloud and Star Formation. *Protostars and Planets IV*, page 3. 39

Vazquez-Semadeni, E., Passot, T., and Pouquet, A. (1995). A turbulent model for the interstellar medium. 1: Threshold star formation and self-gravity. ApJ, 441:702–725. A.2

Vázquez-Semadeni, E., Ryu, D., Passot, T., González, R. F., and Gazol, A. (2006). Molecular Cloud Evolution. I. Molecular Cloud and Thin Cold Neutral Medium Sheet Formation. ApJ, 643:245–259. 32, 41, 56

Whitworth, A. and Summers, D. (1985). Self-similar condensation of spherically symmetric self-gravitating isothermal gas clouds. MNRAS, 214:1–25. 3, 21, 27, 28, 43

Whitworth, A. P., Bhattal, A. S., Francis, N., and Watkins, S. J. (1996). Star formation and the singular isothermal sphere. MNRAS, 283:1061–1070. 8, 25, 55

Whitworth, A. P. and Ward-Thompson, D. (2001). An Empirical Model for Protostellar Collapse. ApJ, 547:317–322. 29, 33

Wilson, R. W., Jefferts, K. B., and Penzias, A. A. (1970). Carbon Monoxide in the Orion Nebula. ApJ, 161:L43. 38

Wolfire, M. G., Hollenbach, D., McKee, C. F., Tielens, A. G. G. M., and Bakes, E. L. O. (1995). The neutral atomic phases of the interstellar medium. ApJ, 443:152–168. 13

Zamora-Avilés, M., Ballesteros-Paredes, J., and Hartmann, L. W. (2017). Are fibres in molecular cloud filaments real objects? MNRAS, 472:647–656. 33

Zamora-Aviles, M. and Vazquez-Semadeni, E. (2013). An evolutionary model for the Star Formation Rate and Efficiency in collapsing Molecular Clouds. In *Protostars and Planets VI Posters*. 41

Zamora-Avilés, M. and Vázquez-Semadeni, E. (2014). An Evolutionary Model for Collapsing Molecular Clouds and their Star Formation Activity. II. Mass Dependence of the Star Formation Rate. ApJ, 793:84. 41, 42

Zamora-Avilés, M., Vázquez-Semadeni, E., and Colín, P. (2012). An Evolutionary Model for Collapsing Molecular Clouds and Their Star Formation Activity. ApJ, 751:77. 41, 42

Zuckerman, B. and Evans, II, N. J. (1974). Models of massive molecular clouds. ApJ, 192:L149–L152. 38

Zuckerman, B. and Palmer, P. (1974). Radio radiation from interstellar molecules. ARA&A, 12:279–313. 38, 41